CHARLES UNIVERSITY IN PRAGUE

The First Faculty of Medicine

Doctoral Thesis

Methods of the Spectroscopic Imaging in clinical practice and experiments

Mgr. Filip Jírů

Thesis Adviser:
Ing. Milan Hájek CSc., DrSc.

Prague 2006

Acknowledgment

I am very thankful to my advisor Dr. Milan Hajek without whose support this thesis would not have been possible.

I would like to thank Dr. Uwe Klose for his helpful advices and guidance during my stay in Tuebingen and Prof. Wolfgang Grodd for giving me the opportunity to join his group.

Also, many thanks to Dr. Börje Bjelke for inviting me to Stockholm - my first research training abroad.

Last, but not least, I would like to thank my parents for their encouragement and support in various aspects.

Contents

4 Experimental part 49

List of Abbreviations used

MRS	magnetic resonance spectroscopy
SI, CSI	Spectroscopic imaging
SVS	Single voxel spectroscopy
TE	echo time
TR	repetition time
FT	Fourier transform
DFT	discrete Fourier transform
FOV	field of view
VOI	volume of interest
OVS	outer-volume suppression
PRESS	point resolved spectroscopy
STEAM	stimulated echo acquisition mode
PSF	point spread function
FID	free induction decay
SNR	signal-to-noise ratio
ADC	analogue-digital converter
CSF	cerebrospinal fluid
GM	grey matter
WM	white matter
CSA	chemical shift artifact
CRB	Cramer-Rao bound
Cr	Creatine
Cho	Choline
NAA	N-acetyl aspartate
Lac	Lactate
RF	radio frequency field
SE	spin echo
STE	stimulated echo
EPI	echo-planar imaging
STD	standard deviation
LB	line broadening

1 Introduction

In the last few decades, an effort to understand the physiology and pathology of the human body has given rise to an impulse to develop new diagnostic methods. Magnetic resonance imaging (MRI) among them, has developed into a major technique for non-invasive medical diagnosis and research. MR spectroscopy (MRS), based on the same physical phenomena as MRI, is the only method which enables non-invasive studying of the metabolite composition of tissues *in vivo*. Most disorders are characterized by changes in concentrations of metabolites in the affected tissue, which can be determined from MR spectra. Despite the low sensitivity of MRS due to typically low concentrations of metabolites observed in the tissues, *in vivo* ^{1}H MRS has gained an important place in medical research as well as in clinical practice.

Two major approaches to localize MR spectra in MR spectroscopy can be recognized: Single voxel spectroscopy (SVS) in which the signal is acquired from one spatial location and spectroscopic imaging (SI) which acquires the signal from multiple regions simultaneously. The ability to provide information about the spatial distribution of metabolites in the tissue is of high importance especially for the localization and delimitation of lesions in tissues.

Although the qualitative analysis of MR spectra can reveal the existence of pathologic processes in the examined tissue, the quantitative assessment of the concentration of metabolites enables the estimation of the degree of pathologic changes and comparison of the results to findings measured in healthy controls. Therefore, an accurate quantification of metabolites from MR spectra is highly desirable. To calculate absolute concentrations of metabolites using SI, several issues have to be addressed. This thesis aims to address various aspects of SI data analysis including spectra quantitation, the assessment of SI data quality or the clinical applications of SI. Although the results of the thesis are applicable to the SI technique in general, the thesis focuses mainly on ^{1}H SI of the human brain.

This thesis is divided into theoretical and experimental sections. The theoretical background of SI is reviewed in the theoretical section. Despite the increasing interest in SI among MR researchers and MR clinicians, there is no dedicated monograph dealing with SI techniques and quantitative SI in detail. Therefore, the theoretical section is intended to provide a comprehensive overview of SI principles and important issues of quantitative SI. The presented text is an extended version of a published textbook chapter (1), namely of the part “Principles of CSI” written by the author of the thesis.

In the experimental section, the original work elaborated within the framework of the thesis is presented. With regard to studies already published in the impacted journals or submitted for publication, a brief description of the important results of the studies are given in the experimental section, whereas a detailed description can be found in the manuscripts attached in the appendix.

2 Aims of the thesis

The objective of this thesis was to develop a methodology for the reliable evaluation of *in vivo* SI data. Several aspects of the evaluation of SI data have been addressed as described below.

- **Development of a tool for the processing and analyzing of SI data**.

The processing of SI data represents a complex issue requiring dedicated evaluation programs. Although various spectra processing programs are provided by the vendors of MR scanners, software enabling complete SI data processing and analysis is not available. Therefore, the main aim of this thesis was to establish a comprehensive tool for the processing and analyzing of SI data.

- **Comparison of results obtained by SI and SVS techniques.**

The accuracy of calculated concentrations is of high importance for each quantitation method. SVS techniques can be taken as the gold standard for quantitation of MR spectra. Therefore, to asses the accuracy of the metabolite concentrations measured by SI, the comparison of results obtained by SI and SVS was performed.

- **Development of a fast method for 3D RF mapping and use of the method for correcting the effects of inhomogeneous RF**.

Several factors influence the signal intensities measured by the SI technique. A big issue for quantitative SI at high magnetic fields is the inhomogeneity of the radiofrequency field (RF). To address this issue, the next aim of the thesis was to propose a sequence for fast 3D RF mapping *in vivo* and to use the sequence for compensation of effects related to inhomogeneous RF.

- **Assessment of the quality of spectroscopic images**

For clinical practice, the interpretation of metabolite images rather than individual SI spectra is desirable. Therefore, the reliability of metabolite images is of high importance. To simplify the quality analysis of spectra measured by SI, an error image, reflecting the accuracy of the computed concentrations, can be displayed. The objective of this part of the thesis was testing the relevance of Cramer-Rao bounds as a potential parameter for the calculation of error images for estimated concentrations and the proposal of a new parameter for the calculation of error images for concentration ratios.

- **Clinical application of the developed program**

The last part of the thesis focuses on the use of the developed processing program in clinical application. The developed methodology was used for the evaluation of SI data measured in patients with MRI-negative extratemporal focal epilepsy. The study questions whether ^{1}H MRS could help in the localization of the epileptogenic zone in these patients.

3 Theoretical part

3.1 Basic concepts of the Spectroscopic Imaging

Spectroscopic imaging (SI), also called chemical shift imaging (CSI), is a method that enables to encode spatial distribution of individual metabolites present in the sample (2,3). Spectra from several voxels at different locations, instead of one as in single voxel spectroscopy (SVS), are measured during a single measurement. In this respect, the method combines features of both conventional MRI and SVS. Because information about chemical shifts of individual metabolites present in the signal of each voxel has to be preserved, the classical frequency encoding known from conventional MR imaging cannot be applied. Instead, phase encoding is used exclusively in SI measurement sequences to obtain information on the spatial distribution of signals.

Similar to MR imaging, depending on how many dimensions spectra are spatially resolved in, 1D, 2D, or 3D SI can be distinguished. A scheme of the simple 1D spin-echo SI sequence is shown in Fig. 3.1. Following the excitation pulse, a phase-encoding gradient G along the **x** axis is switched on for the time τ . During this time, the precession frequency ω of all spins along the axis **x** is modified according to

$$\omega(x) = \gamma x G \qquad [3.1]$$

giving rise to space-dependent phase shifts $\phi(x)$ at the end of the phase encoding

$$\phi(x) = -\gamma x G \tau \qquad [3.2]$$

where x is the position of the spins along the **x** axis, assuming the gradient isocenter at x =0.

After application of the refocusing pulse at time TE, data are sampled as a second part of the spin echo. The whole sequence is repeated N times with repetition time TR, while the gradient strength G is changed in N equidistant steps ΔG from the value $G_{min} = -\Delta GN/2$ to $G_{max} = \Delta G(N/2-1)$ as depicted in Fig. 3.1. Denoting G_l as the gradient strength of the l-th phase-encoding step and introducing variable k_l

$$k_l = \frac{\gamma}{2\pi}\tau G_l = \frac{\gamma}{2\pi}\tau l \Delta G \qquad l = -N/2 \ldots N/2-1 \qquad [3.3]$$

the spatially dependent phase shift $\phi_l(x)$ corresponding to l-th phase encoding step equals $\phi_l(x) = -2\pi k_l x$.

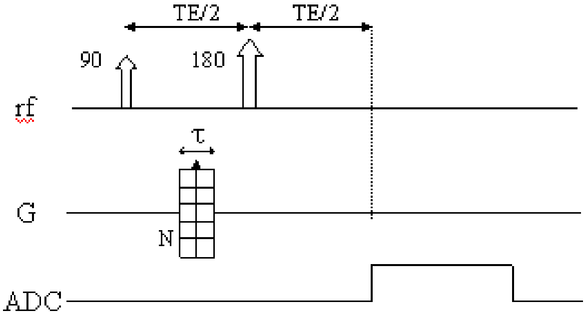

Fig. 3.1 The scheme of the 1D spin echo SI sequence.

Since the overall measured signal $S(t)$ is the sum of all elementary signals $s(t,x)$ distributed along **x** axis, taking additional phase into account, we can for measured signal $S(t,k_l)$ as a function of k_l write

$$S(t,k_l) = \int_{sample} s(t,x) e^{-i2\pi k_l x} dx \qquad [3.4]$$

The measured signal $S(t,k_l)$ is the continuous Fourier transform (FT) of the signals $s(t,x)$ from elementary volumes. The positions of N voxels along the **x** axis can be reconstructed by the inverse discrete Fourier transform (DTF^{-1}). The 1D sequence can be easily extended to 2D (Fig. 3.2a) or 3D (Fig. 3.2b) variants. In 2D and 3D SI, two and three orthogonal phase-encoding gradients are applied, respectively. In reality, as shown in Fig. 3.2, the non selective excitation pulse is often replaced by a frequency selective pulse applied with the slice-selective gradient, resulting in exciting a slice (or slab in case of 3D SI). The phase-encoding gradients are then applied in the plane parallel to the slice in 2D SI, with the third gradient (called partition-encoding gradient) pointing perpendicular to the slice in 3D SI. After the spatial reconstruction, spectra from each element of a matrix, which is called the spectroscopic grid, are available. In 2D SI, the size of the grid corresponds to the field of view (*FOV*) of the SI experiment. In 3D SI, several grids with the same *FOV*, each corresponding to one partition of the excited slice thickness, are available. The number of voxels in the spectroscopic grid (and also the number of partitions) depends on the number of phase-encoding steps performed in the sequence along corresponding directions.

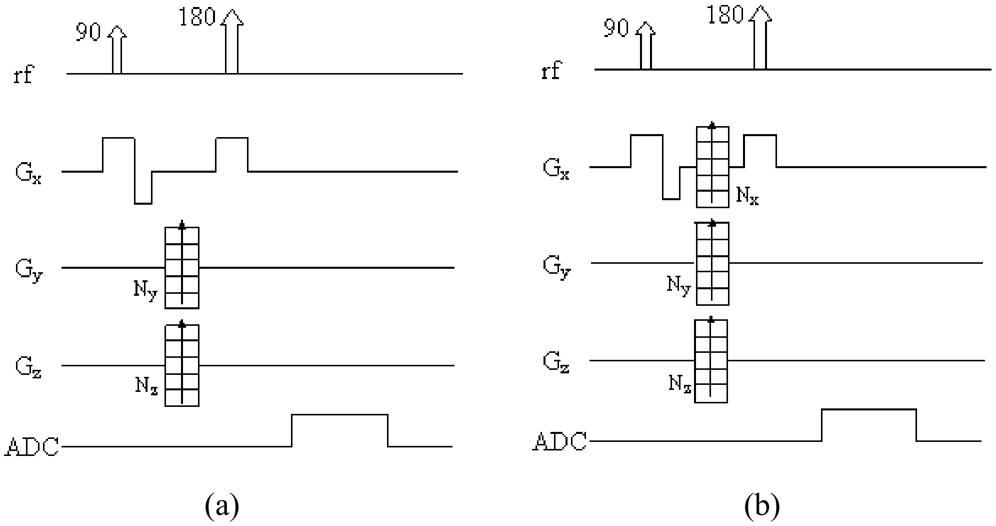

(a) (b)

Fig. 3.2 The scheme of the standard 2D SI (a) and the standard 3D SI (b) spin echo sequence.

To encode positions of the voxels, the sequence with all combinations of phase-encoding increments in all directions has to be repeated. For 3D SI with N_x , N_y , N_z steps (voxels) along corresponding direction, and with N_{acq} representing the number of averages, the acquisition time T_{acq} becomes

$$T_{acq} = N_x N_y N_z N_{acq} TR \qquad [3.5]$$

Due to signal-to-noise and quantification requirements of the measured spectra, repetition time *TR* of the sequence has to be long enough (typically, *TR* =1500 ms). For eight phase-encoding steps along each direction (which is the minimum used number, as discussed later), TR =1500 ms and N_{acq} =1 the acquisition time T_{acq} equals 12.8 min. Because in clinical measurements, more encoding steps are used to achieve better resolution, T_{acq} becomes too long. Therefore, SI sequences are mostly used in 2D mode. Various fast SI sequences, suitable for 3D SI, have been adopted (4), such as sequences using multiple echoes for phase encoding (5,6), sequences using time-varying gradients during the readout period (7-12), sequences derived from the steady state MR imaging sequences (13,14), or the recently implemented parallel spectroscopic imaging techniques (15,16).

3.2 Avoiding undesired excitations in SI

In many cases, examined tissue contains areas with spurious signals, such as areas with poor magnetic field homogeneity, bones, air-containing structures (sinuses), or fatty tissue. These signals are potential sources of the contamination of spectra in other regions. A typical example is ^{1}H SI of the brain, in which strong lipid signals from extracranial subcutaneous fat can contaminate spectra within the brain. Therefore, methods eliminating signals from problematic regions are desirable. Two most often used methods are volume pre-selection and outer volume suppression.

3.2.1 Volume pre-selected SI

The idea of volume pre-selected SI sequences is to incorporate a volume selection used in PRESS or STEAM single voxel spectroscopy into a SI sequence (17,18). In this case, only the desired part of the sample, the *VOI*, is excited using the PRESS or STEAM sequence, while the position of the SI voxels is coded by phase encoding (see Fig. 3.3a, in which a 2D PRESS SI sequence is depicted). Apart from elimination of spurious signals, this approach has another advantage. As is known from MR imaging, to prevent aliasing artifact, all regions of the sample contributing to the measured signal have to be inside the *FOV* (because only phase encoding is performed, frequency low-pass filters cannot be used). This fact dictates the minimum *FOV* size and also the minimum voxel size achievable per fixed time. Because by using volume pre-selected sequences only a restricted area of the sample is excited, *FOV* can be reduced correspondingly, resulting in smaller voxel size without the occurrence of aliasing artifact. However, due to imperfections of pulse profiles, areas outside the selected *VOI* are also partially excited and contribute to the measured signal. Therefore, the *FOV* should always extend beyond the *VOI* to encode positions of these signals (by how much depends on used pulse profiles and the chemical shift artifact), and the *VOI* should be always positioned in the center of the spectroscopic grid. An example of *VOI* positioning with respect to the spectroscopic grid is shown in Fig. 3.3b.

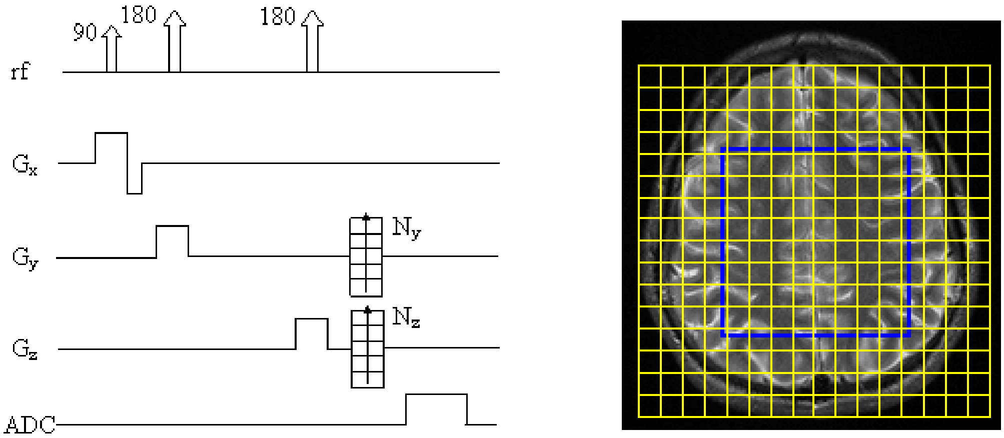

(a) (b)

Fig. 3.3 The scheme of the volume pre-selected 2D PRESS SI sequence (a) and the size and the position of the pre-selected volume (depicted as a black rectangle) with respect to the spectroscopic grid (depicted as a white grid, b).

Spatial encoding of spectra is ensured by the additional phase shifts arising from application of the phase-encoding gradients. The phase-encoding gradients can be at different positions within the sequence. However, any signal present during data sampling and not experiencing this phase shift will not be spatially encoded and added to all points in k-space with the same phase. Because slice profiles are never ideal, every 180° pulse produces, apart from the desired refocusing effect, transverse magnetization also. This magnetization does not encounter encoding gradients whenever they are applied before the 180° pulse. In this case, the signal from this magnetization will not be encoded, and it will contribute to the central voxel. In this respect, performing of encoding after the last pulse in the sequence is advantageous. However, to achieve shorter echo times and avoid eddy currents in the measured spectra, phase encoding is often not realized after the last RF pulse of the sequence. Therefore, proper optimization of the sequence in terms of spoiling unwanted transverse components of 180° pulses in PRESS sequences is necessary. Generally, the elimination of the unwanted coherences can be achieved by the proper application of the spoiler gradients and the cycling of the phases of the pulses, as described both for PRESS and STEAM in the literature. The disadvantage of volume pre-selection by PRESS or STEAM is the rectangular shape of the *VOI*. This restricts the size of the excited area, especially in the brain. Alternatively, by using 2D pulses for excitation, a more general *VOI* shape can be selected (19).

3.2.2 Outer volume suppression

To avoid undesired signals, another method, called outer-volume suppression (OVS) (18,20,21), can also be used. In OVS, areas with spurious signals are saturated by slice selective pulses before the SI sequence starts. Several saturation slices are available to cover regions to be suppressed, as shown in Fig. 3.4a. After each saturation slice is excited, the generated transverse magnetization is spoiled by the crusher gradient as shown in Fig. 3.4b. Because the profiles of the slices are never exactly rectangular (which is especially relevant for large slice thicknesses), saturation slices positioned too close to the area of interest can result in partial suppression of the signals inside the area. In the case when a very large area is to be suppressed, one thick slice can be replaced by two thinner adjoined slices, with the better profile. Because saturation pulses are applied in the pulse train, relaxation of saturated magnetizations during the time between the saturation pulse and the first excitation pulse should be taken into account, especially when many slices are used. This can be solved by varying flip angles of the saturation slices depending on their position in the saturation sequence. Also, because magnetization is always partially recovered at the time of application of the following saturation pulses, multiple excitation in overlapping regions may result in unwanted interactions and the refocusing of spoiled magnetization. This leads to suboptimal signal suppression in the overlapping areas. Therefore, to assure complete spoiling of undesired signals, the OVS concept can be combined with volume pre-selection.

For removal of spurious lipid signals, additional methods can be used such as lipid nulling by means of preparation pulses (22) or using spectral-spatial selective pulses when both only the desired areas and the desired frequency bandwidth are excited at a time (19,23,24). Lipid signals can also be removed by postprocessing methods (25-27). The main disadvantage of lipid nulling is the *T1* weighting of all metabolite signals in the spectra. Concerning spectral-spatial pulses, their length depends on the maximum achievable slew rate, resulting in rather long duration of the pulses, small excitation bandwidth, and also limited minimum echo time of the sequence. Generally, suppression of unwanted lipid resonances becomes less critical when long echo times are used, because $T2$ relaxation time of lipids is much shorter than that of metabolites. However, when quantitative analysis of signals from metabolites having short $T2$ is desired, volume pre-selected SI sequence and outer-volume suppression are the methods of choice.

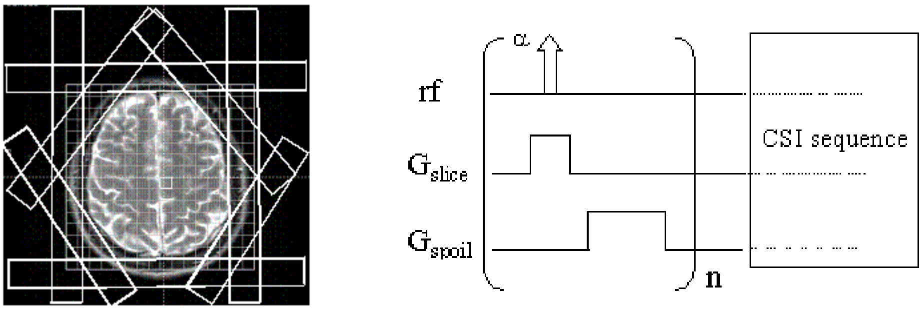

(a) (b)

Fig. 3.4 Outer volume suppression technique. (a) The signal from the subcutaneous fat is saturated using 8 saturation slices depicted as white rectangles. The positions and the thickness of the slices are adjusted before the measurement. (b) The scheme of the OVS sequence. The OVS sequence precedes CSI sequence.

3.3 Reconstruction of SI data

In section 3.1 the effect of 1D phase encoding was demonstrated. In this subsection the generalized reconstruction of 3D SI will be reviewed and the concept of the point spread function introduced. Let us assume a 3D SI sequence with the phase-encoding gradients $\mathbf{G}=(G_x, G_y, G_z)$ applied along the orthogonal coordinate system described by unit vectors $\mathbf{i_x}$, $\mathbf{i_y}$, and $\mathbf{i_z}$. As shown in Fig. 3.2b, gradient strengths along all three directions are incremented in N_x, N_y, and N_z steps of sizes ΔG_x, ΔG_y and ΔG_z. Introducing corresponding increment indexes l, m, and n, then $G_{l,m,n}$, representing the discrete value of the resulting applied gradient, equals

$$\mathbf{G}_{l,m,n} = l\,\Delta G_x\,\mathbf{i_x} + m\,\Delta G_y\,\mathbf{i_y} + n\,\Delta G_z\,\mathbf{i_z} \qquad l = -N_x/2\ldots N_x/2-1 \quad \text{and} \quad m, n \text{ correspondingly} \qquad [3.6]$$

Each gradient combination can be associated with the discrete vector $\mathbf{k}_{\mathrm{l,m,n}}$

$$\mathbf{k}_{\mathrm{l,m,n}} = \gamma \int_{o}^{\tau} \mathbf{G}_{\mathrm{l,m,n}}(t)\,dt = l\Delta k_x \mathbf{i}_{\mathbf{x}} + m\Delta k_y \mathbf{i}_{\mathbf{y}} + n\Delta k_z \mathbf{i}_{\mathbf{z}} \qquad [3.7]$$

The integral in Eq. [3.7] assumes the general case of the time dependent gradient G. In this case, Eq. [3.2] and Eq. [3.3] have to be changed correspondingly.

From Eq. [3.1] to Eq. [3.3], Eq. [3.4] can be generalized for 3D phase encoding

$$S(t, \mathbf{k}_{\mathrm{l,m,n}}) = \int_{coil} s(t, \mathbf{r}) e^{-i2\pi \mathbf{k}_{\mathrm{l,m,n}} \mathbf{r}} \mathrm{d}\mathbf{r} \qquad [3.8]$$

where the integration is performed over the sensitive area of the coil (denoted as *coil*) and **r** represents the position vector relative to the gradient isocenter.

$$\mathbf{r} = x\mathbf{i}_{\mathbf{x}} + y\mathbf{i}_{\mathbf{y}} + z\mathbf{i}_{\mathbf{z}} \qquad [3.9]$$

$S(t,\mathbf{k}_{\mathrm{l,m,n}})$ represents the analogy of k-space in MR imaging, with the difference that not only is one k-space acquired, as in the case of MR imaging, but one k-space for each time point t is sampled. Because gradient amplitudes are incremented discretely, $S(t,\mathbf{k}_{\mathrm{l,m,n}})$ is a discrete function of $\mathbf{k}_{\mathrm{l,m,n}}$. The reconstructed signal $s_{rec}(t, \mathbf{r})$ is usually calculated by the discrete Fourier transform (*DFT*)

$$s_{rec}(t, \mathbf{r}) = \frac{1}{N_x} \frac{1}{N_y} \frac{1}{N_z} \sum_{l,m,n} S(t, \mathbf{k}_{\mathrm{l,m,n}}) e^{i2\pi \mathbf{k}_{\mathrm{l,m,n}} \mathbf{r}} \qquad [3.10]$$

The truncation of the k-space (due to the finite number N_x, N_y, N_z of phase-encoding steps) leads to **r**-space blurring, resulting in finite spatial resolutions Δx, Δy, Δz along $\mathbf{i}_{\mathbf{x}}$, $\mathbf{i}_{\mathbf{y}}$, and $\mathbf{i}_{\mathbf{z}}$ (28)

$$\Delta u = \frac{FOV_u}{N_u} = \frac{1}{\Delta k_u N_u} \qquad u = \{x, y, z\} \qquad [3.11]$$

and the number of voxels equals the number of corresponding phase-encoding steps. The second equality in Eq. [3.11] gives the relation between the size of the *FOV* and the step Δk between k values as a consequence of discrete k-space sampling (Nyquist criterion). The resulting size of the voxel Δx, Δy or Δz is called the Fourier pixel size. Following Eq. [3.10] and Eq. [3.11], signals from voxels at positions $\mathbf{r}_{l',m',n'}$

$$\mathbf{r}_{l',m',n'} = l'\Delta x\, \mathbf{i_x} + m'\Delta y\, \mathbf{i_y} + n'\Delta z\, \mathbf{i_z} \;;\; l' = -N_x/2\ldots N_x/2-1 \quad \text{and} \quad m', n' \text{ correspondingly} \tag{3.12}$$

can be reconstructed by

$$s_{rec}(t,\mathbf{r}_{l',m',n'}) = \frac{1}{N_x}\frac{1}{N_y}\frac{1}{N_z}\sum_{l,m,n} S(t,\mathbf{k}_{l,m,n})e^{i2\pi\mathbf{k}_{l,m,n}\mathbf{r}_{l',m',n'}} \tag{3.13}$$

Equation [3.13] represents the basic formula for the reconstruction of the voxel signals in the SI experiment.

To see the relation between the true signal distribution $s(t,\mathbf{r})$ and the signal $s_{rec}(t,\mathbf{r})$, the inverse *DFT* has to be computed. Substituting $S(t,\mathbf{k}_{l,m,n})$ using Eq. [3.8] and inverting the order of the integral and the summation, the reconstructed signal $s_{rec}(t,\mathbf{r})$ in Eq. [3.13] can be expressed as a convolution of the true signal distribution $s(t,\mathbf{r})$ and the point-spread function (*PSF*)

$$s_{rec}(t,\mathbf{r}) = \int_{coil} s(t,\mathbf{u})PSF(\mathbf{r}-\mathbf{u})\mathrm{d}\mathbf{u} \tag{3.14}$$

where the *PSF* is defined as

$$PSF(\mathbf{r}) = \frac{1}{N_x}\frac{1}{N_y}\frac{1}{N_z}\sum_{l,m,n} e^{i2\pi\mathbf{k}_{l,m,n}\mathbf{r}} \tag{3.15}$$

The *PSF* describes the signal of a hypothetical infinite small point object in the reconstructed image and characterizes the efficiency of the employed reconstruction method. In the case of equally spaced Cartesian sampling, 3D $PSF(\mathbf{r})$ can be separated into three 1D *PSF*, each describing the corresponding dimension

$$PSF(x,y,z) \equiv PSF(\mathbf{r}) = psf_x(x)psf_y(y)psf_z(z) \qquad [3.16]$$

Depending on the number of phase-encoding steps (odd or even number) and the implementation of the gradient incrementing in the measuring sequence, the gradients (and, hence, the $\mathbf{k}_{\mathrm{l,m,n}}$ vector) can be sampled symmetrically or asymmetrically with respect to the zero value. This symmetry influences the final shape of $psf_x(x)$, $psf_y(y)$, and $psf_z(z)$. Direct computation of Eq. [3.15] for $psf_x(x)$, for example, yields the following results (29): In the case of symmetric sampling about zero, when the index l ranges over $l = -(N_x-1)/2, \ldots, 0, \ldots, (N_x-1)/2$ for an odd N_x or over $l = -(N_x-1)/2, \ldots, -1/2, 1/2, \ldots, (N_x-1)/2$ for an even N_x

$$psf_x(x) = \frac{1}{N_x}\sum_{l=-(N_x-1)/2}^{(N_x-1)/2} e^{i2\pi lx/FOV_x} = \frac{1}{N_x}\frac{\sin(\pi N_x x/FOV_{x)}}{\sin(\pi x/FOV_x)} \qquad [3.17]$$

In the case of asymmetric sampling with an even N_x, when the index l ranges over $l = -(N_x/2), \ldots, (N_x/2)-1$,

$$psf_x(x) = \frac{1}{N_x}\sum_{l=-(N_x/2)}^{(N_x/2)-1} e^{i2\pi lx/FOV_x} = \frac{1}{N_x} e^{-i\pi x/FOV_x}\frac{\sin(\pi N_x x/FOV_x)}{\sin(\pi x/FOV_x)} \qquad [3.18]$$

From the preceding expressions, it follows that symmetric sampling leads to a real *PSF*, and asymmetric sampling to a complex *PSF*. Both situations are depicted in Fig. 3.5. In the case of a complex *PSF*, both real and imaginary parts of the FIDs are mixed, and SI spectra show the phase difference with respect to each other. This may cause phasing problems. On the other hand, the *PSF* shape corresponding to asymmetric sampling has a slightly improved profile in terms of the diminished extent and amplitude of the side lobes.

In Fig. 3.6 the influence of the number of phase-encoding steps on *PSF* shape is demonstrated. Clearly, *PSF* shape improves with the increasing number of phase-encoding steps. However, as shown in Eq. [3.5], this improvement is at the expense of acquisition time. The minimum accepted number of encoding steps is usually considered to be 8 (for the *FFT* algorithm, *N* must be a power of 2, unless zero filling is used). Because the *PSF* shape is not rectangular and the *PSF* extends over many voxels, Eq. [3.14] implies that the

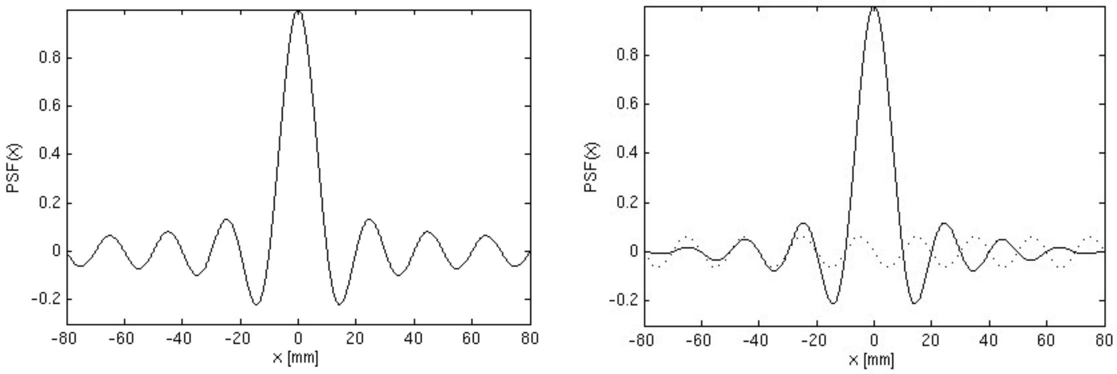

(a) (b)

Fig. 3.5 The shape of 1D point spread function for the symmetrical (a) and asymmetrical (b) k-space sampling. In case of asymmetrical sampling, *PSF* is complex function. The real part is depicted by the solid and the imaginary part by the dotted line.

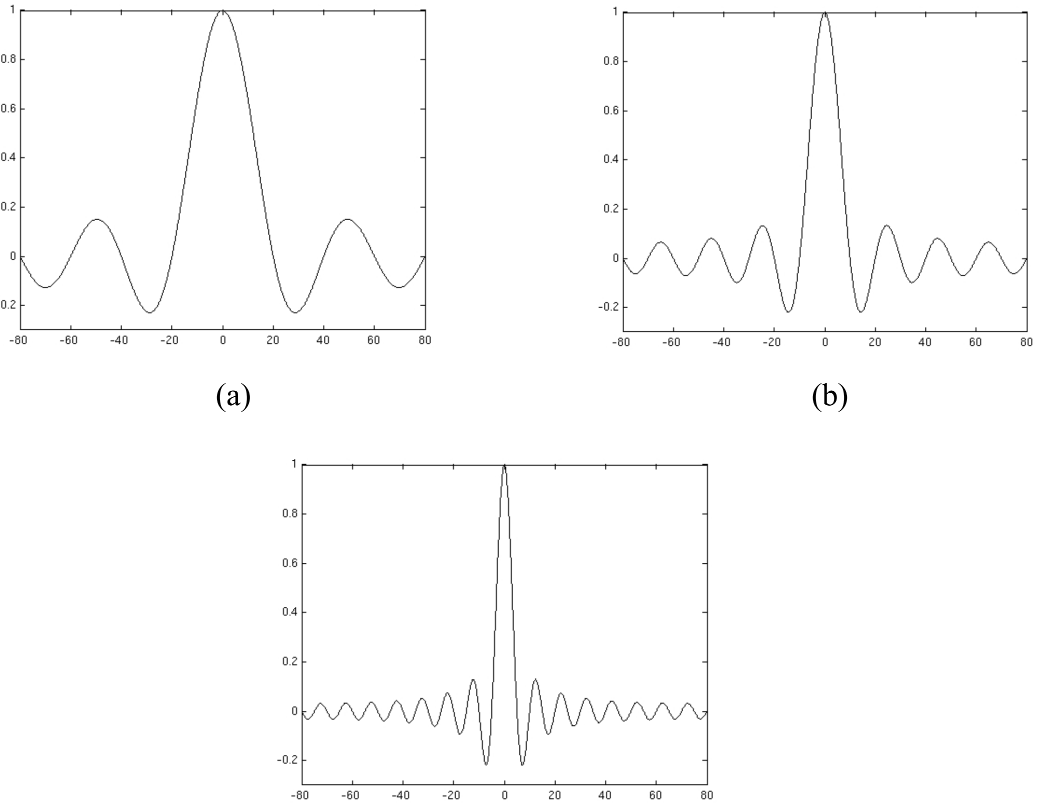

(c)

Fig. 3.6 The dependence of 1D point spread function on the number of symmetrically sampled k-space points. The field of view was assumed to have fixed value 160 mm. The number of k-space points was 8 (a), 16 (b) and 32 (c).

signal measured at the given position (the given voxel, in reality) is always contaminated by the signals from other locations in the sample. This signal “bleeding” leads to the loss of localization precision, and it is the determining factor for the resulting resolution of the SI experiment. The elimination of *PSF* by the deconvolution of the measured concentrations into the known *PSF* and the true metabolite signal is generally not possible, because all spectra in the SI grid are never available with the sufficient quality and deconvolution methods are very prone to noise. Alternatively, *a priori* information from an MRI image can be used for more sophisticated reconstructions to diminish *PSF* effects to some extent (30,31).

The existence of *PSF* explains the need for the suppression of subcutaneous lipids in the scalp and other areas with spurious signals. Even if the relative contributions of distinct voxels are small, the contamination by lipid signal can be severe due to big differences in metabolite and fat concentrations (1:10^3). Moreover, because the frequency of the lipid resonances in distant areas are often shifted (owing to different magnetic field strengths), signal bleeding may result in the spoiling of the whole spectral range.

3.4 K-space weighting techniques

For a fixed size of *FOV*, the profile of the *PSF* improves if the number of phase-encoding steps is increased as depicted in Fig. 3.6. However, due to time constraints and sensitivity reasons, a compromise in the number of encoding steps is necessary. Even if the number of phase-encoding steps is limited, other possibilities of improving the *PSF* shape are available. Because the *FT* of the product of two functions is the convolution of their *FT*, multiplying measured k-space data $S(t,\mathbf{k}_{\mathrm{l,m,n}})$ with a filter function will influence the resulting *PSF*. This post acquisition k-space filtering, also called *apodizatio*n, is realized by the multiplication of the measured k-space data with symmetrical filters having the maximal value in the center of the k-space and smoothly decreasing toward its edges. The operation is performed for all time points *t*. After the application of the filter *w*, Eq. [3.10] can be rewritten as:

$$s_{rec}(t,\mathbf{r}) = \frac{1}{N_x}\frac{1}{N_y}\frac{1}{N_z}\sum_{l,m,n} w(l,m,n)S(t,\mathbf{k}_{\mathrm{l,m,n}})e^{i2\pi\mathbf{k}_{\mathrm{l,m,n}}\mathbf{r}} \qquad [3.19]$$

where $w(l,m,n)$ describes the value of the filter function for the l-th, m-th, and n-th encoding steps. From Eq. [3.14] and Eq. [3.15] the resulting *PSF* is given by

$$PSF(\mathbf{r}) = \frac{1}{N_x}\frac{1}{N_y}\frac{1}{N_z}\sum_{l,m,n} w(l,m,n)e^{i2\pi\mathbf{k}_{l,m,n}\mathbf{r}} \qquad [3.20]$$

Therefore, by using a proper filter function $w(l,m,n)$, the *PSF* profile can be improved. Various filter functions can be used (32), such as the cosine filter

$$w(l) = \cos(\frac{\pi l}{2l_{\max}}) \qquad [3.21]$$

or the Hamming filter

$$w(l) = 0.54 + 0.46\cos(\frac{\pi l}{2l_{\max}}) \qquad [3.22]$$

where l ranges over N_x sampled values, and l_{max} stands for the maximal sampled value of l. 3D extensions are, in the case of Cartesian sampling, given by the product of the corresponding 1D expressions. The effect of filter functions on *PSF* shape is shown in Fig. 3.7. Generally, apodization is always a compromise between *PSF* side lobe reduction and the increase of the width of the main lobe. In this respect, the Hamming function is the optimal filter (32). Because the real resolution of the SI experiment is related to the width of the main lobe of the *PSF* (for details see following subsection), apodization influences the final resolution. Therefore the details of the applied filter should be provided whenever k-space filtering is used.

Postacquisition filtering is not an efficient method of k-space apodization in terms of signal-to-noise ratio (*SNR*) obtained per given time, because the sampled signal from the edges of the k-space is eventually reduced. If more averages are needed, k-space apodization can be performed directly during the measurement by varying the number of averages A_{lmn} for each phase-encoding step (excitation) in proportion to the desired filter function $w(l,m,n)$:

$$w(l,m,n) = A_{lmn} / N_{exc} \qquad N_{exc} = \sum_{l,m,n} A_{lmn} \qquad [3.23]$$

where N_{exc} is the total number of excitations. Analogous to postacquisition filtering, the value of A_{lmn} is maximal in the center of the k-space, where A_{lmn} equals the number of averages N_{acq} of the sequence. It is obvious that apodization during the measurement can only be properly performed when the total number of excitations N_{exc} is sufficient to approximate filter function $w(l, m, n)$ by fractional weights A_{lmn}.

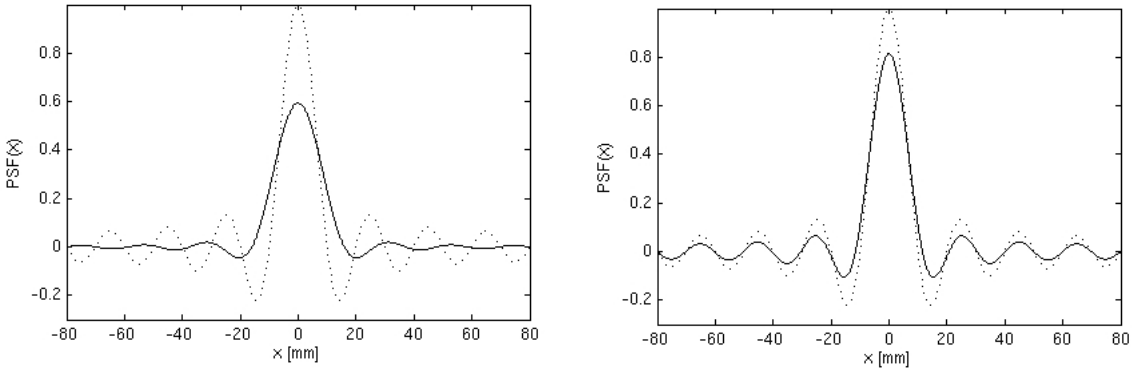

(a) (b)

Fig. 3.7 The influence of a cosine filter (a) and a Hamming filter (b) on the point spread function shape (solid) in comparison to the original *PSF* (dashed) (FOV_x =160 mm, N_x =16, symmetrical sampling).

Because in the case of ^{1}H SI usually only a few averages are needed, an exclusive acquisition weighting is used for non hydrogen nuclei, which require more averages due to sensitivity reasons. When the number of total excitations N_{exc} is small, multiplication of k-space data by a correction smoothing filter, to prevent ringing from sharp digital transitions in weighting, should be performed (33). Apodization can be generally accomplished by any combination of acquisition k-space weighting and the postacquisition filtering. This is the case in reality, because due to the integral number of averages A_{lmn}, the acquisition weighting will not exactly match the required value of $w(l,m,n)$ given by Eq. [3.23]. However, it can be shown (34) that pure acquisition weighting, according to Eq. [3.23], represents an optimal method of producing the desired *PSF* shape in terms of the highest *SNR* in a given measurement time. Alternative methods of acquisition weighting have been proposed, such as weighting achieved by the variable repetition time (35) or, for spiral-based k-space sampling, by variable density of the sampled spiral in k-space (36). The extreme case of weighted sampling is reduced k-space sampling, when some parts of the k-space are not sampled at all. A typical example is circular (spherical) sampling when only points of the k-space inside the circular (spherical) region are sampled and the remaining points are zero-filled (37).This leads to the reduction of the measurement time and also to the improvement of the *PSF* profile. The side lobes of *PSF* are reduced in circular sampling compared to rectangular sampling. This is, however, at the expense of a slight broadening of the central *PSF* lobe. Also, circular sampling leads to an isotropic *PSF* in comparison to rectangular sampling, in which *PSF* side lobes are propagated only along the principal axis. This can be important when potential signal contamination from problematic areas could be reduced by the proper orientation of the SI grid. Variations of circular sampling to achieve further improvements have been suggested (38,39). Reduced sampling can be combined with both acquisition k-space weighting and postacquisition filtering, resulting in various *PSF*s with different data collection efficiencies (33).

3.5 Spatial resolution of SI experiment

Spatial resolution is generally understood as the smallest resolvable distance between two different objects in an image. However, the definition for such a distance is subject to the choice of the object and quality of the image, as well as psychological matters. To compare the performance of various imaging strategies in an imaging experiment, the definition of the achievable resolution dependent solely on the imaging method used is desirable. As shown in Eq. [3.14], the reconstructed signal at a given position in the sample is given by the convolution of the true signal distribution and the *PSF*. In the ideal case of *PSF* equal to the delta function (a rectangular function over one voxel in the discrete case), no contamination would exist and the exact localization of the reconstructed signal would be assured. However, as a consequence of finite k-space sampling, the *PSF* has a non-ideal shape and the spatial resolution of the SI experiment will be determined by the properties of the given *PSF*. In the general case of arbitrarily shaped *PSF*, the resolution Δx can be defined (40) as the width of the approximating boxcar function that has the same height and area as the *PSF*(x), i.e

$$\Delta x = \frac{1}{PSF(0)} \int_{-L/2}^{L/2} PSF(x)dx \qquad [3.24]$$

where integration over the field of view L is performed. Substituting the definition of 1D *PSF* from Eq. [3.15] into Eq. [3.24] and noting that $L=1/\Delta k_x$ gives

$$\Delta x = \sum_l \int_{-L/2}^{L/2} e^{i2\pi k_l x} dx = \frac{1}{N_x \Delta k_x} \qquad [3.25]$$

and analogously for the remaining dimensions y and z.

According to Eq. [3.25], the resolution Δx for the given field of view L is inversely proportional to the number of sampled points N_x in k-space. The calculated resolution Δx is exactly the same as the Fourier pixel size introduced in Eq. [3.11].

The situation is different when a filter function is used to improve the *PSF* shape. Substituting the expression for the filtered *PSF* given by Eq. [3.20] into Eq. [3.24] yields

$$\Delta x = \frac{1}{\sum_l w_l} \int_{-L/2}^{L/2} \sum_l w_l e^{2\pi k_l x} dx = \frac{1}{\sum_l (w_l / w_0) \Delta k_x} \geq \frac{1}{N_x \Delta k_x} \qquad [3.26]$$

where the last inequality is given by the fact that for any practical window function used to improve the *PSF* shape $w_0 \geq w_l$.

Therefore, from Eq. [3.26] it follows that windowing comes at the price of spatial resolution.

3.6 SI preprocessing

Apart from the k-space filtering two additional preprocesing steps are usually performed: Zero filling and grid shifting.

3.6.1 Zero filling

After spatial reconstruction of SI data has been performed, spectra in all voxels of the spectroscopic grid are available. Performing N_x, N_y, and N_z phase-encoding steps along orthogonal directions results, after *DFT* in spatial domain, in $N_x \cdot N_y \cdot N_z$ spatially resolved spectra along corresponding axes.

However, it is possible to increase the number of voxels artificially after the measurement. This operation, called *zero filling*, consists in appending zeros to $S(t,\mathbf{k}_{\mathrm{l,m,n}})$ values prior to the *FT* (Fig. 3.8). Zeros can be appended either symmetrically or asymmetrically, the latter leading to a phase shift in spectra among voxels. Resulting 1D zero filled signal $S_{ZF}(t,k_l)$ can be written

$$S_{ZF}(t,k_l) = S(t,k_l) \quad \text{for} \quad -N_x/2 \le l \le N_x/2-1 \qquad [3.27]$$

$$S_{ZF}(t,k_l) = 0 \quad \text{for} \quad -N_x^{ZF}/2 \le l < -N_x/2 \ \text{ and } \ (N_x/2)-1 < l \le (N_x^{ZF}/2)-1$$

where a symmetrical zero filling from measured N_x points up to N_{ZF} points was assumed.

From Eq. [3.27] and Eq. [3.20] it follows that zero filling does not change the *PSF* of the SI experiment. Recalling the definition of the resolution according to Eq. [3.24] it implies that as the *PSF* remains unchanged the spatial resolution is not improved by zero filling. Zero filling, therefore, represents only an interpolation method and does not affect real spatial resolution. On the other hand it represents a *FT*- tailored interpolation which helps to improve the readability of spectroscopic images.

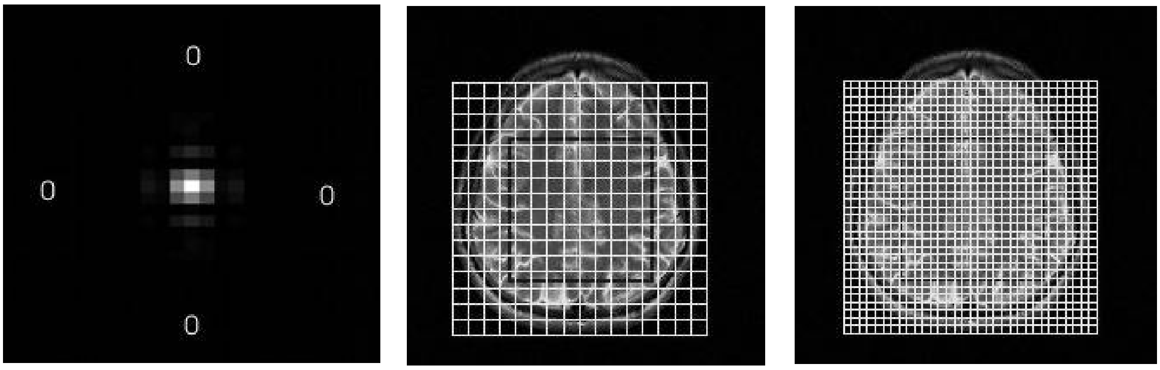

(a) (b) (c)

Fig. 3.8 The effect of zero filling. Zero filling was performed from 16 to 32 data points in both dimensions in k-space (k-space of the first time point shown) (a). Area in the rectangle represents original k-space, while zeros were added symmetrically, resulting in the increase of the number of voxels from original value 16x16 (b) to 32x32 (c).

3.6.2 Grid shifting

Another unique feature of the *FT* reconstruction is the possibility of adjusting the exact position of the grid after the measurement. This operation is based on the shift theorem of *FT*

$$s(t, x_{l'} - x_{j'}) = DFT^{-1}\{S(t, k_l)e^{-i2\pi k_l x_{j'}}\} \quad [3.28]$$

where $x_{j'}$ represents generally the sub-voxel size shift. Eq. [3.28] implies that a multiplication of all k-space values $S\ (t,k_l)$ by a proper phase factor before the DFT^{-1} results in shifting all positions of the voxels (the whole spectroscopic grid). This is very useful because partial volume effects play an important role due to the large voxel size, and by means of grid shifting, the area of interest can be centered in the voxel (Fig. 3.9).

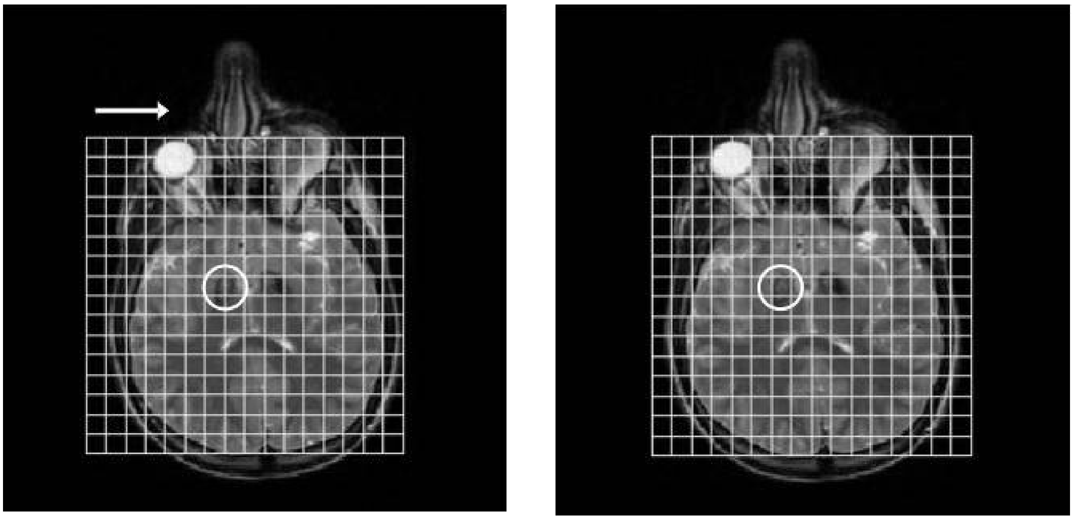

(a) (b)

Fig. 3.9 The shift of the spectroscopic grid. In the original evaluation (a), a selected region has no central voxel. The shift was performed along one direction in order to centre object of interest in one of the voxels and to reduce partial volume effects (b).

3.7 Display of the SI data

Spectroscopic imaging data usually contain substantial amounts of information. To make use of this information efficiently, proper display and analysis of the data are required. There are several ways of presenting spectroscopic imaging data sets. Similar to SVS, one or few selected spectra can be viewed as shown in Fig. 3.10a. This provides spectra in high resolution and enables their reliable inspection. To view all spectra simultaneously, a grid of spectra overlaying the MR scout image can be displayed (Fig. 3.10b). Because the matrix contains many spectra, the size of the displayed spectra is often very small, preventing the operator from resolving all the spectral details. To overcome this, only subsets of all spectra can be displayed.

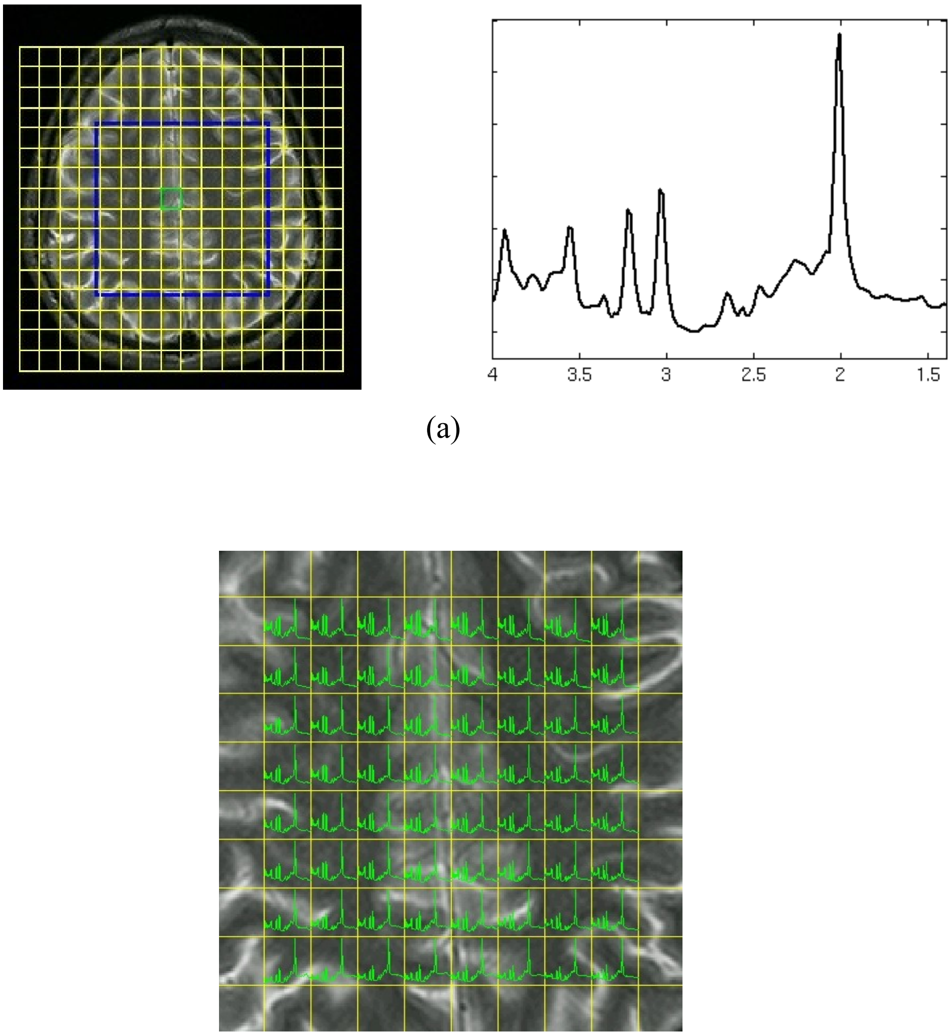

(a)

(b)

Fig. 3.10 The display of acquired spectra. The spectrum from desired voxel can be viewed separately (a) or the grid of spectra overlaying MR scout image can be drawn (b).

The matrix of spectra provides an overview of spectral quality and trends in signal distribution; however, spectra contain complex and often redundant information. Some metabolites may be irrelevant or not well resolved for the study. To summarize the metabolite distribution at a glance, metabolite images (called also metabolite maps) can be computed. For each detectable metabolite in the spectrum, a metabolite image can be calculated when the intensity in the metabolite image corresponds to the signal intensity of the selected metabolite in the given voxel. The resulting image, usually in a color palette, is overlaid on the MR scout image (Fig. 3.11). As pointed out earlier, due to sensitivity reasons, the voxel size is typically of the order of 1 cm^3. The image matrix of spectroscopic images is, therefore, coarse. As previously mentioned, zero filling resulting in a finer matrix can be performed. However, in this case, spectra from more voxels have to be processed. To improve the appearance of the images, interpolation in the image space (after the *FT*) can also be performed. For this purpose bilinear, cubic, or other interpolation methods are used. Even if the apparent resolution of images is improved and the images are better readable, similar to zero filling, the image interpolation does not change the *PSF* and the true resolution of images remains low.

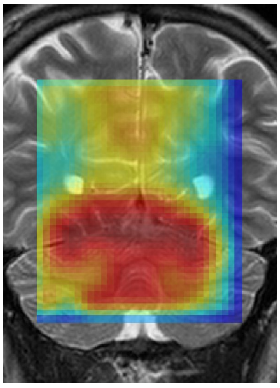

Fig. 3.11 The semi-transparent metabolite image of Creatine measured in the region of the cerebellum. The low signal values correspond to the blue color, whereas the high signal values to the red color.

3.8 Comparison of SVS and SI techniques

SI offers the possibility of acquiring more spectra in the same time instead of just one spectrum as with SVS, but does not bring about any improvement in sensitivity. In terms of *SNR* per unit time and considering that the application of phase encoding is equivalent to spectra averaging, the SI and SVS techniques are equally efficient (41,42). It should be pointed out that the equivalence of both methods, in terms of sensitivity, assumes that SVS and SI voxels have the same size. As shown earlier, due to *PSF* effects, the area contributing to the signal of the selected voxel extends the nominal voxel size. This fact leads to the decreased sensitivity of the SI experiment in terms of the signal measured from one voxel. This can be demonstrated by the integration of *PSF* over the nominal voxel size (43), which in the case of no filtering equals

$$\int_{-\Delta x/2}^{\Delta x/2} PSF(x')dx' = \int_{-\Delta x/2}^{\Delta x/2} \frac{\sin(\pi N_x x'/FOV_{x)}}{N_x \sin(\pi x'/FOV_x)} dx' \approx 0.873 \qquad [3.29]$$

The loss of the voxel signal compared to an ideal selective excitation method is apparent. The signal is not actually lost, but distributed among other voxels (signal bleeding). The overall signal measured in each voxel depends, therefore, on the detailed distribution of the measured signal in the tissue. This fact limits the equivalence of both methods. The preference of one or the other method depends on the number of averages required to acquire spectra of the desired quality. In 2D SI using 16 x 16 matrix, signals from 256 voxels are measured in the same time and with the same *SNR* as opposed to one voxel in SVS using 256 averages. In this case, SI becomes more efficient in terms of acquired information per unit time. On the other hand, if only few averages are needed, e.g., for a reference spectrum without water suppression, SVS is preferable. In practical situations there are also other effects influencing the quality of acquired spectra. The need for shimming of the large volume in the case of SI often means worse magnetic field homogeneity achieved within the whole excited volume, broader signals, and, hence, lower *SNR*. On the other hand, measurements with smaller voxel size are often performed with SI. This leads to better spatial resolution and to improved magnetic field homogeneity within the voxel, resulting in the decrease of the widths when small voxel sizes are used. Significant decrease of line widths was observed when spectra from voxels below 0.4 cm^3 were measured (44).

3.9 Quantitative spectroscopic imaging

The assessment of the absolute concentration of metabolites is of high importance for experimental studies as well as for clinical practice. In contrast to metabolite ratios, which are influenced by changes in concentrations and relaxation times of both the numerator and denominator, absolute concentrations represent a gold standard allowing the accurate comparison and interpretation of results. On the other hand, the estimation of absolute concentrations is more problematic and many factors influencing measured signals have to be taken into account. A great effort has been made in single voxel MR spectroscopy to introduce corrections for various effects influencing the measured signal and to calculate absolute concentration of metabolites *in vivo* (45-47). Most of these corrections are also relevant for quantitative SI. However, additional effects related to the nature of the SI technique have to be taken into account in quantitative SI. In this section, the corrections important for quantitative SI are reviewed.

3.9.1 Calculation of absolute concentrations

The calculation of the absolute concentrations of metabolites relies on the direct proportionality between the concentration of the metabolite, corresponding to the density of magnetization, and the detected signal. A comparison of the signal S_{met}^{cor} of the metabolite with the signal S_{st}^{cor} of the calibration standard of the known concentration C_{st} measured from voxels of the volumes V_{met} and V_{st} yields the desired concentration of the metabolite C_{met}

$$C_{met} = \frac{S_{met}^{cor} N_{st} V_{st}}{S_{st}^{cor} N_{met} V_{met}} C_{st} \qquad [3.30]$$

where N_{st} and N_{met} stand for the number of protons in the molecule contributing to the signals S_{st}^{cor} and S_{met}^{cor}, respectively. The superscript 'cor' indicates that for the calculation of absolute concentrations the corrected signal intensities S^{cor} rather than the measured signal intensities S must be used, as described in the following subsection.

Several strategies for selecting and measuring the calibration standard have been proposed and can been found in comprehensive reviews (45,46).

3.9.2 Introducing corrections

Apart from the voxel volume, the number of contributing protons and the concentration of the metabolite, there are several additional effects influencing measured signal. The general expression for the detected signal of the metabolite acquired from the unit volume can be written as (40)

$$S(\mathbf{r}) = c \cdot g \cdot \lambda(\mathbf{r}) M_0(\mathbf{r}) R(\mathbf{r}) P(\mathbf{r}) \qquad [3.31]$$

where c describes factors that are constant during the measurement of the standard and the metabolite (such as the field strength, nucleus, etc.), g represents the receiver gain, $\lambda(\mathbf{r})$ the reception profile of the coil, $R(\mathbf{r})$ relaxation and saturation effects and $P(\mathbf{r})$ signal changes related to the excitation process. The issue of quantitative MR spectroscopy consists of the fact that the above mentioned effects contribute to the detected signal of the metabolite and the standard to different degrees. Therefore, when calculating absolute concentrations according to Eq. [3.30], signal intensities S_{met}^{cor} and S_{st}^{cor}, corrected for all signal modulating effects have to be used. Denoting $S(l,m)$ measured signal intensities before the correction, and $S^{cor}(l,m)$ corrected signal intensities, the correction factors f_i can be introduced as

$$S^{cor}(l,m) = \frac{S(l,m)}{f_1 f_2 \cdot\cdot f_i} \qquad [3.32\ ]$$

where the indexes l and m stand for the position of the measured voxel in the spectroscopic grid. In the case of 3D SI an additional index describing the position in the partition direction is used. The correction factors f_i for particular effects are described below.

The necessity of the corrections is generally application dependent. Whenever signal variations exceeding the signal change associated with the application of the particular correction are expected, the correction may, in principle, be omitted. An important aspect limiting the number of feasible corrections is often the subject under examination. Some corrections require additional measurements in the subject, which may not be possible due to time constraints. Whenever the particular correction is not performed the error due to the omission of the correction should be estimated and considered when interpreting results. It should be noted that there are additional effects influencing the detected signal and not described later in the text (see (45) for details). However, their influence on the detected signal in ^{1}H SI of the human brain is small and they can be ignored under normal circumstances.

3.9.3 Correction for the receiver gain

During signal detection, the analogue voltage induced in the coil is converted into a digital signal. The digital intensity of the signal in each time point is determined using an analogue-digital converter (*ADC*). To achieve maximum accuracy of the digitalization, the receiver gain of the receiver amplifier is set so that the maximum voltage in the detected signal fills the full volt scale of the *ADC*. Therefore, receiver gain has to be taken into account when comparing measured signals. Depending on the MR system used, receiver gain is given in linear units or in decibels (dB). In the case of linear units, the correction for variable receiver gain can be introduced as

$$f_{RG} = g \qquad [3.33\,]$$

where *g* represents the receiver gain value. If the receiver gain is given in dB, the values have to be converted to the linear scale prior to the calculation of the correction factor according to Eq. [3.33]. It should be noted that modern MR scanners are often equipped with a high resolution *ADC* enabling the receiver gain to be set only in two discrete modes – *LOW* and *HIGH*. In this case, all spectroscopic measurements are usually performed in the *HIGH* mode and the detected signal does not have to be corrected for receiver gain.

3.9.4 Correction for the coil loading

The effective impedance of the coil depends on the sample placed in the coil (coil loading). Therefore, a different voltage U^{glob} to produce a 90° pulse is required for each sample. From the principle of reciprocity for a transmit-receive coil (48), relating the intensity of the detected signal and the transmitting field of the coil, it follows that the detected signal is inversely proportional to the voltage U^{glob}. Therefore, to account for the different coil loading, a correction factor can be introduced (49)

$$f_{cl} = \frac{1}{U^{glob}} \qquad [3.34]$$

where U^{glob} stands for the voltage, which is required for the non-selective 90° pulse. U^{glob} is determined in each subject automatically by the scanner during the calibration of flip angles at the beginning of the measurement. However, since only one effective voltage value U^{glob} for the whole sample volume is used, the correction does not account for a spatially variable radiofrequency field (RF) distribution in the sample. One possible method accounting for the variable RF distribution is the determination of the voltage U^{loc} corresponding to the 90° condition locally in the voxel under examination using several STEAM measurements with variable transmitter amplitudes (50). However, in the case of SI when several voxels are to be measured, the proposed procedure becomes too time consuming. Alternatively, if the map of the flip angle distribution in the measured sample is available, the correction factor f_{cl} according to Eq. [3.34] can be calculated for the voxel with the flip angle value equal to 90° and the influence of RF inhomogeneity can be accounted for additionally using the known flip angle distribution in the sample.

It should be pointed out that the correction, as described in Eq. [3.34], is valid only for transmit-receive coils. In modern MR scanners, to achieve a homogeneous transmitting field and sensitive reception, a body coil is used for excitation and a head coil for reception. In this case, the voltage U^{glob} determined for the body coil provides no information about the receiving coil. However, additional measurements performed both with the body coil as a receiver and a transmitter and with the body coil as a transmitter and the head coil as a receiver allow the relating of signals from both coils and the introduction of an appropriate correction factor (51)

3.9.5 Correction for relaxation times

During the finite time between the signal excitation and the signal reception, transversal relaxation takes place resulting in the decay of the measured signal. Similarly, the repetition of the sequence, required in order to improve the signal-to-noise ratio by signal averaging, may result in the partial saturation of the longitudinal magnetization. As a result of both effects, the amplitude of the measured signal is not directly proportional to the equilibrium magnetization and a correction has to be performed to calculate a theoretical signal strength in the absence of the relaxation effects. The form of the correction depends on the sequence type and sequence timing. The impact of both transversal relaxation and the signal saturation can be reduced by using short *TE* and long *TR*. However, although improvements in hardware have made it possible to achieve short echo times in SI measurements, the use of longer echo times is desirable for some studies. The benefit of using longer echo times consists in the absence of lipid and macromolecule resonances in the spectrum, making the estimation of the baseline easier. Also, when lipid resonances around 1.33 ppm are present in the spectrum, the accurate fitting of lactate resonance is impossible. Similarly, the need to shorten acquisition time often requires the use of short repetition times (*TR*) in the measurement sequences. Assuming an ideal rectangular excitation profile (90° excitation and 180° refocusing), the correction f_{T1} for the longitudinal relaxation and the correction f_{T2} for the transversal relaxation for conventional spin echo (PRESS) and stimulated echo (STEAM) sequences equal (45)

For PRESS:

$$f_{T1} = (1 - e^{\frac{-TR}{T1}}) + 2e^{\frac{-(TR-TE1/2)}{T1}} - 2e^{\frac{-(TR-TE1-TE2/2)}{T1}} \approx (1 - e^{\frac{-TR}{T1}}) \qquad [3.35a]$$

$$f_{T2} = e^{-\frac{TE}{T2}}$$

where *TE1* and *TE2* are two echo times of the double echo in PRESS. The approximation for f_{T1} can be used in practical cases when $TE<<TR$.

For STEAM:

$$f_{T1} = (1 - e^{\frac{-(TR\_STEAM)}{T1}})e^{\frac{-TM}{T1}} \approx (1 - e^{\frac{-(TR)}{T1}})e^{\frac{-TM}{T1}} \qquad [3.35b]$$

$$f_{T2} = e^{-\frac{TE}{T2}}$$

where *TM* denotes a mixing time (time delay between the second and the third pulse) in the STEAM sequence and $TR\_STEAM=TR-TM-TE/2$. The approximation for f_{T1} can be used in practical cases when $TE<<TR$ and $TM<<TR$.

It should be mentioned, that the correction terms for both PRESS and STEAM sequences are valid only in cases, where the transverse magnetization is completely dephased prior to the next sequence repetition and does not coherently contribute to the signal at the beginning of the successive repetition. This assumption is usually fulfilled due to rather long repetition times (at least 1500 ms) compared to the *T2* times of metabolites (about 400 ms) as well as due to the spin dephasing induced by crusher gradients placed at the end of the sequence, or used for water suppression at the beginning of the sequence. Generally, if more sophisticated SI sequences based on coherent steady state methods are used (4,14), correction factors in Eq. [3.35a] and Eq. [3.35b] need to be adopted correspondingly.

The resulting correction for both relaxation times in PRESS and STEAM sequences is given by the product $f_T = f_{T1} f_{T2}$. Observing Eq. [3.35a] and Eq. [3.35b] it follows that the corrections are of low importance when *TE* is very short and *TR* very long. Therefore, a short echo time sequence (*TE* ~ 10 ms) with long repetition time (TR ~ 5000 ms) represents the gold standard for *in vivo* quantitative ^{1}H MR spectroscopy of the human brain. The dependence of the correction term f_T as a function of *T1* and *T2* for the PRESS sequence and relaxation times *T2*=350 ms and *T1*=1500 ms is shown in Fig. 3.12, where the importance of the correction for long *TE* and short *TR* is apparent.

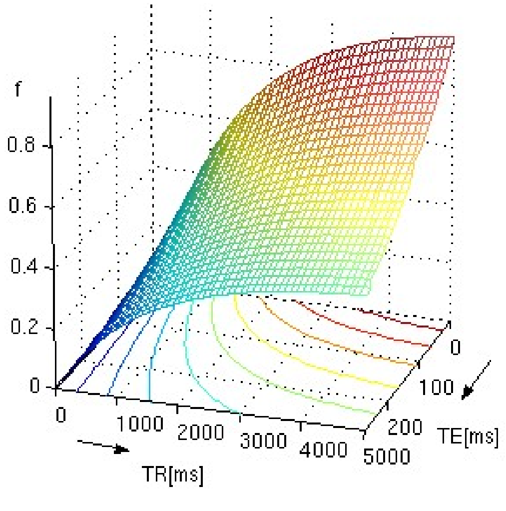

Fig 3.12 Dependence of the correction factor $f = f_{T1} f_{T2}$ on the *TE* and *TR* for the values of *T2*=350 ms and *T1*=1500 ms

Relaxation times *T1* and *T2* are characteristic for each metabolite and are also dependent on the field strength (52,53).

3.9.6 Correction for partial volume effects

The calculation of absolute concentrations according to Eq. [3.30] assumes that the measured metabolite is distributed equally in the whole voxel. When the metabolite is distributed in the examined voxel non-uniformly, the calculated absolute concentrations are biased. This effect is called a partial volume effect.

From the perspective of the distribution of metabolites in the brain, the brain mass can be divided into two distinct parts: brain tissue and the cerebrospinal fluid (*CSF*). In contrast to the brain tissue, the concentration of metabolites in *CSF* is negligible under normal conditions. Since each voxel in the spectroscopic grid contains a generally different percentage of *CSF*, the measured signal of metabolites is modulated by the *CSF* content of the voxel and has to be corrected for. Although knowledge of the *CSF* content is also important in quantitative single voxel spectroscopy, the correction gains greater importance in spectroscopic imaging, where signals from many voxels containing generally different tissue composition are compared. The basic correction procedure consists of the segmentation of the anatomical images into brain tissue and *CSF*, co-registration of the segmented image with the spectroscopic dataset, assessment of the *CSF* percentage in each voxel and the correction of calculated concentrations by the spatially dependent factor

$$f_{CSF}(l,m) = 1 - p^{CSF}(l,m) \qquad [3.36]$$

where $p^{CSF}(l,m)$ represents the average *CSF* percentage in the voxel at the *l*-th, *m*-th coordinate.

The concentrations of metabolites also vary within brain tissue. This reflects the existence of different anatomical-functional structures in the brain. From the anatomical-functional point of view, brain tissue can be divided into grey matter (*GM*) containing mainly neuron bodies and white matter (*WM*) containing axons with myelin sheaths. In Fig. 3.13, the segmented images of *WM*, *GM* and *CSF* in the human brain are shown. The significant differences in the concentrations of metabolites in *WM* and *GM* have been found by several studies (54-56). Although the concentrations vary also within white and gray matter (57,55), the concentration differences between *WM* and *GM* are dominant. The variable concentrations of metabolites in different parts of the brain can, therefore, be understood as a consequence both of the different percentage of *WM* and *GM* in the given voxel and the specific differentiation of brain structures in the given position in the brain.

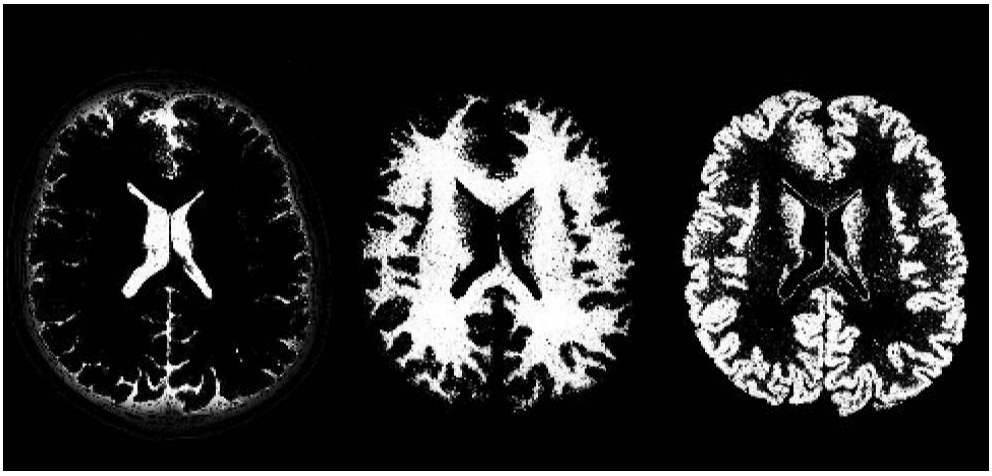

Fig 3.13 The segmented images of CSF, WM and GM (from the left to the right) from the human head.

The concentration of metabolites in pure *WM* and pure *GM* can be calculated using the linear regression between the concentration of the metabolite in several voxels and their *GM* and *WM* percentages (54). However, this method assumes that the concentrations of metabolites in pure *WM* and *GM* are constant in all voxels used for the regression analysis. As an example, the concentrations of the main brain metabolites obtained in the study by McLean (54) are summarized in the Table 3.2. As explained above, due to *PSF* each voxel in the spectroscopic grid is contaminated with the signal from other voxels. This contamination is determined not only by the *PSF* shape and the distribution of the metabolites in the sample, but it is also influenced by the composition of the voxels (in the case of brain tissue by the *CSF*, *WM* and *GM* percentages). For example, there will be no contamination from the neighbouring voxel, if the voxel contains only *CSF*. Therefore, the influence of *PSF* should be taken into account when determining the tissue composition in the given voxel. In other words, the high resolution segmented image should be seen with the 'eyes' of SI measurement. This can be accomplished by resampling the high resolution segmented image to the resolution of the SI data, to mimic a SI experiment with segmented data (58). The correction for variable *CSF* percentage according to Eq. [3.36] is then performed using resampled segmented images.

Metabolite	White matter	Grey matter	$k^{GM/WM}$
NAA+NAAG	7.7 ± 0.6	8.8 ± 0.3	1.2 ± 0.1
Glu+Gln	5.9 ± 0.8	14 ± 2	2.4 ± 0.5
Creatine	3.8 ± 0.4	6.4 ± 0.6	1.7 ± 0.3
Myo-inositol	3.1 ± 0.4	4.9 ± 0.5	1.6 ± 0.3
Choline	1.2 ± 0.2	1.1 ± 0.3	0.9 ± 0.2

Table 3.2 The values of concentrations of selected metabolites in white and grey matter and the value of the corresponding ratio $k^{GM/WM}$ of concentrations in *GM* and *WM*. Adopted from [54].

To segment images into *WM*, *GM* and *CSF* different strategies are used, as described in the literature (59). Generally, to achieve reliable results of segmentation, a good contrast between *WM*, *GM* and *CSF* in the image to be segmented is necessary. As a gold standard, a *T1* weighted 3D magnetization prepared gradient echo sequence (*MPRAGE*) is used, providing very good contrast between individual structures. However, other efficient sequences for the acquisition of images suitable for brain tissue segmentation have been proposed (60,61).

3.9.7 Corrections for excitation and reception profiles

To avoid undesirable spectra contamination arising from subcutaneous lipids, airy structures or bones, SI measurements are often spatially restricted using PRESS or STEAM volume pre-selection (see section 3.2.1). Due to the generally non-rectangular excitation profile of the pre-selected volume (*VOI* profile), the voxels located at different places within the excited slice (or within the slab in the case of 3D SI) experience different flip angles. To accurately compare the concentrations measured in the different position of the slice, the correction of the computed concentrations is necessary. Moreover, when a coil with a non-uniform reception profile is used, the additional signal variations arising from the inhomogeneous reception profile should be accounted for.

The correction factor for the *VOI* profile can be directly measured in the homogeneous phantom by acquisition of the MR image of the *VOI* profile, called further a *VOI image* (62). The *VOI* image must be acquired using the same *VOI* size and *TR* as *in vivo* SI measurement. Since the repetition time *TR* may influence the resulting pulse profile if the condition *TR*>>*T1* does not hold true, an equivalent degree of saturation in phantom and in *in vitro* measurements should be achieved. Therefore, a phantom with the *T1* value comparable to the *T1* values of metabolites *in vivo* should be used. The signal S^{VOI} in the measured *VOI* image is usually normalized to the highest signal intensity in the image and the correction factor for the *VOI* profile is introduced as follows

$$f_p(l,m) = S^{VOI}(l,m) \qquad [3.37]$$

where $S^{VOI}(l,m)$ represents an average value of the signal $S^{VOI}(\mathbf{r})$ in the *l*-th, *m*-th voxel in the *VOI* image.

The correction according to the described procedure accounts for both the *VOI* profile and the reception profile of the coil. However, it should be noted that the *VOI* profile acquired in the phantom may not be the same as the *VOI* profile in the subject. Depending on the way the pulse amplitudes are calculated with respect to the coil loading, different pulse shapes (a number of side lobes) may be used in the phantom and in the subject measurements leading to different excitation profiles. Moreover, the RF distribution in the subject and in the phantom is not equal as a consequence of the interaction between the RF and the sample (63-65).

The second approach is the determination of the correction factor directly in the subject. To eliminate signal variations due to spatially dependent spin density and relaxation times, the *VOI* image is divided by the *reference image* as proposed by McLean (54) (Fig 3.14). The reference image is an image where the influence of the excitation profile is eliminated. In the original 2D implementation this was achieved by enlarging the *VOI* dimensions in both phase encoding directions to the dimensions of the field of view (*FOV*) so that all spins in the reference image experience approximately the same nominal flip angles (90° in STEAM; 90°,180° and 180° in PRESS). Using *VOI* image S^{VOI} and the reference image S^{ref}, the correction factor f_p can be introduced as follows (54)

$$f_p(l,m) = \frac{S^{VOI}(l,m)}{S^{ref}(l,m)} \qquad [3.38]$$

where $S^{ref}(l,m)$ and $S^{VOI}(l,m)$ represent an average value of reference and *VOI* images in the *l*-th, *m*-th voxel.

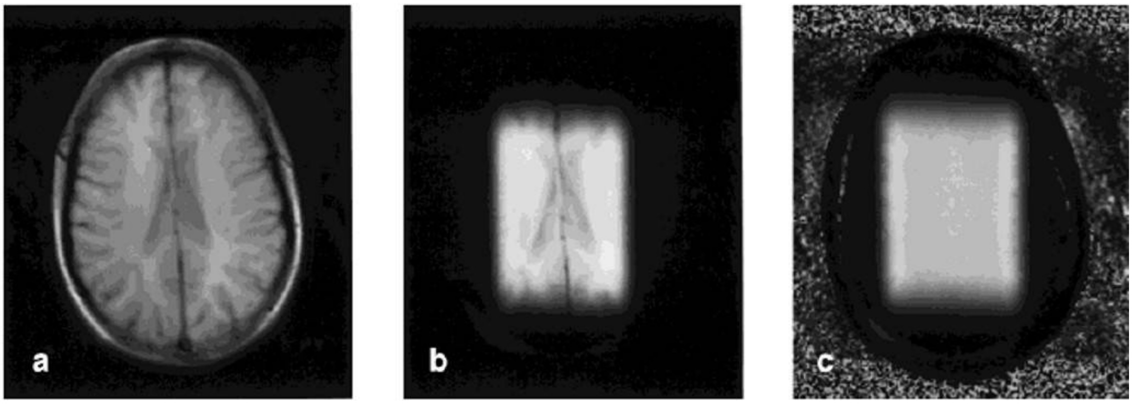

Fig 3.14 Calculation of the excitation profile by the division of the *VOI* and reference images. The *VOI* image (a), The reference image (b) and the calculated excitation profile (c). The images were adopted from (54).

The dependence of f_p in Eq. [3.38] on the reception profile $\lambda(\mathbf{r})$ is eliminated by the division of *VOI* and reference images. Therefore, the correction factor f_p determined using the *VOI* and reference images does not account for the reception profile of the coil. Neglecting the contribution of $\lambda(\mathbf{r})$ is justified only if a homogeneous reception field within the *VOI* can be assumed. On the other hand, in contrast to the phantom profile determination, exactly the same measurement conditions as in the SI examination guarantee the determination of the true excitation profile. However, if an inhomogeneous radiofrequency field exists in the sample, the reference image is no longer a correct reference and the division of the *VOI* and reference images gives an incorrect correction factor. The determination of the excitation profile in an inhomogeneous field is the subject of section 4.5 in the experimental section. The measurements of the *VOI* and reference images can be, in principle, performed using the SI sequence without water suppression. However, the determination of the *VOI* and reference images using an imaging sequence with an implemented volume pre-selection is more efficient. The same radio frequency pulses as in the SI sequence have to be used in the imaging sequence.

3.9.8 Correction for the stability of the MR scanner

The quantitative analysis of MR data relies on the constant performance of the MR hardware. Despite the high reliability of modern MR scanners, quality assurance procedures are of high importance. Due to the possible malfunction of some components of MR scanners, the detected signal may change over time. Therefore, checking and correcting for signal variations connected with temporal instability of the MR scanner is recommended (66). The correction procedure consists of the repeated measurement of the metabolite solution in the phantom using the same protocol. Since the same phantom under the same conditions is measured, the signal variations in the calculated concentration (signal strength) can be attributed to scanner instabilities (Fig. 3.15).

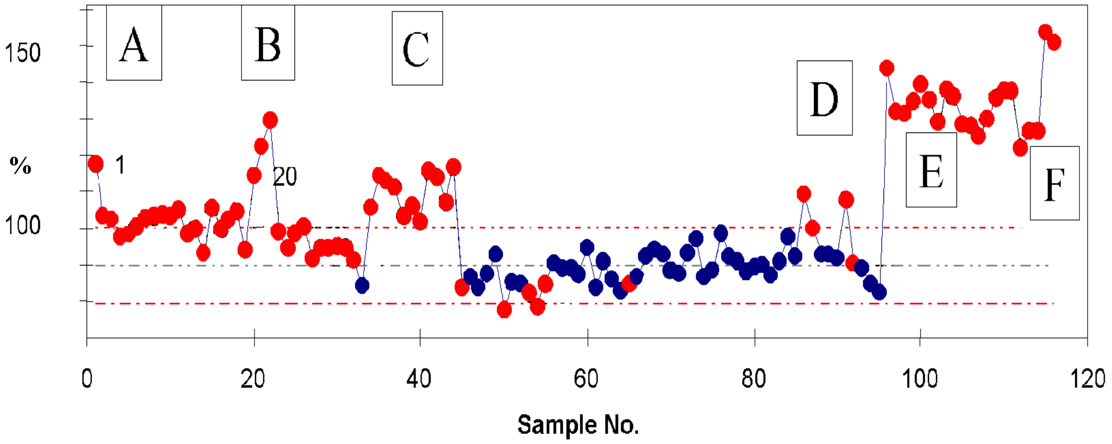

Fig 3.15 The signal variations within 2.5 year. Measurements, indicated by the points, were performed weekly. The signal changes coincided with the various changes in the MR system as follows: A-initial value, B-breakdown of the system, C,D- change of preamplifier, E-new head coil, F-scanner retuning.

The correction factor for temporal instability can then be calculated as

$$f_{stb}(t) = \frac{C(t)}{C_0} \qquad [3.39]$$

where $C(t)$ denotes the concentration measured in the current measurement and C_0 denotes the reference concentration measured at the time of the introduction of the correction.

3.9.9 Chemical shift artifact

The position of the excited slice is based on the assumption that all spins within the slice resonate at one frequency. This is not true when several metabolites with different chemical shifts are present in the excited volume. In this case, the above assumption is violated and spins resonating at different frequencies are excited in different positions. This phenomenon is called chemical shift artifact (*CSA*). The shift d_i (in the direction parallel to the applied gradient G) of the slice excited for the metabolite i (the group resonating at a given frequency) with respect to the slice position for spins resonating at the excitation frequency, is with precision $\sigma_i << 1$, where σ_i is the shielding constant, given as (67)

$$d_i \approx \frac{2\pi\Delta f_i}{\gamma G} \qquad [3.40]$$

where Δf_i is the difference of the metabolite resonance frequency from the transmitting frequency in Hz. In the case of PRESS or STEAM volume pre-selection, the *CSA* affects the position of all three orthogonal slices and *CSA* is presented as a three dimensional shift of the selected *VOI* depending on the strengths of the gradients used for the slice selection along a particular dimension. This situation is depicted in Fig. 3.16. As a consequence, the selected *VOI* may contain a significant amount of tissue outside the desired *VOI* volume – see Fig. 3.16. Denoting d_x, d_y and d_z shifts along directions perpendicular to the individual slices and T_x, T_y, T_z dimensions of the selected *VOI*, then the ratio of the volume selected outside the desired position of the *VOI* to the volume of the *VOI* can be written as

$$\Delta V = 1 - \frac{(T_x - d_x)(T_y - d_y)(T_z - d_z)}{T_x T_y T_z} \qquad [3.41]$$

From Eq. [3.41] it follows, that the *CSA* is pronounced especially for small slice thicknesses, where the reduction of the *CSA* is of importance.

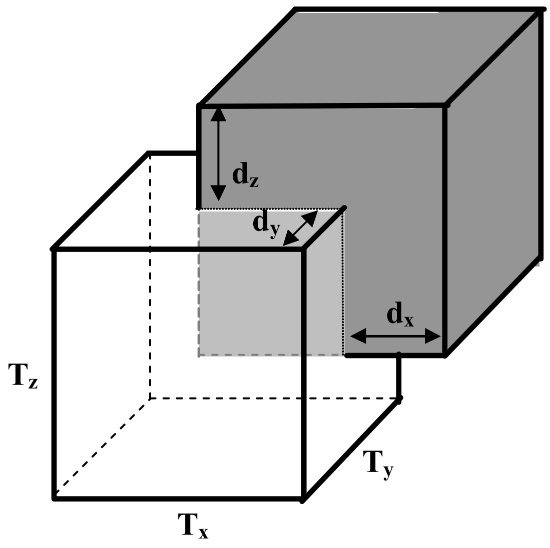

Fig. 3.16 The chemical shift artifact in three dimensions. The desired *VOI* position, as adjusted in the measurement, is depicted in black. As a consequence of CSA the *VOI* is shifted in three dimensions (depicted in gray), where the shifts d_x d_y and d_z vary among particular metabolites according to Eq. [3.40].

The slice shift d_i can be reduced by increasing the strength of the corresponding slice selection gradient G and by minimizing the difference Δf_i between metabolite's resonance frequency and the transmitting frequency. Therefore, the transmitting frequency is usually set on the resonance frequency of the metabolite of the highest interest or, as a compromise, in the middle of the observed spectral range. Due to the increasing frequency range of metabolites with the increasing field strength the *CSA* is an issue especially at high field strengths.

Since *CSA* affects only the position of the pre-selected volume but not the position of the SI grid, it is manifested as a shift of the excited volume with respect to the spectroscopic grid in SI. Therefore, assuming an ideal rectangular excitation profile, in 2D SI *CSA* will shift the position of all voxels in the slice direction but the shift of the *VOI* in both phase encoding directions will influence the signal only in the partially excited voxels at the edge of the *VOI*. However, in reality due to the non-rectangular excitation profile the shift in both phase encoding directions influences the signal of all voxels in the *VOI* depending on the exact shape of the excitation profile. Chemical shift artifact has to, therefore, be taken into account in the correction for the excitation (reception) profile, where the position of the excitation (reception) profile has to be adjusted independently for each metabolite according to the corresponding slice shift d_i.

Because some of the metabolites resonate at several frequencies (CH, CH_2, CH_3 groups), the position of the selected slice differs for each functional group even within one metabolite. Due to the non-ideal excitation profile of the pulse, the individual resonances are excited with a different pulse angle. In the case of the inhomogeneous distribution of the metabolite in the sample, this may lead to the decreased accuracy of the calculated concentration of metabolites when fitting methods decomposing the spectrum into model basis sets (LCModel) are used. The situation is even more complicated for coupled systems, where unequal excitations of individual coupling partners (e.g in the AX_3 system in lactate of A nucleus and X_3 nuclei) results in unwanted signal modulations (68,69) .

Due to the lower sensitivity of 180° pulses to *CSA* compared to 90° pulses, the 180° pulses in the PRESS sequence are usually applied with the gradient along the slice direction, where the slice thickness is the smallest. As a consequence, the remaining 90° and 180° pulses are applied with gradients along individual phase encoding directions leading to the asymmetric shifts along each phase encoding direction.

3.9.10 Determination of the signals of metabolites

The accurate assessment of the signals of the individual metabolites present in the measured signal is a key part of the quantitative analysis. In principle, the measured signal can be processed in the time of frequency domains using parameterized or non-parameterized methods and imposing a different degree of prior knowledge about the evaluated signals (70,71). Each mentioned approach has its advantages and disadvantages and the selection of the processing method has to be considered for the given study (long or short *TE*, ^{1}H or ^{31}P spectroscopy) and requirements (absolute quantification, processing speed). Several programs enabling estimation of signal strengths or the concentrations of metabolites directly have been presented. To quantify ^{1}H SI spectra, the SI data interface CULICH (72), using the LCModel program (73) for spectra fitting, has been developed within the framework of this thesis. Therefore, a brief description of the signal analysis by the LCModel program is given below.

3.9.11 Description of the LCModel program

The LCModel program is a commercial program, dedicated originally to single voxel spectra processing. The program decomposes the measured *in vivo* spectrum into spectra of individual metabolites measured *in vitro*, which form a basis set (Fig. 3.17)

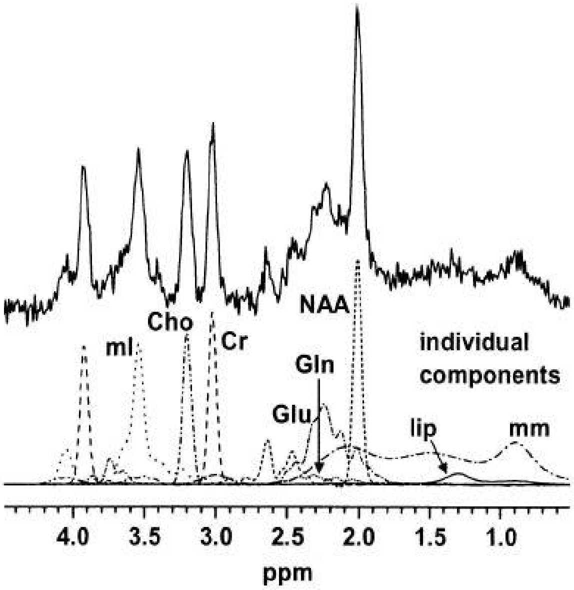

Fig. 3.17 The decomposition of the spectrum (upper picture) into individual metabolites included in the basis set (lower picture). The figure was adopted from (74).

To ensure the correct decomposition of the spectrum, the basis set must contain all metabolites detectable in the *in vivo* spectrum. Since the concentrations of all *in vitro* spectra in the basis set are known, the basis set also serves as a concentration reference, enabling the calculation of concentrations of *in vivo* metabolites in the spectrum. The concentrations are determined as follows: First both the *in vivo* data and the *in vitro* basis set are zero filled to double the number of points in the time domain and Fourier transformed. The discrete in vivo spectrum $Y(\nu_k)$ is then modelled using the basis set metabolites M_l as

$$\hat{Y}(\nu_k) = e^{-i(\phi_0+\nu_k\phi_1)}[\sum_{j=1}^{N_B}\beta_j B_j(\nu_k) + \sum_{l=0}^{N_M} C_l \sum_{n=-N_S}^{N_S} S_n M_l(\nu_{k-n},\gamma_l,\varepsilon_l)] \qquad [3.42]$$

with the constraints

$$C_l \geq 0 \quad \gamma_l \geq 0 \quad \sum_{n=-N_S}^{N_S} S_n = 1 \qquad [3.43]$$

where C_l are concentrations of the N_M metabolites measured in vitro. The N_M metabolite spectra in the basis set, N_l (ν,0,0), are broadened to account for shorter *T2* times in vivo (the parameter γ_l) and shifted to account for small errors in referencing the spectra (parameter ε_l).

The basis set metabolites M_l(ν,γ_l ,ε_l) with the parameters γ_l and ε_l are calculated from

$$M_l(\nu, \gamma_l, \varepsilon_l) = F\{m_l(t)e^{-t(\gamma_l + i\varepsilon_l)}\} \qquad [3.44]$$

where *F* denotes discrete Fourier transform and $m_l(t)$ is the inverse *DFT* of the model spectrum M_l(ν,0,0). The last sum in Eq. [3.42] is a discrete convolution of the basis set metabolites M_l with the lineshape coefficients S_n to account for field inhomogenenities and eddy currents. The baseline is modelled by N_B cubic B-splines, B_j(ν) with equally spaced knots (the term in the first sum in Eq. [3.42]). Φ_0 and Φ_1 (the arguments of the first exponential in Eq. [3.42]) are zero and first order phase corrections.

The model parameters are estimated using a Marquard modification of a constrained Gauss-Newton least squares method

$$\frac{1}{\sigma^2(Y)} \sum_{k=1}^{N} \{\mathrm{Re}[\hat{Y}(\nu_k) - \hat{Y}(\nu_k)]\}^2 + T = \text{minimum} \qquad [3.45]$$

Besides the usual squared difference between the model function and the measured spectrum resolved in *N* data points, the term *T* containing additional contributions imposing the smoothness and zero boundary conditions on lineshape coefficients S_n and the smoothness of spline baseline in the minimized function is considered. The calculated concentration values are provided along with estimates of their Cramer-Rao bounds (*CRBs*). For the details of the minimization procedure see Appendix in ref (73) and (75).

The scaling of basis set metabolites and of the measured *in vivo* spectrum is performed automatically by LCModel according to the volumes of the voxels and corresponding transmitter reference amplitudes. The remaining corrections have to be performed individually by the user. The standard output of LCModel analysis is shown in Fig. 3.18. Original phased spectrum, fitted spectrum, residuum, baseline and estimated concentrations with their Cramer-Rao bounds can be seen in the standard output. In addition, all estimated parameters as well as details of the spectra fitting are available in the special text files.

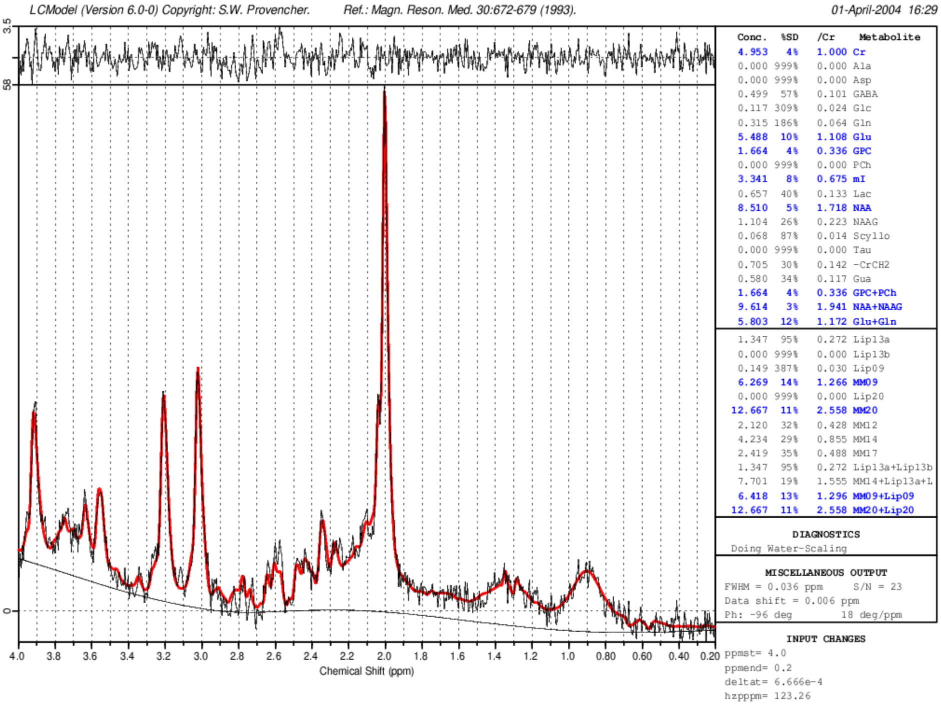

```
LCModel (Version 6.0-0) Copyright: S.W. Provencher.     Ref.: Magn. Reson. Med. 30:672-679 (1993).     01-April-2004  16:29

  Conc.  %SD   /Cr   Metabolite
  4.953   4%   1.000 Cr
  0.000 999%   0.000 Ala
  0.000 999%   0.000 Asp
  0.499  57%   0.101 GABA
  0.117 309%   0.024 Glc
  0.315 186%   0.064 Gln
  5.488  10%   1.108 Glu
  1.664   4%   0.336 GPC
  0.000 999%   0.000 PCh
  3.341   8%   0.675 mI
  0.657  40%   0.133 Lac
  8.510   5%   1.718 NAA
  1.104  26%   0.223 NAAG
  0.068  87%   0.014 Scyllo
  0.000 999%   0.000 Tau
  0.705  30%   0.142 -CrCH2
  0.580  34%   0.117 Gua
  1.664   4%   0.336 GPC+PCh
  9.614   3%   1.941 NAA+NAAG
  5.803  12%   1.172 Glu+Gln

  1.347  95%   0.272 Lip13a
  0.000 999%   0.000 Lip13b
  0.149 387%   0.030 Lip09
  6.269  14%   1.266 MM09
  0.000 999%   0.000 Lip20
 12.667  11%   2.558 MM20
  2.120  32%   0.428 MM12
  4.234  29%   0.855 MM14
  2.419  35%   0.488 MM17
  1.347  95%   0.272 Lip13a+Lip13b
  7.701  19%   1.555 MM14+Lip13a+L
  6.418  13%   1.296 MM09+Lip09
 12.667  11%   2.558 MM20+Lip20

           DIAGNOSTICS
 Doing Water-Scaling

      MISCELLANEOUS OUTPUT
FWHM = 0.036 ppm      S/N = 23
Data shift = 0.006 ppm
Ph: -96 deg         18 deg/ppm

          INPUT CHANGES
ppmst= 4.0
ppmend= 0.2
deltat= 6.666e-4
hzpppm= 123.26
```

Fig. 3.18 The standard ‘one page output’ showing the results of the LCModel analysis. The fit of the spectrum is shown by the thick line and the baseline by the solid black line under the fitted spectrum. The residuum is shown in the upper part of the figure. On the right the estimated concentrations along with Cramer-Rao bounds and the ratio to Creatine are shown for all metabolites in the basis set.

4 Experimental part

4.1 Description of the program CULICH

An accurate determination of the metabolite signals in the spectrum is a basic block of each analysis of *in vivo* MR spectra. Therefore, a tool allowing reliable and automatic processing of SI data is of high importance for the clinical application of SI. In principle, any program enabling single voxel spectra processing can be adopted for SI data evaluation. However, specific requirements on the SI processing programs exist. Firstly, the program has to allow data processing in a batch mode, i.e. the repeated processing of several spectra without any user intervention. Secondly, the program has to allow the display of the spectroscopic grid and calculated metabolic maps overlaying the anatomical images of the measured sample. Although various spectra processing programs are provided by vendors with the scanner computers, software allowing complete SI data processing is not available.

Based on all the technical requirements for an efficient processing tool, the CULICH program (72) enabling comprehensive and reliable SI data processing has been developed. CULICH was programmed in the MATLAB language, supporting efficient manipulation of matrixes and arrays in which all images and spectra are represented. For the spectra fitting itself, a commercially available program LCModel (73), dedicated originally for single voxel spectra analysis, was used. CULICH represents a SI data-LCModel graphical interface, where all data manipulations and corrections are performed and where the display of various parametric maps and their follow up analysis is possible. Although LCModel is capable of processing SI data sets on its own, it lacks any possibility of spectra pre-processing and does not support the display of anatomic images. The modular philosophy of CULICH enables easily including new data formats (SI data formats of various vendors) as well as the possibility of the substitution of LCModel with another program suitable for spectra processing.

4.1.1 The block scheme of CULICH

The basic schematic diagram of the CULICH is depicted in Fig. 4.1, where three main functional blocks can be recognized: 1) the automatic download of the spectra and anatomic high resolution images from the scanner, 2) SI data preprocessing and initiation of LCModel processing, 3) the automatic download of results of the LCModel fitting, their viewing and analysis.

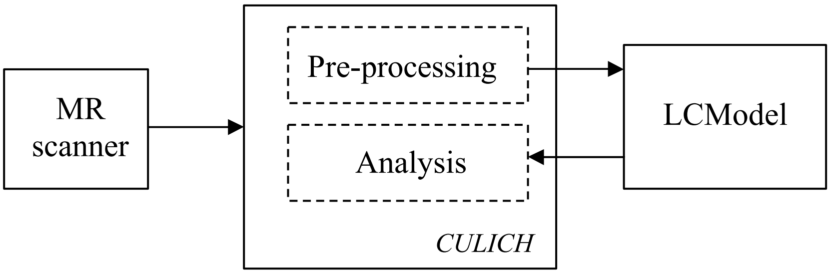

Fig. 4.1 The block scheme of the program CULICH

4.1.2 Data download from the MR scanner

Depending on the scanner manufacturer, as well as the archiving strategy used in the particular place of work, the data can be stored in various formats and disk spaces. FTP data transfer protocol or direct data download from the mapped drive can be utilized in CULICH. If several scanners for SI measurements are used, the possibility to select the corresponding MR scanner assures the initiation of the appropriate module for the data download. The required data is then uploaded to CULICH and the raw data in the scanner can be deleted. Additional data import from a specified folder is also possible. This approach makes CULICH versatile in terms of communication with various scanners.

After the data have been transferred from the scanner, the spectroscopic grid and the pre-selected volume (in case of spatially pre-selected SI sequences) overlaying the three orthogonal anatomical images are displayed in CULICH (Fig. 4.2). The visualization of SI datasets of arbitrary orientation is supported. The anatomical images are downloaded automatically if the identification of the corresponding images is available in the header of the SI data. Zooming, windowing and an exchange of anatomical images are possible.

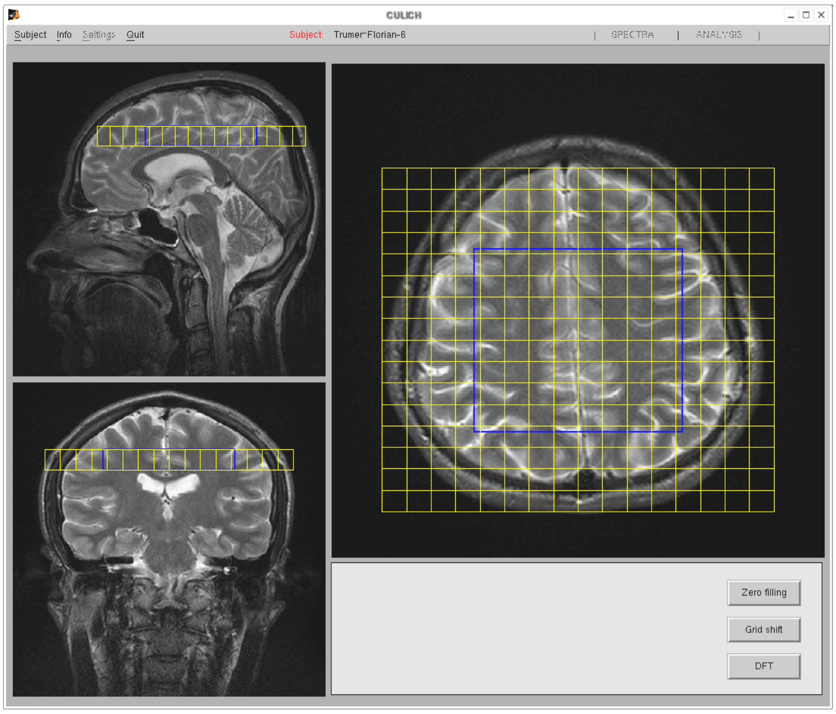

Subject: Trumer^Florian-6

Fig. 4.2 The uploaded SI data in CULICH. A spectroscopic grid overlaying base images is displayed. Further data pre-processing is controlled using the buttons as well as through the program menu.

4.1.3 Spectra pre-processing and initiation of the LCModel analysis

Prior to the fast Fourier transform of k-space data into the spatial domain, the grid shifting, zero filling (available in each direction independently) and k-space filtering using various window functions are selectable. Each pre-processing step is documented in the attached information file. Therefore, one spectrum can be processed repeatedly using different pre-processing parameters. Performed adjustments to the position of the spectroscopic grid and the applied zero filling are directly visible on the screen (Fig. 4.3) After the fast Fourier transform from time to frequency domain, spectra from particular voxels of the spectroscopic grid can be viewed (Fig. 4.4). All standard parameters for spectra display can be adjusted. Additionally, several auxiliary features such as hiding of the spectroscopic grid or display of the map of absolute spectra help to plan the processing by LCModel. For the possibility of evaluating the selected spectrum using an external processing program, the spectrum can be exported in the specified format.

When the LCModel processing is activated, LCModel parameters, such as basis set selection, can be adjusted if the default parameters are not suitable. Optionally, eddy current correction, initial spectra phasing, data filtering or zero filling can be performed prior to LCModel processing. One voxel or voxels in a specified region can be selected for LCModel processing. After evoking the LCModel analysis, data are formatted into the file format required by LCModel and the reference to the spectra to be processed is copied to the queue file controlling LCModel batch processing. This approach enables the processing of several SI datasets without any user intervention and it also enables the multi-user capability of CULICH.

Although CULICH is based on LCModel processing, the block architecture of CULICH enables the use of other processing programs without substantial changes in the code.

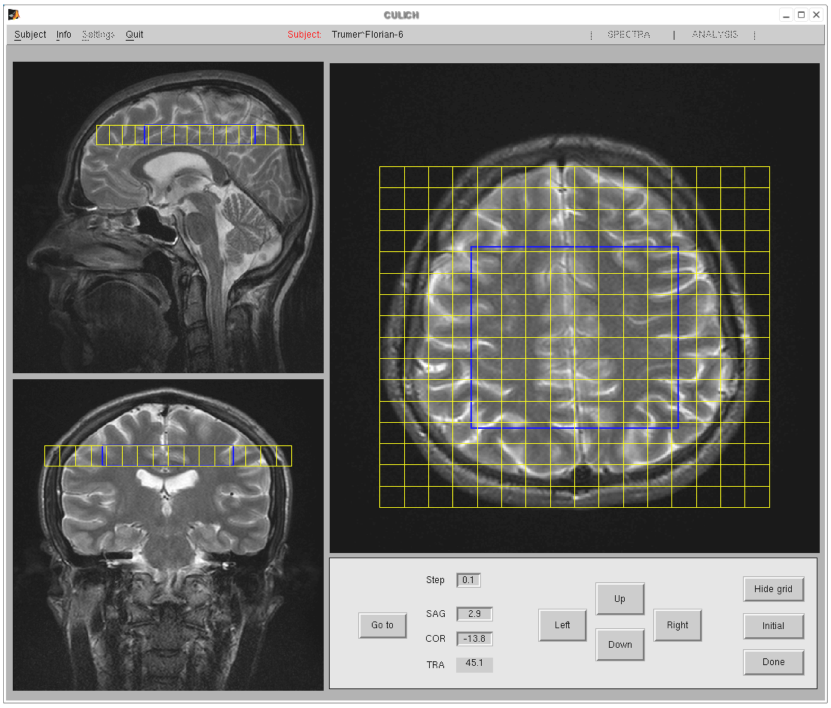

Subject: Trumer^Florian-6
Step 0.1
SAG 2.9
COR -13.8
TRA 45.1

Fig. 4.3 The grid shifting. Position of the grid can be interactively changed using navigation buttons. The coordinates in the scanner coordinate system are displayed.

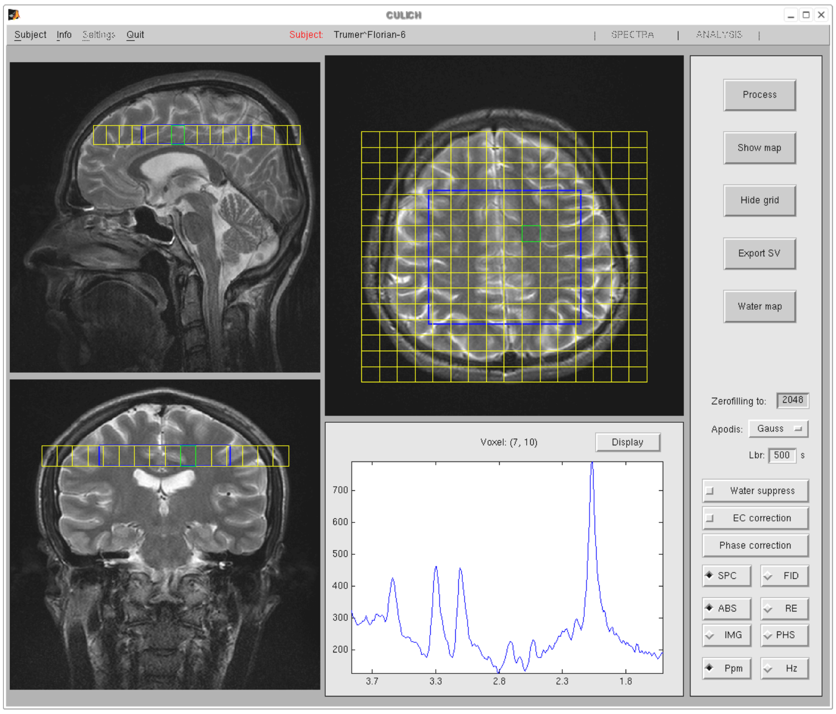

Subject: Trumer^Florian-6

Zerofilling to: 2048

Apodis: Gauss

Lbr: 500 s

Fig. 4.4 The SI data after spatial FT. The spectrum from a selected voxel is viewed. LCModel processing of the selected voxels can be initialized by the 'Process' button.

4.1.4 Viewing and analyzing results

Spectra processed by LCModel are saved in a sequence as they are processed on the disk and the fitted spectra can be viewed regardless of whether the processing of all voxels within one analysis had been finished. The analysis window consists of two main folders: 1) the SPECTRA folder allows the displaying of the fitted spectra and calculated concentrations and 2) the ANALYSIS folder enables the calculation of metabolite images and additional parametrical maps. Information about concentrations of metabolites and their Cramer-Rao bounds along with other parameters such as signal-to-noise ratio, applied phase correction or correlation coefficients between metabolites are available in the SPECTRA folder. Phased spectra, fitted spectra, residua, baseline or individual fitted components can be displayed (Fig. 4.5). Corrections for the non-ideal excitation profile of the *VOI* and for partial volume effects can be optionally performed based on the image of the VOI profile and the segmented image of the examined tissue provided by the user. In the ANALYSIS folder the calculation of metabolite and error images (Fig. 4.6) or the display of the spectral map (Fig. 4.7a) and of bar graphs map (Fig. 4.7b) are available. In the metabolite image window, a metabolite image of the specified metabolite or a ratio of metabolites can be viewed.

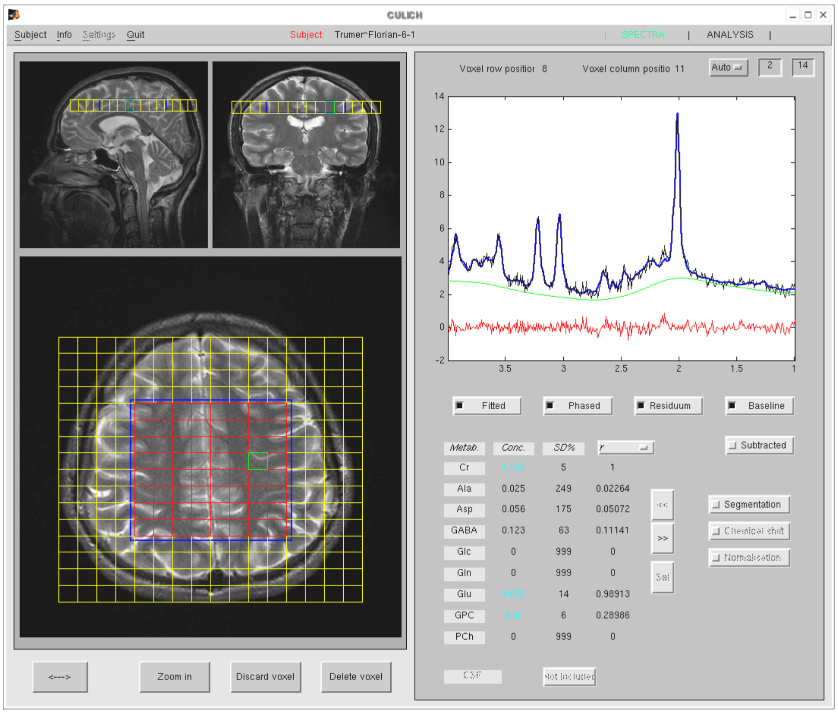

Subject: Trumer^Florian-6-1

Voxel row positior 8

Voxel column positio 11

Metab.	Conc.	SD%	r
Cr	1.104	5	1
Ala	0.025	249	0.02264
Asp	0.056	175	0.05072
GABA	0.123	63	0.11141
Glc	0	999	0
Gln	0	999	0
Glu	1.092	14	0.98913
GPC	0.32	6	0.28986
PCh	0	999	0

Fig. 4.5 The SPECTRA folder of the result window. The result of the LCModel analysis for the selected voxel (green rectangle) is shown. Calculated voxels are depiced in red and the excited *VOI* by the blue rectangle. A phased spectrum (in black), a fitted spectrum (in blue), a residuum (in red) and a baseline (in green) are viewed in the spectrum window. Calculated concentrations of metabolites, their *CRBs* and ratio values with respect to the selected metabolite are displayed.

Along with the metabolite image, an error image based on the Cramer-Rao bounds (*CRBs*) is shown in the neighbouring window (76). Both images overlay the anatomical image. The apparent resolution of the metabolite and error images can be improved by bilinear or cubic interpolations. The transparency, a colour map and colour scaling can be adjusted both for metabolite and error images independently. The low and high threshold values can be adjusted for each image to display only areas of the image with concentration/error values within a specified threshold range. The mask of the selected error image can be applied to the metabolite image to display only areas of the metabolite image with the specified errors. Error of the calculated concentrations can also be expressed as a transparency of the metabolite image. Although the user can freely switch between the ANALYSIS and SPECTRA windows without loosing the contents of the windows the possibility to view the spectra by clicking directly on the metabolite image has been implemented. In addition to the error image other parametric maps such as signal-to-noise ratio map, linewidth map, zero and first order phase correction map or map of the spectra shifts (B0 homogeneity map) can be shown.

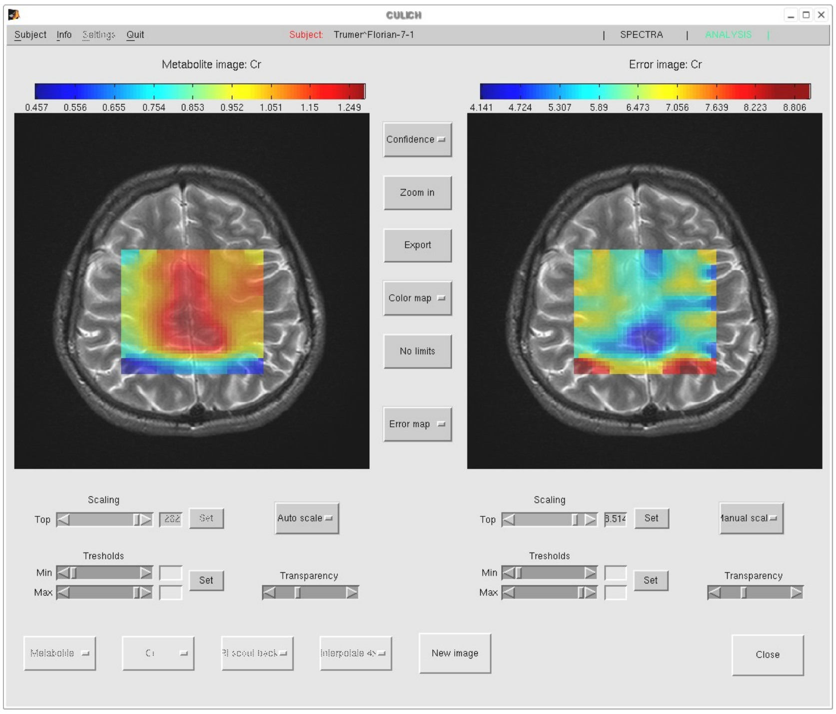

Fig. 4.6 Calculation of metabolite and error images in the ANALYSIS window. The metabolite and error images overlying an anatomical image are displayed simultaneously. The error image can be optionally replaced by other parametric maps.

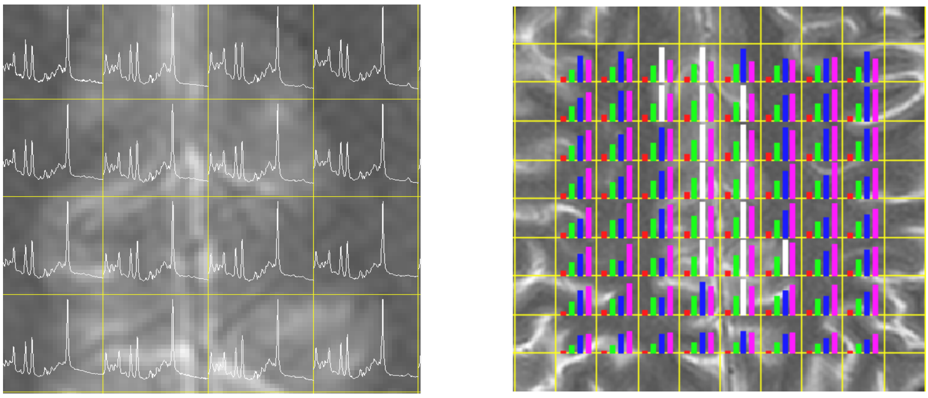

(a) (b)

Fig. 4.7 Additional maps available in the program CULICH. A conventional spectral map (a). The LCModel fits are shown. A bar graphs map (b). The concentration of metabolites in each voxel are depicted as the height of the corresponding bar graph. In the example shown red=Cho, green=Cr, blue=GLX, violet=NAA. When the concentration of some metabolite exceeds the maximum value, the corresponding bar graph appears in white.

4.1.5 Possibilities and limitations of CULICH

The extensive use of MR scanners for routine MR examinations makes the time available for the processing of acquired data directly at the MR host computer or at the dedicated data processing consoles limited. Therefore, the possibility to run a processing program separately on a personal computer is advantageous. Also, the possibility of the simultaneous execution of CULICH on several computers in parallel enhances the efficient use of the program.

There are two major measures characterizing the efficiency of the processing method: the accuracy of the calculated concentrations and the time required for the analysis. For spectra fitting, CULICH makes use of LCModel (see the description of the LCModel program in section 3.9.11), which is among the cutting-edge processing programs in the field of *in vivo* MR spectroscopy. Since the spectra processing in CULICH is performed in the voxel-by-voxel fashion, the number of voxels to be processed is a determining factor for the evaluation time. The number of required voxels depends on the nature of the examined disorder. In the case of diffuse brain disorders spectra from a large area are usually evaluated, whereas more focused areas are measured in cases of localized lesions. However, generally up to 100 voxels need to be processed in one subject. The complexity of the LCModel evaluation is reflected in the calculation time. The usual processing time of one spectrum is at least 20 seconds, usually longer. On the other hand, several LCModel processes can be run in parallel, each of them processing part of the voxels. The time required for the processing of one spectrum can also be reduced by initial spectrum phasing and referencing prior to LCModel analysis. Generally, the computation time is influenced mainly by the spectra quality. Therefore, when high quality spectra are acquired, the processing time can be significantly reduced. It should be pointed out that due to the nature of the disorders indicated for SI examination the speed of the data evaluation is not a critical limitation. Therefore, the longer processing time means no real constraint in clinical SI and it is fully offset by the resulting quality of the fits.

An example of the evaluated spectroscopic image by CULICH is shown in Fig. 4.8. In that image a metabolite image of glutamate + glutamine (GLX) from an axial slice through the human brain above the ventricles is shown. The measurement parameters were as follows: 1.5T, PRESS SI sequence, matrix 32x32, *FOV* 160x160 mm, 4 Hamming filtered averages, *TE* 30 ms, *TR*=1600 ms. Due to the used high resolution of SI data and the ability of LCModel to accurately fit GLX resonances, the different GLX distribution in *WM* and *GM* can be seen in agreement with the literature (54)

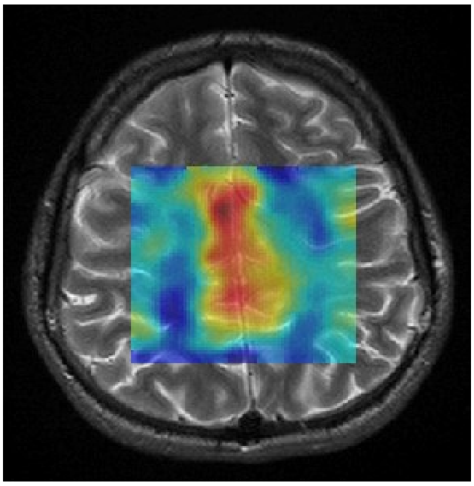

Fig 4.8 The spectroscopic image of glutamate + glutamine (GLX).

4.2 Comparison of concentrations calculated by SI and SVS

Compared to single voxel spectroscopy, spectroscopic imaging is more advantageous in obtaining information about metabolite distribution over a large volume of interest. On the other hand, obtaining high quality spectra by means of SI techniques is more problematic (77-80). The existence of point spread function (*PSF*) is a principal issue when estimating absolute concentrations by means of SI. As explained in the theoretical section, the actual signal contamination depends not only on the *PSF* shape, but also on the distribution of the metabolites in the sample. Moreover, due to the oscillatory character of the *PSF* the effective voxel size is generally different from the nominal voxel size. The application of the k-space filters diminishes the influence of the *PSF*, but at the price of the lower resolution. The question then arises whether the quantitative SI, based on the assumptions of the known voxel size and the proportionality between the measured signal and the concentration of metabolites, is possible. The estimation of absolute concentrations of metabolites using SI sequences has been performed in several studies (81-86). However, no direct comparison of concentrations of metabolites *in vivo* measured both by CSI and SVS (representing the gold standard for the calculation of concentrations) from the corresponding voxels has been shown. In this study a comparison of concentrations of metabolites obtained by both techniques from spatially matched voxels is performed and the role of k-space filtering for the result of the comparison is discussed.

4.2.1 Methods

MR examinations were performed on a Siemens Vision 1.5T whole body imager with a standard CP head coil. The protocol of MR imaging included *T2* weighted sagittal, coronal, and transverse images obtained by a turbo-spin echo imaging sequence (*TR*/*TE*=5400/99 ms, 1 acquisition, slice thickness 5 mm). The MR images were used for the localization of volume of interest (*VOI*). The MR spectra were measured both by SVS ^{1}H PRESS sequence (*TE*/*TR*/*NA*=135ms/1500ms/256) and proton 2D volume pre-selected ^{1}H PRESS-SI sequence (*TE*/*TR*/*NA*=135 ms/1500 ms/1, 16x16 voxels, *FOV*=160 mm x 160 mm, transversal orientation), slice thickness 20mm. The nominal SVS and SI voxel sizes were both 10 mm x 10 mm x 20 mm=2 ml.

The spectrum measurement protocol consisted of the global shimming (automatic, using an implemented MAPSHIM procedure), *VOI* selection (Fig. 4.9), local shimming of the field in the *VOI* and the water suppression adjustment followed by the spectrum measurement. The spectra were sampled to 1024 time points. The carrier frequency was set on the water resonance at 4.7 ppm. The water suppression was accomplished by CHESS pulse (Gaussian shape, half-width 50 Hz). All slice selective excitation pulses were Hamming filtered sinc pulses (duration 5120 μs, sampled to 512 time points) of variable bandwidth, applied with the fixed gradient strength.

13 healthy volunteers were examined by both SVS and SI sequences to compare both methods. Shimming was performed on SVS and SI volumes separately. The spectra were measured from the regions of the white mater (Fig. 4.9). All volunteers were informed about the experiment and provided written consent in accordance with the local ethical committee rules.

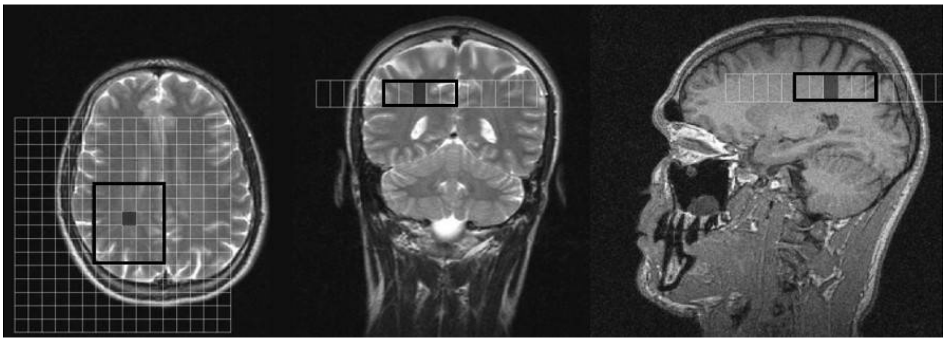

Fig 4.9 Typical positions of the pre-selected volume (big black rectangle) in SI experiment and the single voxel in SVS experiment (small gray colored rectangle).

Single voxel spectra were processed by LCModel and SI spectra were processed by CULICH software also using LCModel. In both cases the LCModel basis set was acquired from SVS measurements. The basis set calibration phantoms contained a water solution of N-acetyl aspartate (NAA), Creatine (Cr), Choline (Cho) and Lactate (Lac) in concentrations of about 50-100mM and were prepared according to Provencher (87). In SI data LCModel analysis the voxel size was set to nominal voxel size 2 ml, regardless the filter function used. In all measurements only NAA, Cr and Cho resonances were evaluated. Each SI data set was processed four times. First time with no k-space filter and remaining times with the applied Hamming filters $0.54+0.46\cos(2\pi l)$ in both dimensions; with l in the range of Filter 1: l= -0.25 to 0.25; Filter 2: l= -0.375 to 0.375; Filter 3: l= -0.5

to 0.5. The application of the filters lead to the resulting resolution: 12.1 mm (Filter 1), 15.3 mm (Filter 2) and 19.5 mm (Filter 3), computed according to Eq. [3.26].

For all comparisons, the spectra from SI and SVS voxels at the same position were acquired. The exact matching of the SVS and the SI voxels was achieved by the post acquisition adjustment of the Coronal and Sagittal SI grid coordinates in CULICH. In cases of the evaluation of *in vivo* spectra, the grid position was shifted for every metabolite separately, according to Eq. [3.40], to account for the chemical shift artifact. In our case, using SVS gradients 2 mT/m in all directions, these shifts were: d_{NAA}=2.0 mm, d_{CR}=1.3 mm, d_{CHO}=1.1 mm.

To prevent signal alteration due to possible excitation profile imperfections, only the voxels in the middle of the excited *VOI* whose distance from the edge of the SI pre-selected volume was at least two voxels were processed.

In vivo concentrations were calculated in the arbitrary units with the correction for relaxation effects using values *T1*: NAA=1300 ms, Cr=1800 ms, Cho=1700 ms; *T2*: NAA=368 ms, Cr=185 ms, Cho=425 ms according to Christiansen et al. (88).

4.2.2 Results

The means of concentrations of metabolites in the arbitrary units as well as the metabolite ratios measured both by SVS and SI sequences in 13 healthy volunteers are, along with their corresponding confidence intervals (level of confidence 95%), shown for all reconstructions (k-space filters) performed in Table 4.1. To compare SI and SVS evaluation methods, t-test preceded by F-test was performed between each SI reconstruction data set and SVS data set both for metabolite ratios and absolute concentrations. T-test did not show any significant differences in absolute concentrations, but shown significant differences in ratios Cho/Cr (no filter) and NAA/Cho (filter f3) when no *CSA* correction was performed and ratios Cho/CR and NAA/Cr (both no filter) when *CSA* correction was performed.

The errors of the concentration estimations provided by LCModel ranged up to 20% for all evaluated metabolites.

	Cho	Cr	NAA	Cho/Cr	NAA/Cr	NAA/Cho
SVS	3.0(0.2)	12.3(0.8)	12.5(1.2)	0.25(0.02)	1.0(0.1)	4.1(0.3)
CSI	3.2(0.3)	10.6(1.3)	12.1(0.9)	0.31(0.03)	1.2(0.1)	3.8(0.2)
CSI-f1	3.1(0.2)	11.6(1.1)	12.4(0.9)	0.27(0.02)	1.1(0.1)	4.1(0.2)
CSI-f2	2.9(0.2)	12.2(1.2)	12.6(1.0)	0.24(0.01)	1.04(0.05)	4.3(0.2)
CSI-f3	2.8(0.2)	12.5(1.1)	12.7(0.9)	0.23(0.01)	1.02(0.05)	4.5(0.2)

(a)

	Cho	Cr	NAA	Cho/Cr	NAA/Cr	NAA/Cho
SVS	3.0(0.2)	12.3(0.8)	12.5(1.2)	0.25(0.02)	1.0(0.1)	4.1(0.3)
CSI	3.2(0.3)	10.5(1.4)	12.6(1.0)	0.31(0.04)	1.2(0.1)	4.0(0.3)
CSI-f1	3.1(0.3)	11.5(1.1)	12.5(1.1)	0.27(0.02)	1.1(0.08)	4.1(0.2)
CSI-f2	2.9(0.2)	12.4(1.2)	12.8(1.0)	0.24(0.02)	1.04(0.05)	4.4(0.3)
CSI-f3	2.9(0.3)	12.5(1.1)	12.6(0.9)	0.23(0.02)	1.01(0.05)	4.4(0.3)

(b)

Table 4.1 Means of concentrations of metabolites in vivo in arbitrary units as well as metabolite ratios measured both by SVS and SI sequences in 13 healthy volunteers along with their corresponding confidence intervals (level of confidence 95%) for the case when no *CSA* correction (a) and *CSA* correction were performed (b). F1, f2, f3 stand for three k-space filters used.

4.2.3 Discussion

Although both SVS and SI techniques measure the signal from the selected voxel, due to a different nature of both methods different voxel profiles (voxel volume and size) have to be generally expected. Neglecting a slice profile of the pre-selection *VOI*, the phase encoding assures the orthogonal voxel shapes in phase encoding directions. In contrast, non-ideal pulse profiles determine the voxel shape/volume in SVS in all dimensions, similarly to the pulse profile in the slice direction in 2D SI. Considering further *PSF* effect, the localization of SI and SI techniques is, strictly taken, not equivalent. However, to be able to calculate the concentrations of metabolites, assumptions about the rectangular voxel shape are made in SVS and SI experiments. Therefore, the presented comparison questions whether the SI and SVS give the same results assuming the perfect localization of both methods. As apparent from Table 4.1a and Table 4.1b, *CSA* correction affected calculated concentration only to a small extent. This could be explained by small *CSA* related shifts in our experiment and by the fact that voxels were positioned in homogeneous areas. The highest difference before and after the correction was observed in NAA concentrations, apparently due to the highest *CSA* related shift. In case of Creatine, where resonances both from CH_3 and CH_2 groups contributed to the resulting metabolite signal, the frequency of the stronger resonance (CH_3 at 3.01 ppm) was used for the *CSA* correction. This shortcoming could explain observed significant difference between SVS and SI results for ratios of metabolites with CR even after *CSA* correction. Since SI was measured by two dimensional PRESS-SI sequence with the transversal orientation and since different transversal selection gradients for SVS and SI were used, the shift perpendicular to the transverse plane remained uncorrected. The chemical shift artifact can be eliminated by the proper adjustment of the excitation frequency, however, this was not in our measuring sequence possible.

Although not significantly different from SVS values, SI concentrations vary depending on the k-space filter used. It is obvious that *PSFs* associated with particular k-space filters lead to the different resolution and an effective voxel volume measured. However, no significant differences between concentrations corresponding to particular k-space filters were found. Since 'strong' k-space filtering leads to the high decrease of resolution, the filter 2, representing moderate filtering, is most suitable. The application of the k-space filters lead further to the decrease of fitting errors of SI spectra. This can be understood, since due to the filter effect, a smaller region with better magnetic field homogeneity contributes to the signal.

In the presented study no excitation slice profile correction was applied. The excitation profile is especially distorted at the edges of the excited slice. For that reason, only voxels, in the middle of the *VOI* and having the distance from the edge of the excited volume at least two voxels, were selected. The inspection of pulse profiles showed that in such an arrangement, the pulse flip angle in the measured SI voxel can be assumed constant and equal to the nominal flip angle.

It should be noted that, as a consequence of volume pre-selection, *PSF* of the volume pre-selected SI differ from *PSF* of the SI sequence without the pre-selection. It is a consequence of the fact that an area from which a potentional contamination may arise is determined by the *VOI* size. This implies that the signal (and thus the spectra contamination) generally depends on the size of the pre-selected VOI and, therefore, may vary among the subjects if the VOI size is variable.

For example, for the signal *S(0)* measured from the central SI voxel under the assumption of a unit concentration in the sample, for a 1D SI experiment we can write

$$S(0) = \int_{-FOV/2}^{FOV/2} P(x)PSF(x)dx \qquad [4.1]$$

where *FOV* stands for the field of view and *P*(*x*) describes the profile excited during the volume pre-selection. In the ideal case, when *P*(*x*) is the rectangular function equal 1 for *x* in the interval (–*L*/2, *L*/2) and 0 elsewhere (*L* is the size of the *VOI*), the Eq. [4.1] can be simplified

$$S^{id}(0) = \frac{FOV}{N}\sum_{n} \frac{p_n \sin(\pi n VOI/FOV)}{\pi n} \qquad [4.2]$$

A Formula for *PSF* for symmetrical k-space sampling according to Eq. [3.15] was used to calculate Eq. [4.2]. The generalization of the Eq. [4.2] to two and three dimensional Cartesian sampling is given by the product of the corresponding expressions in Eq. [4.2]. Due to a oscillating character of the *PSF* we can expect modulation of the measured signal according to the size of the pre-selected *VOI* (see Fig 4.10).

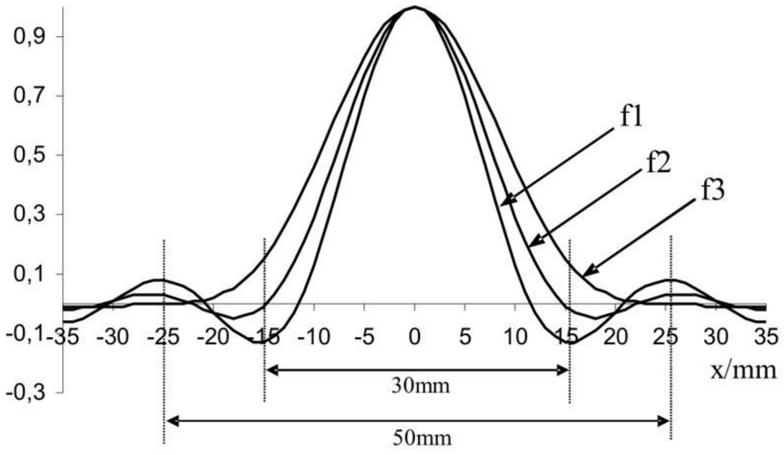

Fig 4.10. Volume pre-selection results in the restriction of area from which signal contamination can exist. Due to the different *PSF* shape as a result of k-space filtering, the signal measured for the given volume size differs for particular filters used.

The dependence of the *S*(0) on the *VOI* dimension *L* is for different k space filtering shown in Fig 4.11a. As apparent from the figure, the dependence is pronounced especially when no k-space filtering is used and it can be eliminated by the stronger k-space filtering. This behavior was confirmed by measurements of the signal in the uniform phantom (50 mM

Acetate) from the centered voxel with varying squared *VOI* size, as shown in Fig. 4.11b. The deviations from the theoretical dependence, shown in Fig. 4.11a, can be ascribed to the different assumed excitation profiles (ideal rectangular in Fig. 4.11b, but real nonrectangular in Fig. 4.11a).

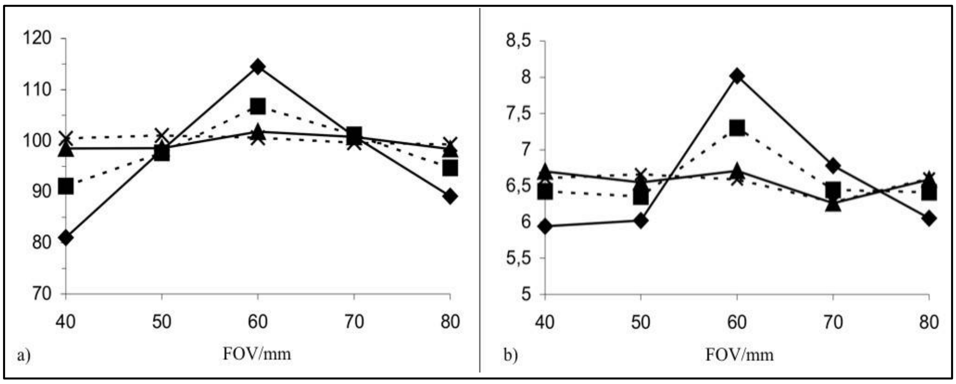

Fig 4.11 Theoretical a) and experimental b) dependence of the signal strength from the central voxel of SI grid on the size of the squared pre-selected volume ranging from 80 x 80 mm to 40 x 40 mm in the homogeneous phantom. Particular curves correspond to the different k-space filters used as follows: ♦ no filter, ■ filter1, ▲ filter 2, x filter 3.

The dependence of the measured voxel, as described by Eq. [4.2], holds true only for a constant concentration metabolites and the central voxel. Therefore, in *in vivo* measurements, the signal behaviour will be generally different. However, the signal measured in each voxel will still depend on the *VOI* dimensions. Assuming the variable *VOI* sizes in the group of measurements the corresponding signal modulation may exhibit mainly as an increase of standard deviations of calculated concentrations. Keeping the *VOI* dimensions constant within one study may, therefore, increase the accuracy of calculated concentrations. The effects are less pronounced when stronger k-space filtering is applied. In the presented study the *VOI* size was changed only minimally (typical size 50x60 mm).

Due to the matched position of SVS and SI voxels no segmentation of the brain tissue was performed. The influence of *PSF* to the effective content of *CSF* in the SI voxel, as described in section 3.9.6, was neglected due to the positioning of the measured voxels in the region distinct from the areas with high *CSF* content.

Values of the absolute concentrations given in Table 4.1 are higher than those in the literature (46). This is caused by the fact that no relaxation correction was performed for the metabolites in the basis set since relaxation times *in vitro* were not measured. In this respect concentrations given in Table 4.1 should be considered as in arbitrary units. However, since the same echo time *TE*=135 ms and the repetition time *TR*=1500 ms for the SVS and SI sequences were used, relaxation corrections were not necessary for the comparison of the methods.

For the proper spectra evaluation, the correct acquisition of the LCModel basis set is essential. For SI data evaluation, the basis set acquired by single voxel spectroscopy sequences has been used exclusively (54,89). Even though the measurement of the basis set by the single voxel sequence is straightforward, the above mentioned *PSF* related effects as well as non-equivalent voxel profiles may lead to discrepancies between signal strengths from the SI voxels and the SVS voxel used in the basis set. In addition to that the sensitivity of the coupled spins both to the experienced flip angle (variations in excitation profiles) and the echo spacing in PRESS sequence may lead to further signal changes (90). However, the coupled resonances were not in this study examined. An alternative approach could be to measure the basis set from the signal of the representative SI voxel instead of the SVS voxel. Nevertheless, the same SI data acquisition and processing techniques would be required whenever using this basis set to assure the consistent *PSF* shape. Being aware of these discrepancies the SVS basis set for the SI data evaluation was used in this study. For many MR laboratories this is the method of choice since ones acquired SVS basis set need not to be measured again. It should be noted that the effects related to the excitation profile of the voxel are neglected also in the LCModel evaluation of SVS spectra when one basis set for various voxel sizes is used. The used experimental basis set contained NAA, Cr, Cho and Lac. Although there are also other metabolites present in the brain, their signal contributions to the measured spectra and their influence on LCModel fitting of the observed metabolites are at the echo time *TE*=135 ms in healthy brain negligible. The only exception could be Inositol, however its omission in the basis set did not lead to any distortion in the Choline region and did not affect the overall fit quality.

Since SVS and SI sequences were not identical in terms of encoding and crusher gradients, the different out of volume contamination as well as the different diffusion weighting of the signal acquired by both sequences can also influence the comparison.

4.2.4 Conclusions

In the presented study concentrations of metabolites in human brain measured both by single voxel and spectroscopic imaging techniques from spatially matched voxels and processed by LCModel program were compared. In the experimental and processing arrangement used no differences in the metabolite concentrations were observed. Similarly, no differences in concentration ratios were observed when mild k-space filtering was performed. The application of k-space filter helps to diminish *PSF* effect, such as contamination with the signal from neighboring voxels or the dependence of the observed signal on the pre-selection volume size and leads to the lower errors of the spectra fits. Although none of the applied filters broke the agreement of concentration values, to keep resolution in reasonable limits proper filter 'strength' should be used. Keeping in mind above mentioned effects spectroscopic imaging by LCModel can be used for quantitative studies of the metabolites present in human brain.

4.3 The importance of relaxation corrections for quantitative SI

Diagnostics using MR spectroscopy are based on the comparison of the concentrations of metabolites measured in the examined patient and the control values estimated in a group of healthy volunteers. When calculating the concentrations of metabolites from spectra with long echo time and short repetition time, the corrections for relaxation times according to Eq. [3.35a] and Eq. [3.35b] should be performed. The exact correction for relaxation effects requires knowledge of relaxation times $T1$ and $T2$. However, various $T1$ and $T2$ relaxation times can be found in the literature (46). This fact reflects the low accuracy of the estimated relaxation times as well as possible natural $T1$ and $T2$ variations among the subjects. The situation is even more problematic in patients. Although a change in the relaxation times is expected as a result of a brain disorder, the time constraints usually do not allow additional examinations to assess relaxation times in patients and therefore relaxation times estimated in healthy controls are used also for the correction of data from the patients. Because the inexact values of relaxation times introduce an error in calculated concentrations, the question arises whether the calculated concentration values reflect in the given case the change in the concentration or in the relaxation times. The estimation of the impact of errors in $T1$ and $T2$ values to calculated concentrations of metabolites is subject to this study.

4.3.1 Impact of the inaccurate knowledge of *T1* and *T2*

Due to statistical evaluation, the concentrations of metabolites in the control group are estimated with finite statistical errors. The significant difference of the calculated concentration from the control value may be caused both by the different concentration of the metabolite or by the mismatch between the true $T1$ and $T2$ values and the values used for the relaxation correction in the patient. For these consideration and their clinical utilization, it is helpful to know how the original value of relaxation times must change (at a constant metabolite concentration) for the calculated concentrations to differ significantly from control value. Due to a multiplicative character of f_{T1} and f_{T2} the influence of $T1$ and $T2$ relaxation times corrections can be treated separately.

Influence of T2 value

Starting with a correction for $T2$ relaxation f_{T2} and assuming the control value of the measured concentration (without a correction to in vivo metabolites relaxation times) for a given sequence can be expressed as $C \pm a$, where a represents error of the estimation of C, the above condition can be described as

$$\frac{C}{f_{T2'}} = \frac{(C \pm a)}{f_{T2}} \qquad [4.3]$$

where $T2'$ is the changed value of relaxation time $T2$. $T2'$ can thus be expressed as follows

$$T2' = \frac{T2\,TE}{TE - T2 \ln(C/(C \pm a))} \qquad [4.4]$$

specifically, if looking for a $T2'$ at which the concentration changes by x percent of the original value,

$$T2' = \frac{T2\,TE}{TE - T2 \ln(100/(100 \pm x))} \qquad [4.5]$$

For the given experimental design, it has to be considered, using Eq. [4.4] and Eq. [4.5] , whether or not the change in the magnitude of the signal being measured can be related solely to the change in relaxation time $T2$. In the case of TE=136 ms, representing often used long echo time, the 10% increases and decreases in concentrations correspond to following $T2'$ values: *NAA* ($T2$=368 ms): $T2'$=292 ms and 516 ms, *Cr* ($T2$=185 ms): $T2'$=164 ms and 216 ms, *Cho* ($T2$=425 ms): $T2'$=327 ms and 636 ms, respectively.

Further consequences of the inaccurate knowledge of $T2$ values for the comparison of concentrations measured with short and long echo times can be found in the paper by Jiru et al. (91).

Influence of T1 value

The identical analysis can be performed for the correction factor f_{T1}. The condition analogous to the Eq. [4.3] can be for the PRESS sequence described as

$$\frac{C}{f_{T1'}} = \frac{(C \pm a)}{f_{T1}} \qquad [4.6]$$

where *T1'* is the changed value of the relaxation time *T1*. *T1'* can thus be expressed as follows

$$T1' = \frac{TR}{\ln(100 \pm x) - \ln(100e^{-\frac{TR}{T1}} \pm x)} \qquad [4.7]$$

The mixing time *TM* is in STEAM sequences usually about 5-10 ms. Assuming a typical *T1* time *T1*=1500 ms and typical *TR* time in SI sequences *TR* =1500 ms, the term $e^{-TM/T1}$ equals 0.99 and it can be neglected to the term 1- $e^{-TR/T1}$. In this approximation Eq. [4.7] can be used both for PRESS and STEAM sequences. In case of *TR*=1500 ms, representing often used repetition time, the 10% increases and decreases in concentrations correspond to following *T1'* values: *NAA* (*T1*=1300 ms): *T1'* =1049 ms and 1540 ms, *Cr* (*T1*=1800 ms): *T1'* =1516 ms and 2079 ms, Cho (*T1* =1700 ms): *T1'* =1424 ms and 1971 ms, respectively. The *T1* and *T2* values were adopted from (88).

4.3.2 Discussion and conclusions

Due to the multiplicative character of f_{T1} and f_{T2} in the resulting correction f_T, it follows that if both corrections are not negligible, the change in the f_{T1} factor can be offset by the change in the f_{T2} factor and vice versa, which makes the exact interpretation of the signal changes a complex problem. If a metabolite has several resonances (e.g. CH_3, CH_2, and CH groups), the relaxation times of individual resonances are generally different. As a result, corrections to relaxation times should ideally be made separately for each resonance. This is, however, not possible when using automated fitting techniques as LCModel since they calculate the metabolite's overall signal. Moreover, the literature often gives only the values of relaxation times of the main resonances of individual metabolites.

As apparent from the estimated values of *T2'* and *T1'* the 10% change in the calculated concentrations corresponds for *TE* =136 ms and *TR* =1500 ms to rather big changes in *T2* and *T1*. However, a wide range of *T2* and *T1* values measured in the identical areas of the healthy brain can be found in the literature (46) and the relaxation times measured in patients are not usually available. Moreover, the estimated values of relaxation times depend on the localization method used, voxel size, range of *TE* and *TR* values, etc. (92). In this respect the published values of relaxation times are not comparable. Therefore, *T1* and *T2* relaxation times used for the corrections in healthy subjects and patients should be acquired with the equivalent methods. Ideally, the relaxation times should be estimated for each patient individually. However, using available measurement sequence this is not for time constrains possible. As a consequence, inaccurate knowledge of the *T1* and *T2* values limits achievable accuracy of the calculated absolute concentrations. Therefore, fast and reliable determination of *T1* and *T2* relaxation times suitable for examination of patients remains a challenge for further studies.

4.4 3D mapping of the radio frequency field *in vivo* (Paper I)

An Inhomogeneous radio frequency magnetic field (RF), is an essential source of error for the quantification of MRI and MR spectroscopy parameters. The inhomogeneous RF distribution results in variations in the signal strength and a spatially variable image contrast. Apart from the imperfect homogeneity of RF in the unloaded transmitting coil caused by the coil construction, the interactions between the tissue and magnetic fields, such as RF eddy and displacement currents, make the RF distribution dependent on the coil loading and on sample geometry (63,64). The manifestation of a dielectric resonance is strongly pronounced at higher field strengths, resulting in a large RF variation in the sample (65). Knowledge of the RF distribution in the sample helps to identify possible artifacts and enables the correction of RF related signal variations. Due to the interactions between the tissue and magnetic fields the measurement of the RF distribution directly in the subject is necessary. Several approaches for 2D mapping the RF distribution in the subject have been proposed (93-100). In order to correct for effects of RF inhomogeneities in 3D datasets knowledge of the 3D RF distribution in the sample is necessary. Only recently, the echo planar imaging (EPI) readout has been used in the magnetization prepared gradient echo sequence to acquire 3D RF maps (101), where the acquisition of the 3D RF map required four minutes.

In this study a 3D modification of the method introduced by Akoka et al. (96) based on the simultaneous acquisition of the spin echo and stimulated echo is proposed. The method enables the acquisition of the 3D RF map in 1.5 minute.

4.4.1 Methods

In the method proposed, a primary spin echo (SE) and a stimulated echo (STE) are measured in the three pulse sequence α - $TE/2$ - 2α - $TE/2$- data_acq - α - $TE/2$- data_acq. It can be shown (96) that using this sequence the flip angle α can be calculated as

$$\alpha = \arccos\left(\frac{I_{STE}\, e^{\frac{TM}{T1}}}{I_{SE}}\right) \qquad [4.8]$$

regardless of the nominal flip angle of the first pulse, where I_{SE} stands for the intensity of the spin echo and I_{STE} for the intensity of the stimulated echo measured in the described sequence. TM is the distance between the second and the third pulse.

The calculation of α values according to Eq. [4.8] requires knowledge of the $T1$ value of the measured tissue. However, $T1$ values are spatially variable in tissues. When the accurate $T1$ value in the given position in the sample is not known, the calculated flip angles are biased. In this study, one $T1$ value was used for the calculation of flip angles in all voxels in the measured volume and the dependence of the bias on the measurement parameters was estimated.

To make the 3D acquisition possible in a short time, two EPI readouts, one for the spin echo and one for the stimulated echo were implemented in the measurement sequence. The acquisition of the 3D RF map using 64 partitions and TR=500 ms requires 1.5 min. The method was demonstrated by measurements in both a phantom and a healthy volunteer at 3T.

4.4.2 Results

SE and STE images acquired *in vivo* as well as calculated RF maps showed good quality and no significant artifacts. The RF maps corresponding to four partitions acquired in a human brain are shown in Fig. 4.12. In the measured brain volume, flip angle values ranging from 76° to 113° were observed. The comparison of calculated flip angles with the flip angles obtained by fitting signal behaviour in the 3D STEAM-EPI sequence and the analysis of errors due to spatially dependent $T1$ values in the brain show that the accuracy of the calculated flip angles in the human brain using the proposed method is about 2°.

4.4.3 Conclusions

A method for fast 3D RF mapping was proposed. The results suggest that the calculation of 3D RF maps with sufficient quality and accuracy is possible. The use of EPI readouts makes the sequence more sensitive to inhomogeneities in the static magnetic field. Therefore, the proposed sequence is dedicated mainly to RF mapping in the head. The flip angle variations observed *in vivo* may significantly influence the signal in various measurement sequences and should be taken into account when interpreting results. One of the possible applications of the proposed 3D RF mapping technique is the correction of signal variations related to RF inhomogeneity in spectroscopic imaging at high fields.

A detailed description of this study is given in Appendix – Paper I.

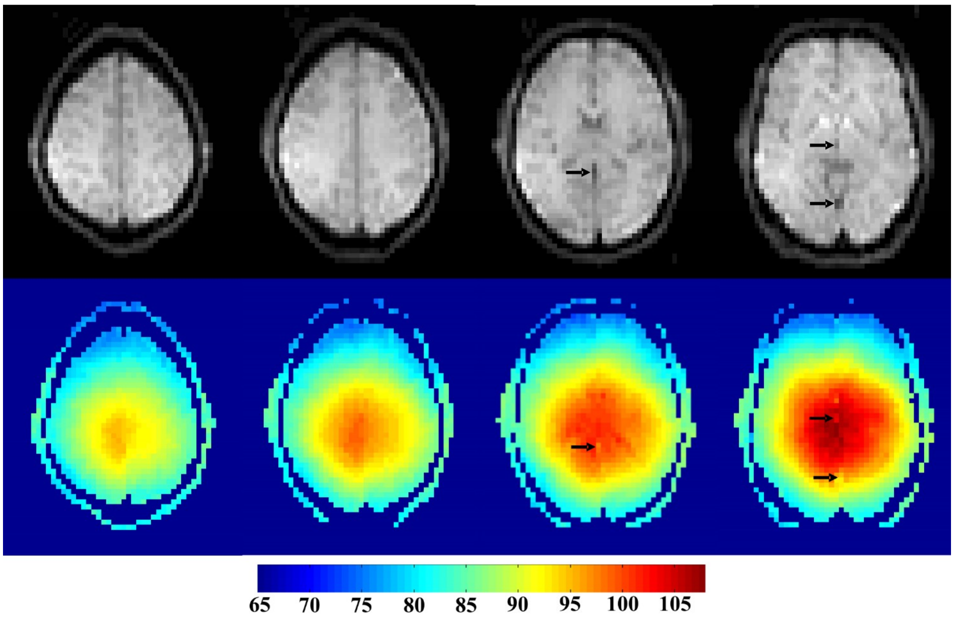

Fig. 4.12 SE images (upper row) and corresponding calculated RF maps (lower row) of four selected partitions of the 3D RF map acquired in the human brain. The flip angle values are expressed in colors, as indicated by the adjoined colorbar. Black arrows indicate areas with biased calculated flip angle values due to the high *CSF* percentage in the voxels.

4.5 Estimation of the *VOI* profile in an inhomogeneous RF field

As described in section 3.9.7, the major disadvantage of the measurement of the excitation profile of *VOI* of PRESS or STEAM sequences using a homogeneous phantom is the generally different RF distribution in the subject and in the phantom. The significant variations in the RF distribution in the sample can be present at high fields as demonstrated in Fig. 4.12. The calculation of the *VOI* profile by the division of the *VOI* and reference images as described in Eq. [3.38] is based on the assumption that flip angle values in the reference image are within the *VOI* constant. However, whenever the RF in the subject is not homogeneous this assumption is violated and the division of the *VOI* and reference images according to the Eq. [3.38] does not provide the correct *VOI* profile. While at low fields (up to 1.5T), where only small RF variations exists, the uncorrected division of the *VOI* and reference images provides a good approximation of the *VOI* profile, in the high fields additional corrections for RF inhomogeneities have to be performed. In this section, the method of calculating the *VOI* profile in an inhomogeneous RF is presented.

4.5.1 Influence of RF inhomogeneity on the excitation profile

A general formula describing the signal S in the PRESS or STEAM sequence can be written as (40).

$$S(\mathbf{r}) = \lambda(\mathbf{r}) M_0(\mathbf{r}) R(\mathbf{r}) P(\alpha(\mathbf{r}), \beta(\mathbf{r}), \gamma(\mathbf{r})) \qquad [4.9]$$

where $\lambda(\mathbf{r})$ stands for the reception profile of the receiving coil, $M_0(\mathbf{r})$ stands for the magnetization density, $R(\mathbf{r})$ describes relaxation and saturation effects and $P(\alpha(\mathbf{r}),\beta(\mathbf{r}),\gamma(\mathbf{r}))$ the excitation profile of the *VOI*.

The dependence of the excitation profile $P(\alpha,\beta,\gamma)$ on the flip angles α β γ in STEAM and PRESS sequences has been described in the literature as (40)

$$P(\alpha,\beta,\gamma) = (\sin\alpha)(\sin\beta)(\sin\gamma) \qquad \text{for STEAM} \qquad [4.10a]$$

$$P(\alpha,\beta,\gamma) = (\sin\alpha)(\sin^2\frac{\beta}{2})(\sin^2\frac{\gamma}{2}) \qquad \text{for PRESS} \qquad [4.10b]$$

where α, β and γ are generally spatially dependent flip angles reflecting the frequency profiles of the radio-frequency pulses and the RF inhomogeneities.

To assess the influence of the RF inhomogeneities, the flip angles $\alpha(\mathbf{r})$, $\beta(\mathbf{r})$ and $\gamma(\mathbf{r})$ can be expressed as a product of $\alpha_{\mathrm{rf}}(\mathbf{r})$, $\beta_{\mathrm{rf}}(\mathbf{r})$ and $\gamma_{\mathrm{rf}}(\mathbf{r})$ describing flip angle distributions in an assumed homogeneous RF and the function $B^{inh}(\mathbf{r})$ describing the inhomogeneity of the RF

$$\alpha(\mathbf{r}) = \alpha_{rf}(\mathbf{r})B^{inh}(\mathbf{r}) \quad \text{and} \quad \text{analogously for } \beta(\mathbf{r}) \text{ and } \gamma(\mathbf{r}) \qquad [4.11]$$

where the function $B^{inh}(\mathbf{r})$ equals 1 in the areas where the flip angle has the correct nominal value and is scaled correspondingly where any RF field inhomogeneity exists.

Let us assume the acquisition of 3D *VOI* and reference images using the STEAM imaging sequence. The division of the corresponding partitions of 3D *VOI* and reference images and ignoring the relaxation effects yields

$$D(\mathbf{r}) = \frac{S^{VOI}(\mathbf{r})}{S^{ref}(\mathbf{r})} = \frac{\sin(\alpha_{\mathrm{rf}}^{\mathrm{VOI}}(x)B^{inh}(\mathbf{r}))\cdot\sin(\beta_{\mathrm{rf}}^{\mathrm{VOI}}(y)B^{inh}(\mathbf{r}))\cdot\sin(\gamma_{\mathrm{rf}}^{\mathrm{VOI}}(z)B^{inh}(\mathbf{r}))}{\sin(\alpha_{\mathrm{rf}}^{\mathrm{ref}}(x)B^{inh}(\mathbf{r}))\cdot\sin(\beta_{\mathrm{rf}}^{\mathrm{ref}}(y)B^{inh}(\mathbf{r}))\cdot\sin(\gamma_{\mathrm{rf}}^{\mathrm{ref}}(z)B^{inh}(\mathbf{r}))} \qquad [4.12]$$

where a STEAM pre-selection accomplished by flip angles α, β and γ applied with gradients along three orthogonal directions **x**, **y** and **z** is assumed. The acquisition of the reference image is performed using the sequence with non-selective second and third pulses and with slab thickness much greater than the slice thickness of the *VOI*. Therefore, it can be assumed that in the area of the *VOI*, the flip angles $\alpha_{\mathrm{rf}}^{\mathrm{ref}}(x)$, $\beta_{\mathrm{rf}}^{\mathrm{ref}}(y)$ and $\gamma_{\mathrm{rf}}^{\mathrm{ref}}(z)$ in the reference image equal the nominal flip angle value 90°. Eq. [4.12] can then be rewritten

$$D(\mathbf{r}) = \frac{\sin(\alpha_{\mathrm{rf}}^{\mathrm{VOI}}(x)B^{inh}(\mathbf{r}))\cdot\sin(\beta_{\mathrm{rf}}^{\mathrm{VOI}}(y)B^{inh}(\mathbf{r}))\cdot\sin(\gamma_{\mathrm{rf}}^{\mathrm{VOI}}(z)B^{inh}(\mathbf{r}))}{\sin^3(\pi/2\cdot B^{inh}(\mathbf{r}))} \qquad [4.13]$$

From Eq. [4.13] it follows that due to additional signal variances induced by the function $B^{inh}(\mathbf{r})$, the reference image is not a proper signal reference with spatially invariant excitation. The influence of RF inhomogeneities can be eliminated by the multiplication of $D(\mathbf{r})$ with the denominator of Eq. [4.13] (102)

$$D^{cor}(\mathbf{r}) = D(\mathbf{r}) \cdot \sin^3(\pi/2 \cdot B^{inh}(\mathbf{r})) \qquad [4.14]$$

and the analogical solution for the PRESS sequence equals

$$D^{cor}(\mathbf{r}) = D(\mathbf{r}) \cdot \sin^5(\pi/2 \cdot B^{inh}(\mathbf{r})) \qquad [4.15]$$

To calculate the final correction factor for the given voxel in the 3D SI data, all partitions of the high resolution 3D data set $D^{cor}(\mathbf{r})$ matching the corresponding partition of the 3D SI data are averaged. This yields a data set with as many partitions as in the 3D SI data but with a high resolution matrix in each partition. The resulting value of the correction factor $D^{cor}(l,m,n)$ for the l-th, m-th , n-th voxels is obtained by averaging all high resolution voxels corresponding to the given voxel in the 3D SI data. The determination of the correction factor $D^{cor}(l,m)$ for 2D SI is analogous with the difference that all partitions of $D^{cor}(\mathbf{r})$ rather than partitions matching the slice thickness should be averaged, since the *VOI* profile in the slice direction always exceeds the slice thickness.

In the case of 2D *VOI* and reference images the division of the *VOI* and reference images yields (for STEAM)

$$D(\mathbf{r}) = \frac{S^{VOI}(\mathbf{r})}{S^{ref}(\mathbf{r})} = \frac{\int_z \sin(\alpha_{\mathrm{rf}}^{\mathrm{VOI}}(x)B^{inh}(\mathbf{r})) \cdot \sin(\beta_{\mathrm{rf}}^{\mathrm{VOI}}(y)B^{inh}(\mathbf{r})) \cdot \sin(\gamma_{\mathrm{rf}}^{\mathrm{VOI}}(z)B^{inh}(\mathbf{r}))dz}{\int_z \sin^2(\pi/2 \cdot B^{inh}(\mathbf{r})) \cdot \sin(\gamma_{\mathrm{rf}}^{\mathrm{VOI}}(z)B^{inh}(\mathbf{r}))dz} \qquad [4.16]$$

From Eq. [4.16] it follows that the described correction for RF inhomogeneities using 2D VOI and reference images is without additional measurements enabling to determine function $\gamma_{\mathrm{rf}}^{\mathrm{ref}}(z)$ impossible. Moreover, 3D RF mapping procedure to estimate function $\mathrm{B}^{\mathrm{inh}}(\mathbf{r})$ is always required. For the correction of the excitation profile in 3D CSI data sets the correction procedure using 3D VOI and reference images is the only method of choice. The proposed correction for an inhomogeneous RF can be adopted for various imaging sequences.

4.5.2 Influence of the signal saturation

In the division of the *VOI* and reference images in Eq. [4.12], the influence of the terms R^{VOI} and R^{ref} describing the signal saturation due to the finite *TR* was ignored. Since the *T1* values of water are spatially dependent, the signal saturation during the measurement of the *VOI* and reference images will not be equivalent to the saturation of the metabolites during SI measurements. This effect especially plays a role when *TR*s comparable to *T1* or shorter are used. The most affected are the areas with low flip angles close to the edges the *VOI* (62 nad) and areas with high *CSF* percentage. Therefore, bias in the estimated excitation profile can be assumed. On the other hand, it should be noted that since *T1* times of individual metabolites observable by ^{1}H SI in the brain are not identical one excitation profile of the *VOI* cannot, in principle, provide exact correction for all metabolites. A possible solution is the acquisition of the *VOI* and reference images under fully relaxed conditions, (*TR*>>*T1*), yielding after the division, the excitation profile of the *VOI* without any saturation and the calculation of the saturation factor analytically. However, although the analytical solution can be derived, the spatial dependence of individual flip angles $\alpha_{\mathrm{rf}}^{\mathrm{VOI}}(\mathbf{r})$, $\beta_{\mathrm{rf}}^{\mathrm{VOI}}(\mathbf{r})$ and $\gamma_{\mathrm{rf}}^{\mathrm{VOI}}(\mathbf{r})$ are required for the calculation of the saturation factor R^{VOI}, which can be estimated only from additional measurements. A method for accurately accounting for saturation effects is subject to future study.

4.5.3 Influence of the reception profile of the coil

Apart from the excitation profile, the inhomogeneous reception profile of the coil, denoted in Eq. [4.9] by the symbol $\lambda(\mathbf{r})$, is an additional source of spatial inhomogeneities in the measured signal. As is apparent from the calculation of the correction factor $D(\mathbf{r})$ in Eq. [4.12], the function $\lambda(\mathbf{r})$ is cancelled out by the division of the *VOI* and reference images and its influence on the final correction factor $D^{cor}(\mathbf{r})$ is not accounted for. The influence of $\lambda(\mathbf{r})$ has to be, therefore, accounted for separately and the new correction f_{prof} for both reception and excitation profiles can be introduced as

$$f_{prof}(\mathbf{r}) = D^{cor}(\mathbf{r})\lambda(\mathbf{r}) \qquad [4.17]$$

To calculate the correction factor f_{prof} according to Eq. [4.17], the spatial dependence of $\lambda(\mathbf{r})$ has to be know. The principle of reciprocity for the transmit-receive coil relates the reception of the coil with its excitation profile. It states that the reception profile is equivalent to the magnetic field produced at the given position by the coil when unit current flows through the coil (48).

Therefore, the measurement of the RF distribution of the transmit-receive coil provides information about the reception profile of the coil and $\lambda(\mathbf{r})=B^{inh}(\mathbf{r})$.

However, it should be noted that the principle of reciprocity is only an approximation when the wave length of the radio-frequency field is comparable with the object size, as in the case of the higher field strengths (3T and higher). In the study by Seifert et al. (103), it was noted that the product of the excitation and reception profiles has to show the same symmetry as an imaged object. Therefore, when acquiring axial slices in the head, the reception profile is equal to the excitation profile mirrored around the central sagittal plane.

In modern MR scanners, to achieve homogeneous transmitting and to increase signal-to-noise ratio, a body coil is used for transmitting and a multi-channel head coil is used for reception. The excitation profile $B^{inh}(\mathbf{r})$ of the body coil then provides no information about the reception profile of the head coil. In this case, the reception profile of the head coil can be approximately calculated from the division of the image acquired using the body coil as a transmitter and the head coil as a receiver and using the body coil both as a transmitter and receiver.

4.5.4 Implementation of the measurement sequences

The proposed correction method requires the fast acquisition of 3D *VOI* and reference images. Since the same *TR* as in an SI experiment should be used in the *VOI* and reference images, conventional imaging sequences cannot be employed due to time constraints.

Therefore, imaging sequences with PRESS and STEAM volume pre-selection and with EPI-readouts were adopted (Fig 4.13). 3D encoding was accomplished by the conventional single shot 2D EPI acquisition and the application of an additional partition-encoding in the slice direction (104). The resulting acquisition time *TA* then equals $TA=TR\cdot PAR$, where *PAR* stands for the number of partitions in the 3D *VOI* (reference) image For the acquisition of reference images, the same sequence but with non–selective second and third pulses was adopted. The function $B^{inh}(\mathbf{r})$ was calculated as $B^{inh}(\mathbf{r})=\alpha(\mathbf{r})/90$ where α is the flip angle value measured using the 3D RF mapping sequence described in section 4.4.

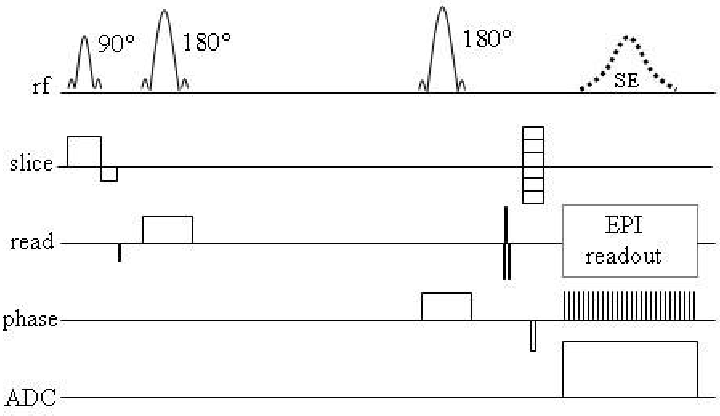

Fig. 4.13 The scheme of the sequence for the measurement of *VOI* images. A sequence without crusher gradients is shown for simplicity. The sequence for the measurement of reference images is identical, only the shaped second and third pulses are replaced by rectangular pulses applied without slice selective gradients.

4.5.5 Results and conclusions

The measurement sequences for the acquisition of 3D *VOI* and reference images using EPI readout proved to be robust and suitable for the acquisition of VOI and reference images in the human brain.

The importance of the proposed correction can be considered by calculating the correction factors for PRESS (according to Eq.[4.15]) and STEAM (according to Eq. [4.14]) using the RF distribution measured in the human brain by the proposed RF mapping sequence. In Fig. 4.14 the correction factors for a selected slice through basal ganglia are shown.

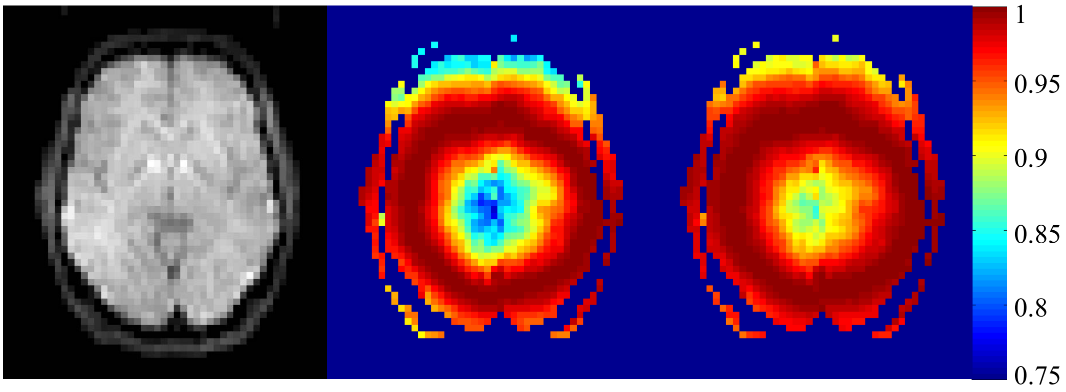

(a) (b) (c)

Fig. 4.14 Values of correction factors for the selected partition in the brain. The reference image (a), the correction factor for PRESS calculated according to Eq. [4.15] (b) and the correction factor for STEAM calculated according to Eq. [4.14] (c).

The measurements were performed at 3T. From Fig. 4.14 it is apparent that PRESS is more prone to RF inhomogeneities than STEAM. The correction is more important in the areas close to the middle of the brain. The lowest values of the correction factors calculated in the examined volume were about 0.62 for PRESS and 0.75 for STEAM. As a consequence, when the uncorrected profile is used for the correction the signal changes in the metabolites' signals resulting solely from RF inhomogeneities can be misinterpreted as a pathologic process or, conversely, the pathologic changes may be overlooked. Therefore, the proposed correction is recommended when measuring SI data at high fields.

4.6 Assessment of the quality of spectroscopic images (Paper II)

The results of an SI experiment are often presented as metabolic images showing the distribution of particular metabolites. The calculation of these images is usually performed automatically based on the processing of the spectra of interest. If the spectra quality is not sufficient, the calculated concentrations are biased and the resulting metabolic images show an incorrect metabolite distribution. Although a visual inspection of all spectra reveals the low quality spectra, it is a time consuming procedure. Instead, the display of an 'error image' reflecting the reliability of the computed concentrations in the metabolite image has been proposed (105,106,76). The key question of the concept of error images is the selection of the parameter for the calculation of error images. In the developed program CULICH the program LCModel is used for the calculation of the concentrations of metabolites. The concentrations are in LCModel calculated along with corresponding Cramer-Rao lower bounds (*CRBs*) reflecting the accuracy of the calculated concentrations. Therefore, CRBs calculated by LCModel could be a suitable parameter for the calculation of error images in CULICH. However, *CRBs* represent accurately the accuracy of the calculated concentrations only if the correct model function for spectra fitting is used. Although the LCModel program uses a basis set acquired from in vitro measurements of metabolites, the presence of the background signal and noise in the spectra makes the fulfillment of the correct model function (and hence the validity of the estimated *CRBs*) ambiguous. The aim of this study was to test the relevance of *CRBs* estimated by LCModel to describe the errors of calculated concentrations of metabolites by means of spectra simulations and to propose a parameter for the calculation of error images for concentration ratios. To use the concept of error images effectively, an effective way to display the information from error images was developed.

4.6.1 Methods

For simulation purposes, two generic spectra mimicking spectra acquired at 1.5T with and without baseline signals were created. To simulate various experimental conditions, noise was added to the spectra and the spectra were line broadened so that 20 spectra with different signal-to-noise ratio (*SNR*) and line broadening (*LB*) combinations were obtained. 100 noise realizations were performed for each *SNR* value. All simulated spectra were processed by LCModel 6.0. For each set of 100 spectra with a given *SNR* and linewidth combination, the mean of the estimated concentrations (*M*), the percentage standard deviation of all the estimated concentrations from the mean (*STD*) and the mean of percentage *CRBs* (*CRB_avg*) were computed for all metabolites in the spectrum as well as the selected metabolite ratios. If *CRBs* describe the accuracy of the calculated concentrations *CRB_avg* should be related to corresponding *STD* values. To assess the relation between *CRBs* and standard deviations of the computed concentrations, *CRB_avg* values were plotted against *STD* values for all *SNR* and line broadening combinations (20 pairs all together) and linear regression and correlation analyses were performed. The calculation of error image was demonstrated on *in vivo* SI data.

4.6.2 Results

A high correlation (correlation coefficients ranging from 0.97 to 0.99) was found between *CRB_avg* and *STD* values for all the evaluated metabolites and ratios indicating that *CRBs* estimated by LCModel can be used to describe the variance of the calculated concentrations. The concept of error images is demonstrated on the metabolite image of Creatine. In Fig. 4.15 a semi-transparent metabolic image of creatine, measured from an oblique slice intersecting the basal ganglia, is overlaid on a morphologic image. The metabolite image shows an increased concentration of Creatine (Cr) in the basal ganglia, which is in accordance with the published data (107,108). On the other hand, the image shows very low Cr concentrations in the middle frontal region. The spectra from selected regions in the metabolite image are shown in Fig. 4.15. As apparent from that figure, low Cr concentrations in the middle frontal region are the consequence of poor quality spectra. However, this finding can be directly obtained using the error image without viewing the spectra. In Fig. 4.16a, the error image reflecting the *CRB* values of Cr is displayed. It immediately indicates low accuracy of the concentrations calculated in the middle frontal region. To visualize only those parts of the metabolite image with low *CRBs*, a threshold of 8% was set for *CRBs* and only those areas of the metabolic image with *CRBs* values below the threshold are displayed in Fig. 4.16b. However, a question arises which value is the proper threshold value. To overcome the ambiguity of the threshold value, we propose to map *CRBs* as the transparency of the metabolite image (Fig, 4.16c). After the transparency mapping, the middle frontal part of the image remained completely transparent as a consequence of the very high *CRB* values. The observed decrease in Cr concentrations in the frontal part of the metabolite image can be therefore identified as the result of poor quality spectra and can be discarded from the analysis.

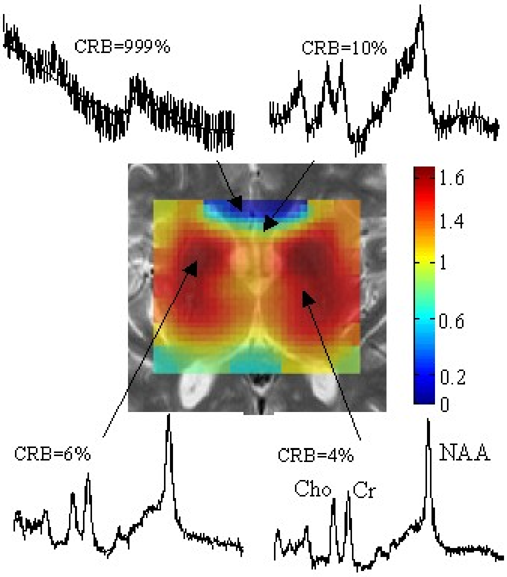

Fig. 4.15 Metabolite image of creatine measured from a slice containing the basal ganglia. Concentrations are expressed as colors of the metabolite image as indicated by the colorbar. The spectra measured from the areas indicated by the arrows along with the corresponding *CRBs* of creatine are shown

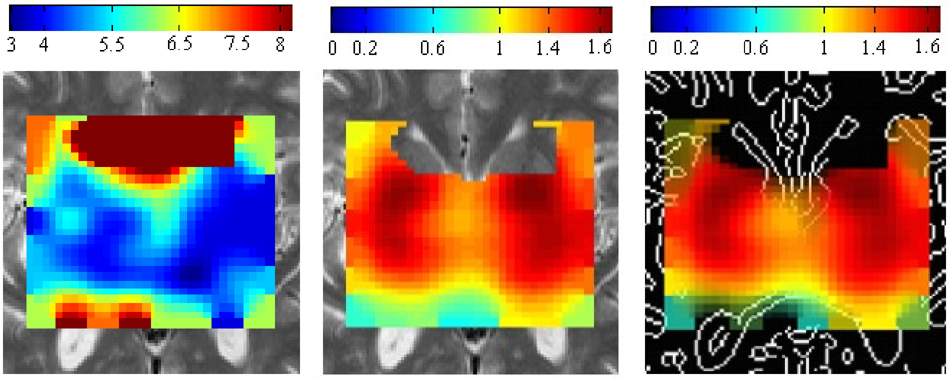

(a) (b) (c)

Fig. 4.16 Error image corresponding to the creatine metabolite image shown in Fig. 4.17(a). Metabolite image of creatine where only the areas with corresponding *CRBs* below 8% are shown (b). Metabolite image of creatine where *CRB* values are mapped as a transparency of the image (c). High transparency reflects high *CRB* values and hence low accuracy of metabolite image.

4.6.3 Conclusions

It was shown that *CRBs* are strongly correlated with the standard deviations of the calculated concentrations and therefore reflect the relative uncertainty of the calculated concentrations among voxels in the spectroscopic grid, which makes *CRBs* a suitable parameter for the calculation of error images in SI. This approach avoids extensive examination of each spectrum of large SI data sets and helps to reject low quality spectra.
A detailed description of this study is given in Appendix – Paper II.

4.7 ^{1}H MR spectroscopic imaging in patients with MRI-negative extratemporal epilepsy (Paper III)

In epileptology, ^{1}H MRS has proved to have a significant value in the lateralization of the epileptogenic zone in mesiotemporal epilepsy (109-114). In extratemporal epilepsies, the epileptogenic zone is frequently larger and more difficult to delineate in comparison with temporal lobe epilepsy. In patients with MRI-detectable lesions, ^{1}H MRS abnormalities usually co-localize with those areas of lesions found using MRI. The most challenging patients are those with normal MRI findings, in whom only ^{1}H MRS holds a promise for finding the metabolic changes corresponding to the epileptogenic zone. Few reports have referred to ^{1}H MRS abnormalities in patients with frontal or parietal lobe epilepsy, with or without MRI detected lesions (115-117). According to these studies, it seems probable that ^{1}H MRS may help in the lateralization of extratemporal epilepsy; however, it is not clear whether it is useful in the localization of the epileptogenic zone. It also remains unclear if ^{1}H MRS abnormalities reflect a pathology underlying seizure onsets or non-specific neuronal disturbances spreading to surrounding and distant non-epileptic regions. In the current study the hypothesis was tested that ^{1}H MRS could help in the localization of the epileptogenic zone.

4.7.1 Methods

Seven patients (three females and four males aged from eight to 23 years, mean age, 11.7 years), with the diagnosis of refractory extratemporal epilepsy and at least two negative MRI examinations were included in the study. The patients were examined according to the diagnostic presurgical protocol for patients with refractory MRI-negative focal epilepsy. The protocol included video-EEG monitoring, ^{1}H MRS, ictal ^{99m}Tc-ECD SPECT with subtraction and interictal ^{18}FDG-PET, etc. SI examinations were performed using a 1.5-T whole body MR imager. SI spectra were measured in the transversal plane by using a volume pre-selected PRESS-SI. The data were processed by the program CULICH (72). The description of metabolic abnormalities was done in two steps. First, metabolic images were evaluated visually and the position of the lesion was proposed on the basis of minima in the metabolic maps. In the second step, the coefficient of asymmetry (C_a) was calculated. C_a is defined as

$$C_a = 2*({}^{x}R_{sin} - {}^{x}Rd_x)/({}^{x}R_{sin} + {}^{x}R_{dx}) \qquad [4.17]$$

where ^{x} is the metabolite under investigation (NAA, Cr or Cho) and R is the metabolite concentration ratio in the left (*sin*) and right (*dx*) hemispheres (symmetrical with respect to the central line). The minimum number of SI voxels used for statistical evaluation was five for the side of the suspected lesion, and the data were compared with the coefficients of asymmetry obtained from the control group by ANOVA analysis with contrast evaluation and by paired t-tests. The results of the SI examination were compared with the results from ictal SPECT, subdural mapping and the position of the resection. Histopathology of the resected brain tissue has been performed.

4.7.2 Results

All patients had a visible asymmetry in images of metabolite concentrations (or their ratios). The most frequent abnormalities were characterized by significant differences in the coefficients of asymmetry of the NAA/Cr (in five of seven patients) and NAA/Cho (in four of seven patients) ratios. In five patients, there was localized a local minima of NAA/Cr and NAA/Cr ratios. In two remaining patients only the asymmetry between the left and right hemisphere was observed.

Comparison of metabolite maps with results of subdural electrode mapping showed that in patients with a clearly localized metabolic abnormality, the ictal onset zone overlapped with ^{1}H MRS changes. In the remaining two patients without a localized ^{1}H MRS abnormality the ictal onset zone was found outside the position of SI slides. However, the lateralization resulting from SI evaluation was confirmed by the results of the surgery, supporting the assumption that metabolite changes are not concentrated only at a restricted area but are usually more extensive

In the patients with a localized ^{1}H MRS abnormality, metabolite changes co-localized with results of ictal SPECT in all (four) cases with a localized hyperperfusion zone.

Histopathological analysis showed FCD in all patients. Severe type II FCD were predominantly encountered. Correlation of ^{1}H MRS abnormalities with the localization of the resection cavity on postoperative MRI showed an overlap of these regions in all the patients with a localized ^{1}H MRS pathology.

Based on the precise correlation of postoperative MRI defects with ^{1}H MRS maps, we can be certain that the histologically examined tissue co-localized with the regions of the most prominent ^{1}H MRS changes. The correlation between the localized ^{1}H MRS abnormality and the lesion in T2w image after surgery is for one patient shown in Fig. 4.17.

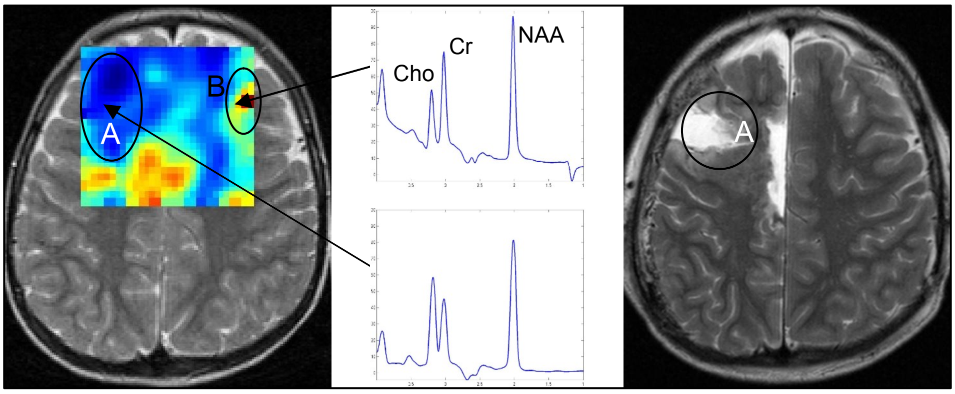

Fig. 4.17 SI result and T2w image of one patient (NAA – N-acetylaspartate, Cho – choline compounds, Cr – creatine/phosphocreatine).
a) Projection of the NAA/Cho CSI map before surgery: a large hypointensive area A (blue color) was considered to be a metabolic anomaly, and C_a calculated from areas A and B confirmed this;
b) ^{1}H MR spectra from symmetrical voxels in areas A and B (see arrows) show differences in the NAA/Cho ratio between area A and area B: A/B ~ 4.6/7.6;
c) Hyperintensive lesion in T2w image after surgery corresponds to area A in SI image.

4.7.3 Conclusions

The present study found promising results concerning the sensitivity of ^{1}H MRS in patients with MRI-undetectable malformations of cortical development. In our group of patients, ^{1}H MRS helped not only to lateralize, but also to localize the epileptogenic zone and therefore showed practical value for designing a surgical approach. The most important message of the study is the good correlation among ^{1}H MRS, ictal SPECT and subdural mapping, which was subsequently confirmed by histopathological analysis of the resected tissue. We suggest that ^{1}H MRS may provide important additional data in the presurgical evaluation of patients without apparent MRI lesions.

A detailed description of this study is given in Appendix – Paper III.

5 Conclusion

In the presented thesis several aspects of the SI data evaluation have been addressed.
The CULICH program has been developed to enable the comprehensive processing of SI data. The program offers advanced functionality for evaluation of SI data. The initial experience with the program shows that CULICH is suitable for evaluation of SI data measured in both clinical practice and experiments. The program has been implemented in two places of work where it is currently undergoing thorough testing. The inclusion of additional features for advanced statistical evaluation of data is planned for a future version of CULICH.

The direct comparison of results obtained by SI and SVS techniques showed that in the experimental setup used there were no significant differences in concentrations calculated using both methods. Although principal issues, such as the existence of point spread function, make quantitative SI less reliable, the results suggests that quantification of spectra using the SI technique is possible. However, it should be noted that all relevant corrections have to be applied to SI data to obtain correct concentration values. The omission of corrections in the comparison presented was justified by ensuring the same conditions for both SVS and SI measurements.

Several effects may influence the measured signal. Often their impact on the result is ignored, leading to systematic errors in the measured data. Concerning signal corrections, the thesis focused on the influence of relaxation times on the calculation of absolute concentrations of metabolites and the determination of the excitation profile of VOI in the inhomogeneous RF. In contrast to the influence of *T2* time, which can be diminished by using short echo times, time constraints in SI do not allow the use of long *TR* to avoid signal saturation. Therefore, the finite error corresponding to inaccurate knowledge of *T1* time remains one of the limiting factors of the accuracy of calculated concentrations in SI. In this respect, methods allowing the fast measurement of *T1* times of metabolites are of high interest. The sequence for 3D mapping of RF was proposed and its use for the determination of the *VOI* profile in inhomogeneous RF was demonstrated. It was shown that inhomogeneous RF may play a significant role in determination of the excitation profiles. The exact inclusion of the saturation effects in the calculated *VOI* profile is subject to current research. 3D RF mapping sequence may also find use in determining corrections for RF inhomogeneity related signal variations in structural and functional MR imaging.

The assessment of the quality of spectroscopic images is of high importance in clinical practice. Although visual inspection of all spectra is preferred, this is not possible in the clinical environment. Error images allow focusing on the areas with higher error where lower quality spectra can be expected. Moreover, the innovative approach of the selective display of metabolite images depending on the error of the calculated concentrations significantly simplifies the data analysis. A metabolite image with low accuracy has no clinical value and can be excluded from analysis. Error analysis using the concept of error images was implemented in CULICH and became an integral part of SI data evaluation in our department.

CULICH has been applied to the evaluation of SI data measured in patients with MRI-negative extratemporal epilepsy. The localization of the epilepsy lesion according to SI findings and histology of the resected tissue are highly correlated. This result suggests that the SI technique can be helpful for localizing epileptogenic lesions in patients with negative findings from other diagnostic modalities.

It can be concluded that the developed methodology will contribute to the more accurate evaluation of SI data, which improves the reliability of clinical examinations using SI techniques.

6 Publications

6.1. Publications and manuscripts the thesis is based on

Jiru F, Skoch A, Klose U, Grodd W, Hajek M. Error images for spectroscopic imaging by LCModel using Cramer-Rao bounds. *MAGMA*. 2006 Feb;19(1):1-14.

Jiru F, Klose U. Fast 3D radio frequency field mapping using echo planar imaging. Submitted to *Magn. Reson. Med.*

Krsek P, Hajek M, Dezortova M**, Jiru F,** Skoch A, Marusic P, Zamecnik J, Kyncl M, Tichy M, Komarek V. ^{1}H MR spectroscopic imaging in patients with MRI-negative extratemporal epilepsy: Correlation with ictal onset zone and histopathology. *Manuscript.*

Jiru F, Dezortova M, Burian M, Hajek M. The role of relaxation time corrections for the evaluation of long and short echo time 1H MR spectra of the hippocampus by NUMARIS and LCModel techniques. *MAGMA*. 2003 Nov;16(3):135-43.

6.2. Other publications concerning the thesis

Klose U., **Jiru F**.: Principles of MR Spectroscopy and Chemical Shift Imaging. In: Advanced Image Processing in Magnetic Resonance Imaging. Edited by Luigi Landini. CRC Press, 2005. Book chapter, pp.369-409.

6.3. Other publications

Hajek M, Adamovicova M, Herynek V, Skoch A, **Jiru F**, Krepelova A, Dezortova M. MR relaxometry and 1H MR spectroscopy for the determination of iron and metabolite concentrations in PKAN patients. *Eur Radiol*. 2005 May;15(5):1060-8.

Skoch A, **Jiru F**, Dezortova M, Krusinova E, Kratochvilova S, Pelikanova T, Grodd W, Hajek M. Intramyocellular lipid quantification from (1)H long echo time spectra at 1.5 and 3 T by means of the LCModel technique. *J Magn Reson Imaging*. 2006 Mar 27; [Epub ahead of print].

References

1 Klose U, Jiru F. Principles of MR Spectroscopy and Chemical Shift Imaging. In: Advanced Image Processing in Magnetic Resonance Imaging. Edited by Luigi Landini. CRC Press, 2005

2 Brown T, Kincaid B, Ugurbil K. NMR chemical shift imaging in three dimensions. *Proc Natl Acad Sci U S A.* 1982; 9:3523 - 3526.

3 Maudsley AA, Hilal SK, Perman WP, Simon. Spatially resolved high resolution spectroscopy by four dimensional NMR. *J. Magn. Reson.* 1983; 51:147-152.

4 Pohmann R, von Kienlin M, Haase A. Theoretical evaluation and comparison of fast chemical shift imaging methods. *J Magn Reson*. 1997; 129:145-160.

5 Duyn JH, Moonen CT. Fast proton spectroscopic imaging of human brain using multiple spin-echoes. *Magn Reson Med*. 1993; 30:409-414.

6 Duyn JH, Frank JA, Moonen CT. Incorporation of lactate measurement in multi-spin-echo proton spectroscopic imaging. *Magn Reson Med*. 1995; 33:101-107.

7 Adalsteinsson E, Irarrazabal P, Spielman DM, Macovski A. Three-dimensional spectroscopic imaging with time-varying gradients. *Magn Reson Med*. 1995; 33:461-466.

8 Posse S, DeCarli C, Le Bihan D. Three-dimensional echo-planar MR spectroscopic imaging at short echo times in the human brain. *Radiology*. 1994; 192:733-738.

9 Mansfield P. Spatial mapping of the chemical shift in NMR. *Magn Reson Med*. 1984; 1:370-386.

10 Norris DG and Dreher W. Fast proton spectroscopic imaging using the sliced k-space method. *Magn Reson Med*. 1993; 30:641-645.

11 Matsui S, Sekihara K, Kohno H. Spatially resolved NMR spectroscopy using phase-modlulated spin-echo trains. *J.Magn. Reson.* 1986; 67:476-490.

12 Web P, Spielman D, Macovski A. A fast spectroscopic imaging method using a blipped phase encode gradient. *Magn Reson Med*. 1989; 12:306-315.

13 Speck O, Scheffler K, Hennig J. Fast 31P chemical shift imaging using SSFP methods. *Magn Reson Med*. 2002; 48:633-639.

14 Dreher W, Geppert C, Althaus M, Leibfritz D. Fast proton spectroscopic imaging using steady-state free precession methods. *Magn Reson Med*. 2003; 50:453-460.

15 Dydak U, Weiger M, Pruessmann KP, Meier D, Boesiger P. Sensitivity-encoded spectroscopic imaging. *Magn Reson Med*. 2001; 46:713-722.

16 Dydak U, Pruessmann KP, Weiger M, Tsao J, Meier D, Boesiger P. Parallel spectroscopic imaging with spin-echo trains. *Magn Reson Med*. 2003; 50:196-200.

17 Moonen CT, Sobering G, van Zijl PC, Gillen J, von Kienlin M, Bizzi A. Proton spectroscopic imaging of human brain. *J. Magn. Reson.* 1992; 98:556-575.

18 Duyn JH, Matson GB, Maudsley AA, Weiner MW. 3D phase encoding 1H spectroscopic imaging of human brain. *Magn Reson Imaging*. 1992; 10:315-319.

19 Spielman D, Pauly J, Macovski A, Enzmann D. Spectroscopic imaging with multidimensional pulses for excitation: SIMPLE. *Magn Reson Med*. 1991; 19:67-84.

20 Duyn JH, Gillen J, Sobering G, van Zijl PC, Moonen CT. Multisection proton MR spectroscopic imaging of the brain. *Radiology*. 1993; 188:277-282.

21 Posse S, Schuknecht B, Smith ME, van Zijl PC, Herschkowitz N, Moonen CT. Short echo time proton MR spectroscopic imaging. *J Comput Assist Tomogr*. 1993; 17:1-14.

22 Ebel A, Govindaraju V, Maudsley AA. Comparison of inversion recovery preparation schemes for lipid suppression in 1H MRSI of human brain. *Magn Reson Med*. 2003; 49:903-908.

23 Spielman D, Meyer C, Macovski A, Enzmann D. 1H spectroscopic imaging using a spectral-spatial excitation pulse. *Magn Reson Med.* 1991; 18:269-279.

24 Kiefer C and Klose U. Presaturation of irregular spatial structures with two dimensional waveforms corrected for B1-inhomogeneities. *Proceedings of the International Society for Magnetic Resonance in Medicine*. 2000; 8:1429.

25 Hu X, Patel M, Ugurbil K. A new strategy for spectroscopic imaging. *J. Magn. Reson. B*. 1994; 103:30-38.

26 Hu X, Patel M, Chen W, Ugurbil K. Reduction of truncation artifacts in chemical shift imaging by extended sampling using variable repetition time. *J. Magn. Reson. B*. 1995; 106:292-296.

27 Haupt CI, Schuff N, Weiner MW and Maudsley AA. Removal of lipid artifacts in 1H spectroscopic imaging by data extrapolation. *Magn Reson Med*. 1996; 35:678-687.

28 Bracewill, R. The Fourier Transform and it applications. *New York.* 1978

29 Murphy Boesch J, Jiang H, Stoyanova R, Brown TR. Quantification of phosphorus metabolites from chemical shift imaging spectra with corrections for point spread effects and B1 inhomogeneity. *Magn Reson Med*. 1998; 39:429-438.

30 Constantinides CD, Weiss RG, Lee R, Bolar D, Bottomley PA. Restoration of low resolution metabolic images with a priori anatomic information: 23Na MRI in myocardial infarction. *Magn Reson Imaging*. 2000; 18:461-471.

31 Gao Y, Reeves SJ. Optimal k-space sampling in MRSI for images with a limited region of support. *IEEE Trans Med Imaging*. 2000; 19:1168-1178.

32 Ernst RR, Bodenhausen G, Wokaun A. Principles of nuclear magnetic resonance in one and two dimensions. *Oxford,.* 1987.

33 Hugg JW, Maudsley AA, Weiner MW, Matson GB. Comparison of k-space sampling schemes for multidimensional MR spectroscopic imaging. *Magn Reson Med*. 1996; 36:469-473.

34 Mareci TH, Brooker HR. Essential considerations for spectral localization using indirect gradient encoding of spatial information. *J. Magn. Reson.* 1991; 92:229 - 246.

35 Kuhn B, Dreher W, Norris DG, Leibfritz D. Fast proton spectroscopic imaging employing k-space weighting achieved by variable repetition times. *Magn Reson Med*. 1996; 35:457-464.

36 Adalsteinsson E, Star Lack J, Meyer CH, Spielman DM. Reduced spatial side lobes in chemical-shift imaging. *Magn Reson Med*. 1999; 42:314-323.

37 Maudsley AA, Matson GB, Hugg JW, Weiner MW. Reduced phase encoding in spectroscopic imaging. *Magn Reson Med*. 1994; 31:645-651.

38 Ponder SL, Twieg DB. A novel sampling method for 31P spectroscopic imaging with improved sensitivity, resolution, and sidelobe suppression. *J Magn Reson B*. . 1994; 104:85-88.

39 Hetherington HP, Luney D J, Vaughan JT, Pan JW, Ponder SL, Tschende, O, Twieg DB, Pohost GM. 3D 31P spectroscopic imaging of the human heart at 4.1 T. *Magn Reson Med*. 1995; 33: 427-431.

40 Haacke EM, Brown RW, Thompson MR, Venkatesan R. *Magnetic Resonance Imaging, Physical Principles and Sequence Design.* John Wiley & Sons, New York., 1999.

41 Granot J. Selected Volume Spectroscopy (SVS) and Chemical-Shift Imaging. A Comparison. *J. Magn. Reson.* 1986; 66:197-200.

42 Posse S, Aue WP. 1H spectroscopic imaging at high spatial resolution. *NMR Biomed*. 1989; 2:234-239.

43 Maudsley AA. Sensitivity in Fourier imaging. J Magn Reson. 1986; 363-366.

44 Gruber S, Mlynarik V, Moser E.. High-resolution 3D proton spectroscopic imaging of the human brain at 3 T: SNR issues and application for anatomy-matched voxel sizes. *Magn Reson Med*. 2003; 49:299-306.

45 Kreis R. Quantitative localized 1H MR spectroscopy for clinical use. *Prog. NMR Spectroscopy*. 1997; 31:155-195

46 Hajek M. Quantitative NMR spectroscopy. Comments on methodology of in vivo MR spectroscopy in medicine. *Quart. Magn. Res. Biol. Med.* 1995; 3:165-193.

47 Keevil SF, Barbiroli B, Brooks JC et al. Absolute metabolite quantification by in vivo NMR spectroscopy: II. A multicentre trial of protocols for in vivo localised proton studies of human brain. Magn Reson Imaging. 1998 Nov;16(9):1093-106.

48 Hoult DI, Richards RE. The signal-to-noise ratio of the nuclear magnetic resonance experiment. *J Magn Reson* 1976; 24:71-85.

49 Michaelis T, Merboldt KD, Bruhn H, Hanicke W, Frahm J. Absolute concentrations of metabolites in the adult human brain in vivo: quantification of localized proton MR spectra. *Radiology*. 1993 Apr;187(1):219-27.

50 Helms G. A precise and user-independent quantification technique for regional comparison of single volume proton MR spectroscopy of the human brain. *NMR Biomed*. 2000 Nov;13(7):398-406.

51 Jost G, Harting I, Heiland S. Quantitative single-voxel spectroscopy: the reciprocity principle for receive-only head coils. *J Magn Reson Imaging*. 2005 Jan;21(1):66-71.

52 Ethofer T, Mader I, Seeger U, Helms G, Erb M, Grodd W, Ludolph A, Klose U. Comparison of longitudinal metabolite relaxation times in different regions of the human brain at 1.5 and 3 Tesla. *Magn Reson Med*. 2003 Dec;50(6):1296-301.

53 Traber F, Block W, Lamerichs R, Gieseke J, Schild HH. 1H metabolite relaxation times at 3.0 tesla: Measurements of T1 and T2 values in normal brain and determination of regional differences in transverse relaxation. *J Magn Reson Imaging*. 2004 May;19(5):537-45.

54 McLean MA, Woermann FG, Barker GJ, Duncan JS. Magn Reson Med. 1999 Jan;41(1):21-9. Quantitative analysis of short echo time (1)H-MRSI of cerebral gray and white matter. *Magn Reson Med*. 2000 Sep;44(3):401-11.

55 Noworolski SM, Nelson SJ, Henry RG, Day MR, Wald LL, Star-Lack J, Vigneron DB. High spatial resolution 1H-MRSI and segmented MRI of cortical gray matter and subcortical white matter in three regions of the human brain. *Magn Reson Med*. 1999 Jan;41(1):21-9.

56 Hetherington HP, Mason GF, Pan JW, Ponder SL, Vaughan JT, Twieg DB, Pohost GM. Evaluation of cerebral gray and white matter metabolite differences by spectroscopic imaging at 4.1T. *Magn Reson Med*. 1994 Nov;32(5):565-71.

57 Pouwels PJ, Frahm J. Regional metabolite concentrations in human brain as determined by quantitative localized proton MRS. *Magn Reson Med*. 1998 Jan;39(1):53-60.

58 Weber-Fahr W, Ende G, Braus DF, Bachert P, Soher BJ, Henn FA, Buchel C. A fully automated method for tissue segmentation and CSF-correction of proton MRSI metabolites corroborates abnormal hippocampal NAA in schizophrenia. *Neuroimage*. 2002 May;16(1):49-60

59 Hong Yan. Signal Processing for Magnetic Resonance Imaging and Spectroscopy (Signal Processing and Communications Series, 15) Marcel Dekker, New York 2002.

60 Horska A, Calhoun VD, Bradshaw DH, Barker PB. Rapid method for correction of CSF partial volume in quantitative proton MR spectroscopic imaging. *Magn Reson Med*. 2002 Sep;48(3):555-8.

61 Bonekamp D, Horska A, Jacobs MA, Arslanoglu A, Barker PB. Fast method for brain image segmentation: application to proton magnetic resonance spectroscopic imaging. *Magn Reson Med*. 2005 Nov;54(5):1268-72.

62 Wild JM, Marshall I. Normalisation of metabolite images in 1H NMR spectroscopic imaging. *Magn Reson Imaging*. 1997; 15(9):1057-66.

63 Botomley PA, Andrew ER. RF magnetic field penetration, phase shift and power dissipation in biological tissue: implication for NMR imaging. *Phys Med Bio*l 1978; 23:630-643.

64 Hoult DI, Phil D. Sensitivity and power deposition in a high-field imaging experiment. *J Magn Reson Imaging* 2000; 12(1):46-67.

65 Yang QX, Wang J, Zhang X, Collins CM, Smith MB, Liu H, Zhu XH, Vaughan JT, Ugurbil K, Chen W. Analysis of wave behavior in lossy dielectric samples at high field. *Magn Reson Med* 2002; 47(5):982-9.

66 Hajek M, Burian M, Dezortova M. Application of LCModel for quality control and quantitative in vivo 1H MR spectroscopy by short echo time STEAM sequence. *MAGMA*. 2000 Feb;10(1):6-17.

67 Jung WI. Localized Double spin echo proton spectroscopy Part I: Basic concepts. Concepts in Magn. Reson. 1996; 8(1):1-15.

68 McKinnon G., Boesinger P. Lactate signal loss with echo based volume selective spectroscopy. *Magn. Reson Med. Biol.* 1990; IV:101-111.

69 Bunse M, Jung W. I., Lutz O. Localized double spin-echo spectroscopy of weakly homonuclear coupled spin systems: Influence of chemical shift artifacts. *Appl. Magn. Reson.* 1992; 3:185-197

70 Vanhamme L, Sundin T, Hecke PV, Huffel SV. MR spectroscopy quantitation: a review of time-domain methods. *NMR Biomed.* 2001 Jun;14(4):233-46.

71 Mierisova S, Ala-Korpela M. MR spectroscopy quantitation: a review of frequency domain methods. *NMR Biomed.* 2001 Jun;14(4):247-59.

72 Jiru F, Burian M, Skoch A, Hajek M (2002) LCModel for spectroscopic imaging. In: Proceedings of the Annual Science Meeting ESMRMB, *MAGMA* Suppl 1, Cannes, p 368

73 Provencher SW. Estimation of metabolite concentrations from localized in vivo proton NMR spectra. *Magn Reson Med.* 1993 Dec;30(6):672-9.

74 Kanowski M, Kaufmann J, Braun J, Bernarding J, Tempelmann C. Quantitation of simulated short echo time 1H human brain spectra by LCModel and AMARES. Magn Reson Med. 2004 May;51(5):904-12.

75 Provencher SW. A constrained regularization method for inverting data represented by linear algebraic or integral equations. *Comput Phys Commun* 1982; 27:213–227.

76 Jiru F, Skoch A, Klose U, Grodd W, Hajek M. Spectroscopic imaging of Glutamine and Glutamate usány LCModel and error images. In: Proceedings of the 21th Annual Science Meeting ESMRMB*,* 2004 *MAGMA* – Suppl, Copenhagen, Denmark

77 Mareci TH, Brooker HR. Essential Considerations for Spectral Localization Using Indirect Gradient Encoding of Spatial Information. *J Magn Reson.* 1991; 92:229-246

78 Wang Z, Bolinger L, Subramanian VH, Leigh JS. Errors of Fourier chemical shift imaging and their corrections. *J Magn Reson* 1991; 92:64-72

79 Koch T, Brix G, Lorentz WJ. Theoretical description, Measurement and Correction of Localization errors in 31P Chemical shift imaging. *J Magn Reson, Series B* 1994; 104:199-211

80 Moonen CT et at. Proton Spectroscopic Imaging of Human Brain. *J Magn Reson* 1992; 98:556-575

81 Husted CA, Duijn JH, Matson GB, Maudsley AA, Weiner MW. Molar Quantitation of in vivo Proton metabolites in human brain with 3D magnetic resonance spectroscopic imaging. *MRI* 1994; 12:661-667.

82 Alger R, Symko SC, Bizzi A, Poss S, DesPres DJ, Armstrong MR. Absolute quantitation of short TE brain 1h-MR spectra and spectroscopic imaging data. *J Comp Assist Tomogr* 1993; 17:191-199.

83 Lara RS, Matson GB, Hugg JW, Maudsley AA, Weiner MW. Quantitation of in vivo phosporus metabolites in human brain with magnetic resonance spectroscopic imaging (MRSI) *MRI* 1993; 11:237-278.

84 Soher BJ, van Zijl PC, Duyn H, Barker PB. Quantitative proton MR Spectroscopic imaging of the human Brain *Magn. Reson. Med.* 1996; 35:356-363.

85 Pan JW, Twieg DB, Heterington P. Quantitative Spectroscopic imaging of the human brain. *Magn. Reson. Med.* 1998; 40:363-369.

86 Mc Lean MA, Woermann FG, Simister RJ, Barker GJ, Duncan JS. In Vivo Short Echo Time 1H-Magnetic Resonance Spectroscopic Imaging (MRSI) of the Temporal Lobes *Neuroimage* 2001; 14:501-509.

87 Provencher S LCModel manual. Available at http://s-provencher.com/pages/lcmodel.shtml

88 Christiansen P, Toft P, Larsson DHB, Stubgaard M, Henriksen O. The concentration of N-acetyl aspartate, creatine + phosphocreatine, and choline in different parts of the brain in adulthood and senium. *Magn Reson Imag* 1993; 11:799-806

89 Srinivasan R, Vigneron D, Sailasuta N, Hurd R, Nelson S. A comparative study of myo-inositol quantification using LCmodel at 1.5T and 3.0T with 3 D 1H proton spectroscopic imaging of the human brain. *Magn Reson Imag* 2004; 22:523–528.

90 Thompson RB, Allen PS. Sources of variability in the response of coupled spins to the PRESS sequence and their potential impact on metabolite quantification. *Magn Reson Med.* 1999; 41:1162-1169.

91 Jiru F, Dezortova M, Burian M, Hajek M. The role of relaxation time corrections for the evaluation of long and short echo time 1H MR spektra of the hippocampus by NUMARIS and LCModel techniques. *MAGMA*. 2003 Nov;16(3):135-43.

92 Ethofer T, Mader I, Seeger U, Helms G, Erb M, Grodd W, Ludolph A, Klose U. Comparison of longitudinal metabolite relaxation times in different regions of the human brain at 1.5 and 3 Tesla. *Magn Reson Med*. 2003 Dec;50(6):1296-301.

93 Hornak JP, Szumowski J, Bryant RG. Magnetic field mapping. *Magn Reson Med* 1988; 6(2):158-63.

94 Alecci M, Collins CM, Smith MB, Jezzard P. Radio frequency magnetic field mapping of a 3 Tesla birdcage coil: experimental and theoretical dependence on sample properties. *Magn Reson Med* 2001; 46(2):379-85.

95 Thulborn KR, Boada FE, Shen GX, Christensen JD, Reese TG. Correction of B1 inhomogeneities using echo-planar imaging of water. *Magn Reson Med* 1998; 39(3):369-75.

96 Akoka S, Franconi F, Seguin F, Le Pape A. Radiofrequency map of an NMR coil by imaging. *Magn Reson Imaging* 1993; 11(3):437-41.

97 Stollberger R, Wach P. Imaging of the active B1 field in vivo. *Magn Reson Med* 1996; 35(2):246-51.

98 Klose U. Mapping of the radio frequency magnetic field with a MR snapshot FLASH technique. *Med Phys* 1992; 19(4):1099-1104.

99 Vaughan JT, Garwood M, Collins CM, Liu W, DelaBarre L, Adriany G, Andersen P, Merkle H, Goebel R, Smith MB, Ugurbil K. 7T vs. 4T: RF power, homogeneity, and signal-to-noise comparison in head images. *Magn Reson Med* 2001;46(1):24-30.

100 Oh CH, Hilal SK, Cho ZH, Mun IK. Radio frequency field intensity mapping using a composite spin-echo sequence. *Magn Reson Imaging* 1990; 8(1):21-5.

101 101 Ikonomidou VN, de Zwart JA, Duyn JH, van Gelderen P. B1 mapping based on signal modeling with magnetization prepared 3D EPI. *Proceeding of ISMRM*, 2005 (13), 899

102 Jiru F, Grodd W, Klose U. Correction for CSI excitation profile in inhomogeneous RF fields. No. 381, 22nd Ann Sci Meeting ESMRMB, Basle, Switzerland, Sept 15-18, 2005; *MAGMA* 18, Suppl.7, S224.

103 Seifert F, Wuebbeler G, Schubert F, Rinneberg H. Influence of dielectric resonance phenomena on calibration of NMR signals measured by high field MRS using local transmit/receive coils. *Proc. Intl. Soc. Mag. Reson. Med.* 2003; 11:2549.

104 Abduljalil AM, Aletras AH, Robitaille PM. 3D echo planar imaging: application to the human head. *Magn Reson Med* 1995; 34(2):144-8.

105 Jiru F, Skoch A, Klose U, Grodd W, Hajek M (2004) Spectroscopic imaging of Glutamine and Glutamate using LCModel and error images. In: Proceedings of the 21th Annual Science Meeting ESMRMB, *MAGMA* –Suppl, Copenhagen, Denmark

106 Young K, Khetselius D, Soher BJ, Maudsley AA Confidence images for MR spectroscopic imaging. *Magn Reson Med* 2000; 44:537–545.

107 Pouwels PJ, Brockmann K, Kruse B,Wilken B, Wick M, Hanefeld F, Frank J. Regional age dependence of human brain metabolites from infancy to adulthood as detected by quantitative localized proton MRS. Pediatr Res 1999; 46:474–485.

108 Hajek M, Adamovicova M, Herynek V, Skoch A, Jiru F, Krepelova A,Dezortova M. MR relaxometry and 1H MR spectroscopy for the determination of iron and metabolite concentrations in PKAN patients. *Eur Radiol* 2005; 15:1060–1068.

109 Hajek M, Komarek V, Dezortova M, Hlavnicka P, Smejkalova M, Faladova L, Hovorka J. Determination of epileptogenic focus using 1H MR spectroscopy. (Cz) *Ces Slov Neurol Neurochir* 1995; 3:103-107.
110 Cendes F, Caramanos Z, Andermann F, Dubeau F, Arnold DL. Proton magnetic resonance spectroscopic imaging and magnetic resonance imaging volumetry in the lateralization of temporal lobe epilepsy: a series of 100 patients. *Ann Neurol* 1997; 42:737-746.
111 Hajek M, Dezortova M, Komarek V. 1H MR spectroscopy in patients with mesial temporal epilepsy. *MAGMA* 1998; 7:95-114.
112 Hetherington HP, Pan JW, Spencer DD. 1H and 31P spectroscopy and bioenergetics in the lateralization of seizures in temporal lobe epilepsy. *J Magn Reson Imaging* 2000; 16:477-483.
113 Bernasconi A, Tasch E, Cendes F, Li LM, Arnold DL. Proton magnetic resonance spectroscopic imaging suggests progressive neuronal damage in human temporal lobe epilepsy. *Prog Brain Res* 2002; 135:297-304.
114 Hammen T, Stefan H, Eberhardt KE, W-Huk BH, Tomandl BF. Clinical applications of 1H-MR spectroscopy in the evaluation of epilepsies-what do pathological spectra stand for with regard to current results and what answers do they give to common clinical questions concerning the treatment of epilepsies? *Acta Neurol Scand* 2003; 108:223-238.
115 Garcia PA, Laxer KD, van der Grond J, Hugg JW, Matson GB, Weiner MW. Proton magnetic resonance spectroscopic imaging in patients with frontal lobe epilepsy. *Ann Neurol* 1995; 37:279-281.
116 Stanley JA, Cendes F, Dubeau F, Andermann F, Arnold DL. Proton magnetic resonance spectroscopic imaging in patients with extratemporal epilepsy. *Epilepsia* 1998; 39:267-273.
117 Lundbom N, Gaily E, Vuori K,et al. Proton spectroscopic imaging shows abnormalities in glial and neuronal cell pools in frontal lobe epilepsy. *Epilepsia* 2001; 42:1507-1514.